

RESEARCH AND ADVANCED DEVELOPMENT OF A 2 KW ARC-JET THRUSTOR

(NASA-CP-54035) RESEARCH AND ADVANCED
DEVELOPMENT OF A 2 KW ARC-JET THRUSTOR
(Plasmadyne Corp.) 131 p

N74-73650

00/99 Unclass
35252

O. J. McCaughey, W.A. Geideman, Jr., and K. Muller

prepared for

NATIONAL AERONAUTICS AND SPACE ADMINISTRATION

CONTRACT NAS 3-2521

FACILITY FORM 606	SECRET	
	(ACCESSION NUMBER)	(THRU)
	131	2
	(PAGES)	(CODE)
	CR54035	06
	(NASA CR OR TMX OR AD NUMBER)	(CATEGORY)

plasmadyne

A GIANNINI SCIENTIFIC COMPANY

REPRODUCED BY
NATIONAL TECHNICAL
INFORMATION SERVICE
U.S. DEPARTMENT OF COMMERCE
SPRINGFIELD, VA. 22161

CLASSIFICATION CHANGE

UNCLASSIFIED

TO -

By authority of

Changed by

E.O. 11652

Date 2-21-74

142

[REDACTED]

NASA CR-54035

GRC 1646

COPY NO. 35

SUMMARY REPORT

RESEARCH AND ADVANCED DEVELOPMENT
OF A 2 KW ARC-JET THRUSTOR

by

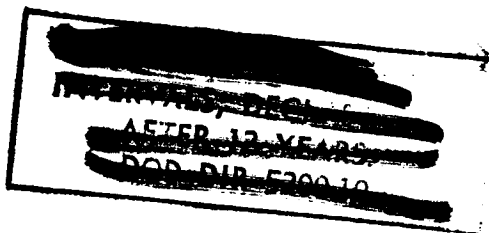
O. J. McCaughey, W. A. Geideman, Jr., and K. Muller

prepared for

NATIONAL AERONAUTICS AND SPACE ADMINISTRATION

CONTRACT NAS 3-2521

Technical Management
NASA Lewis Research Center
Cleveland, Ohio
Spacecraft Technology Division
Henry R. Hunczak and Harold Ferguson



PLASMADYNE CORPORATION

3839 South Main Street
Santa Ana, California

11

[REDACTED]

FOREWORD

This document is the Summary Report required under NASA Contract NAS 3-2521. It is the result of a six-month analytical and experimental program of applied research and advanced development of a 2 KW arc-jet thruster. The program was conducted by Plasmadyne Corporation for the NASA Lewis Research Center. The NASA Technical Monitors for the program were Messrs. Henry R. Hunczak and Harold Ferguson.

Mr. Owen J. McCaughey served as Program Manager at Plasmadyne, and as such was responsible for the overall performance of the program. Mr. William A. Geideman, Jr., served as Project Engineer during the latter phase of the program, and was responsible for direct supervision and coordination of the analytical and experimental efforts during that period. Mr. Kurt Muller served as Senior Research Engineer and was responsible for the areas of design analysis (aerodynamics, thermodynamics, and heat transfer), preliminary design of thrusters, and improvement of test instrumentation and experimental techniques. Others who contributed significantly to the program include Messrs. Morris Brillhart (Assistant Project Engineer for early phase), M. G. Mitcheltree (Test Engineer), Harold E. Wallace (Design Engineer), Erhard Gansel (Design Engineer), and Richard Rosic (Designer).

This Summary Report was prepared by Owen J. McCaughey, William A. Geideman, Jr., and Kurt Muller.

The experimental part of this program began in January 1963 and ended in July 1963.

ABSTRACT

17205

The research and advanced development of low power (1 - 2 KW) arc-jet thrusters for eventual attitude control and orbit correction applications continued at Plasmadyne Corporation during the first half of 1963 in a six-month program under the sponsorship of NASA (Contract NAS 3-2521). Prior to 1963 the work had been carried out at the 1 KW power level with only moderate success because of the very low flow rate and critically small dimensions. In the present program an increase to the 2 KW power level was specified in the hope that the higher flow rate, higher Reynolds number, and somewhat larger dimensions would permit development of a long life thruster.

The research and development phase of this six-month program consisted primarily of parametric investigations of arc region geometry and operation conditions, with supporting analytical and design work, in an attempt to determine the configuration with the best life and performance.

The present program was culminated in July 1963 with the successful completion of a 150 hour (6.3 day) continuous endurance test on a 2 KW D.C. arc-jet thruster using hydrogen as the propellant. Average performance during the 150 hour endurance test was:

Power input	=	2 KW
Hydrogen flow rate	=	3.2×10^{-5} lbs/sec.
Thrust	=	30.1 millipounds
Specific impulse	=	935 seconds
Propulsive efficiency	=	30.7%

This test, the first successful long duration endurance test on a low power arc-jet, was terminated voluntarily without failure. Results of this program indicate that the state-of-the-art has advanced to the point where low power arc-jet thrusters can be developed to produce good performance and long life in continuous operation. Recommendations are presented for making further improvements in the present design (used in 150 hour test) during future development work, based on concepts developed during this program.

Author

TABLE OF CONTENTS

	Page No.
1.0 INTRODUCTION AND SUMMARY	1
2.0 THRUSTOR DESIGNS	6
2.1 General Design Characteristics	6
2.1.1 Series 142-300 Thrustor (Arc Chamber-Throat Design)	6
2.1.2 Series 142-400 Thrustor (Cylindrical Constrictor Design)	10
2.1.3 Series 142-600 Thrustors (Cylindrical Constrictor Design - Advanced)	19
2.1.4 Summary of all Thrustor Designs	20
2.2 Internal Flow Passage Analysis	25
2.2.1 Series 142-400	25
2.2.2 Series 142-600	49
2.3 Anode Design and Heat Transfer in Anode	53
2.3.1 Series 142-400	53
2.3.2 Series 142-600	55
2.4 Optimum Nozzle Performance	55
2.4.1 Laminar Friction in a Nozzle	58
2.4.2 Effects of Non-Axial Flow	66
3.0 EXPERIMENTAL RESULTS	71
3.1 Systematic Variation of Throat Diameter	71
3.2 Systematic Variation of Anode-Cathode Axial Gap Spacing	75
3.3 New Area Ratio Nozzles	78
3.4 150-Hour Endurance Test	80
3.5 Tests of Series 142-300 Thrustor Design	97
3.6 Interpretation of Test Results	97

TABLE OF CONTENTS

	Page No.
4.0 TEST FACILITY AND INSTRUMENTATION	99
4.1 Thrust Balance	99
4.2 Mass Flow Measurement	101
4.2.1 Calibration Error Analysis	107
4.3 Summary of Test Instrumentation and Instrument Calibration	110
5.0 THRUSTOR ASSEMBLY, INSPECTION, TEST, AND DISASSEMBLY PROCEDURES	118
5.1 Thrustor Assembly and Inspection	118
5.2 Testing Procedure	122
5.3 Thrustor Disassembly and Re-inspection	122
6.0 CONCLUSIONS AND RECOMMENDATIONS	123
6.1 Conclusions	123
6.2 Recommendations	127
7.0 REFERENCES	128
APPENDIX A -- GAS CONSTANT OF INDUSTRIAL HYDROGEN	129

FIGURES

Figure No.		Page No.
2.1	2 KW Arc-Jet Thrustor Assembly Model 142-300	7
2.2	Schematic Illustration of the Two Principal Arc Configurations for DC Arc-Jets	9
2.3	Modification of Thrustor 142-300	11
2.4	2 KW Arc-Jet Thrustor Assembly, Model 142-400	13
2.5	Definition of Thrustor Geometry	16
2.6	2 KW Arc-Jet Thrustor Assembly, Model 142-600	21
2.7	Diagram of Cathode-Anode Geometry And Geometry of Cathode Gap Region	30
2.8	Diagram of Flow Area Variation in Constrictor Inlet	33
2.9	Flow Section in the Constrictor at Variable Cathode Gap Settings	39
2.10	Schematic of Flow Cross-Sectional Areas in Arc Region	40
2.11	Flow Through the Constrictor - Cold Flow Condition	43
2.12	Enthalpy-Entropy Diagram for Arc Heating Process	44
2.13	Plot of Flow Area, Velocity, Pressure, and Reynolds Number vs Axial Station - Hot Flow Conditions (Type 142-600)	45
2.14	Schematic Diagram of Propellant Flow System	46
2.15	Sketch of Propellant Flow Pattern in Vortex Chamber of Series 142-600 Thrustors	50
2.16	Sketch of Cathode Tip Configuration After Erosion	53
2.17	Original Anode Insert with Undercut, Series 142-400 Thrustor	54
2.18	Modified Anode Insert, Undercut Eliminated, Series 142-400 Thrustors	54
2.19	Second Modification of Anode Insert - Series 142-400	54
2.20	Calculated Nozzle Efficiency vs Area Ratio and Divergence Half-Angle (Simplified Analysis)	57
2.21	Description of Forces in a Divergent Nozzle	58
2.22	Description of Nozzle in the Cylindrical Coordinate System	60
2.23	Plot of Integral of Friction Function	65

FIGURES

Figure No.		Page No.
2.24	Description of Nozzle Coordinate System for the Axial Flow	66
2.25	Experimental Comparison Between a Short and a Long Nozzle With the Same Half Angle	69
3.1	Specific Impulse as a Function of Constrictor-Throat Diameter and Propellant Flow Rate -- Type 142-400 Thrustor	73
3.2	Efficiency as a Function of Constrictor Throat Diameter and Flow Rate -- Type 142-400 Thrustor	74
3.3	Efficiency vs Specific Impulse as a Function of Cathode-Anode Gap Setting for Constant Constrictor Diameter = 0.035 Inch -- Type 142-400 Thrustor	76
3.4	Efficiency as a Function of Axial Gap Setting at Various Levels of Specific Impulse for Constant Constrictor Diameter = 0.035 Inch -- Type 142-400 Thrustor	77
3.5	Experimental Comparison Between a Short and a Long Nozzle with the Same Half Angle	79
3.6	Photograph of Cathode After 25-Hour Endurance Test on Series 142-400 Thrustor	81
3.7	Photograph of Anode-Nozzle Insert from Exit End	82
3.8	Photograph of Anode-Nozzle Insert from Inlet End	83
3.9	Photograph of Series 142-600 Thrustor in Operation	85
3.10	Plot of Thrustor Inlet Pressure and Propellant Flow Rate vs Time -- 150-Hour Endurance Test	87
3.11	Plot of Thrust and Thrustor Surface Temperatures vs Time -- 150-Hour Endurance Test	88
3.12	Plot of Thrustor Efficiency and Specific Impulse vs Time -- 150-Hour Endurance Test	89
3.13	Plot of Thrustor Input Voltage and Current vs Time -- 150-Hour Endurance Test	90
3.14	Photograph of Cathode Mounted in Cathode Insulator After Disassembly of Series 142-600 Thrustor	92
3.15	Photograph of Cathode and Cathode Insulator After Disassembly of Series 142-600 Thrustor	93

FIGURES

Figure No.		Page No.
3.16	Photograph of Internal Parts of Series 142-600 Thrustor Assembled Without Molybdenum Outer Housing	94
3.17	Photograph of Nozzle Exit End of Anode-Nozzle Insert After Completion of 150-Hour Endurance Test	95
4.1	Schematic Diagram of Mechanical Force Amplification System for Thrust Measurement	100
4.2	Thrust Balance Calibration System	102
4.3	Photograph of Thrust Indicating and Recording Instrumentation	103
4.4	Typical Recording Trace and Read-out Data for Thrust Balance Calibration Using Remotely-Controlled Calibration System	104
4.5	Typical Thrust Calibration Curve	105
4.6	Schematic Diagram of Built-in Calibration System for Propellant Flowmeter	106
4.7	Calibration Curve for Orifice Flowmeter	108
4.8	Voltage Correction Curve for Esterline-Angus Voltmeter	112
4.9	Current Correction Curve for Esterline-Angus Ammeter	113
4.10	Schematic Diagram of 2 KW Arc-Jet Test Facility and Instrumentation Connections	115
4.11	View of Control Consoles	116
4.12	View of Vacuum Test Chambers	117
5.1	Assembler Inspecting Boron Nitride Rear Insulator for Dimensional Accuracy	119
5.2	Assembler Shown Using Precision Gauge to Set Cathode-Anode Gap Spacing	120
5.3	Assembler Shown Using High Voltage Hypot Instrument	121

TABLES

Table No.		Page No.
1	Definition of Symbols for Thrustor Geometry	16
2	Values of Geometric Parameters for Tests 1 - 10 to Determine Effects of Variation of Constrictor-Throat Diameter	17
3	Values of Geometric Parameters for Tests 11 - 21 to Determine Effects of Variation of Cathode-Anode Setting	18
4	Summary of Geometric Parameters of Thrustors Tested	23
5	Summary of all Thrustor Designs Tested	27
6	Tabulation of Minimum Flow Sections	32
7	Flow Areas in the Anode	38
8	Calculated Values of Minimum Area to Throat Area Ratio	40
9	Friction Losses in the Propellant Passages	48
10	Flow Passage Geometry and Flow Velocities in Series 142-600 Thrustors	51
11	Optimum Nozzle Area Ratio as a Function of Divergence Half Angle	68
12	Summary of Experimental Tests on 2 KW Thrustor	72
13	Description of Instrumentation - 2 KW Arc-Jet Engine Program	111
14	Description of Test Facility - 2 KW Arc-Jet Engine Program	114

1.0 INTRODUCTION AND SUMMARY

A NASA-sponsored program for research and development of low power (1-2 KW) arc-jet engines has been in progress at Plasmadyne Corporation since September 1960. This program was initiated by the NASA Marshall Space Flight Center in 1960, under contract NAS 5-651, and the first phase of the program was under the sponsorship and direction of that Center.

The work statement for the first phase required, in part, that Plasmadyne conduct applied research and development on thrusters and other components necessary to demonstrate the operation of an arc-jet engine suitable for attitude control applications on space satellites. The engine was to be designed so that with minimum redesign it could be incorporated into attitude control systems for satellites of the type to be launched by Centaur and Saturn vehicles. Later, the Phase I program (1960-61) was modified extensively, with the final version requiring the design, development, flight qualification, and delivery of a number of complete flight test engines for the SERT program, together with ground support equipment and mock-up hardware.

Most of the Phase II program (1961-62), a continuation of the NAS 5-651 contract, was carried out under the sponsorship and direction of the NASA Lewis Research Center. This phase also underwent several modifications during the twelve-month period. It was divided into three somewhat separate and parallel efforts, as follows:

- 1) A thruster research and development effort, with heavy emphasis placed on the applied research and development necessary to achieve a steady-state thruster capable of long life with high reliability.
- 2) A systems engineering and engine flight test effort, initially as a part of the SERT flight test program, later modified to encompass only a comprehensive engine ground test program in a simulated space environment.
- 3) An electromechanical controls and dynamic measurements effort, intended to provide all of the control elements and sub-systems required to assemble a laboratory model of a complete single axis arc-jet attitude control system, and to provide special test equipment to measure the dynamic performance of such a system.

In November 1961, a study contract, NAS 8-2544, was awarded to Plasmadyne by Marshall Space Flight Center to parallel the Phase II effort. The objective of that program, most of which was monitored by the Lewis Research Center, was to investigate analytically the potential applications of low power arc-jets and to make a preliminary design study of an arc-jet attitude control and station-keeping system for a 550 lb.

~~CONFIDENTIAL~~

synchronous communication satellite.

The results of these past programs have been presented in previous Plasmadyne reports (see References).

For the 1963 period, the scope of the NASA sponsored program at Plasmadyne for research and development of low power arc-jets was modified again to one in which the sole objective was to investigate continuous running thrusters at the 2 KW power level. A six-month contract, NAS 3-2521, was awarded to Plasmadyne for this purpose, under the direction of the Lewis Research Center. The results of the program are presented in this Summary Report. The goal of the present program was to develop a thruster capable of operating continuously for at least 250 hours at 2 KW, 1000 seconds specific impulse, and 20 millipounds of thrust. The change from the 1 KW to the 2 KW power level was made primarily to allow the thruster dimensions and operating Reynolds number to be increased in the hope that a long-life configuration could be found in the low power size. Concentration only on obtaining long life in a continuous running thruster was specified by the NASA Technical Monitors in the belief that it was mandatory to demonstrate the feasibility of obtaining useful lifetimes in low power arc-jets before continuing the development of either pulsed thrusters or continuous running thrusters for attitude control, station-keeping, or primary propulsion applications. It was stated that consideration would be given to the development of pulsed arc-jet thrusters and complete arc-jet attitude control and station-keeping systems when and if long life capability was demonstrated.

The scope of work under this program was specified in considerable detail by the NASA Technical Monitors, both prior to and during the program. It was intended to be primarily a parametric experimental investigation of the effects of geometry and operating point variation on the performance and life of one type of thruster design -- the conventional constricted arc design -- which had been investigated at the 1 KW power level in the previous programs. Analytical work was to be done as required in support of the experimental program.

The primary objective program -- the development and demonstration of reasonably long life capability in a low power arc-jet -- was reached in July 1963 when a 2 KW thruster developed under this contract successfully completed a 150 hour continuous endurance test at Plasmadyne. The test was voluntarily terminated without failure at the 150 hour point because of a lack of funds to continue the experimental effort under the contract. Post-test examination of the thruster indicated that the endurance test could probably have been continued for a substantially longer period of time without failure.

The average thrust produced by this thruster during the entire 150 hour test was 30.1 millipounds at a specific impulse level of 935 seconds and an overall propulsive efficiency of 30.7 percent. Performance remained nearly constant (within about 2.5 percent) throughout the endurance test.

The endurance test had been scheduled to be run at a specific impulse level of 1000 seconds, but an uncooled thrust balance was used for the test and a post-test hot calibration of the balance indicated that the test had been run at an average level of 935 seconds. However, propulsive efficiency during the endurance test was 40 percent higher than the minimum specified by the work statement.

A duplicate thruster was operated successfully for short periods at specific impulse levels up to 1275 seconds and at power levels from 1.5 to 3.5 KW.

In several preliminary design and mission studies carried out by Plasmadyne on the low power arc-jet engines it has been found that these engines are compatible with solar panel-battery power supplies and have many advantages over competitive engines for long duration attitude control and orbit correction applications on space vehicles such as communication satellites, geophysical satellites, and manned orbiting space stations (e.g., MOSS).

Potential advantages include:

1. Power can be supplied by state-of-the-art solar panels and/or batteries.
2. Both pulse-mode and steady-state operation of low power arc-jets have been successfully demonstrated.
3. Specific thrust levels (lbs/KW) are high enough to produce useful torques (in attitude control) and useful accelerations (in station-keeping and primary propulsion).
4. Specific impulse levels of arc-jets are sufficiently high, and overall system weights (including propellant storage, power supply and power conditioning sub-systems) are sufficiently low to make the arc-jet (or combination arc-jet and resisto-jet) attitude control and station-keeping system very competitive in several applications.
5. Low power arc-jet thrusters operate at a single moderate voltage level, about 100 volts, and do not require complex power conditioning equipment.
6. Electrothermal thruster systems can automatically operate as cold hydrogen thrusters (at $I_{sp} \sim 250$ seconds) in the event of interruption or failure of the main power supply or power conditioning equipment.
7. The feasibility of hydrogen propellant storage system has been indicated in design studies.

~~CONFIDENTIAL~~

The thrusters developed under this program have been designed primarily for continuous operation and, as such, would not be very suitable for the short-pulse operation required in many control applications, even though an earlier 1 KW model was tested with some success in the short-pulse mode of operation (~200 millisecond pulses). If actual control applications are contemplated, a true pulse-mode arc-jet will have to be designed and tested specifically for that purpose.

It was found in the present program that several areas of the thruster were more critical than previously realized, and needed greater analytical and design attention than they had received in the past. These areas included the propellant injector-vortex chamber configuration, the nozzle divergence angle, and the heat transfer in the anode-nozzle- both internally by conduction and externally by radiation and contact conduction. The final design benefited from work on all of these areas.

It has also been found that thruster efficiency level can have a rather direct bearing on the life problem in low power arc-jet development. Low power thrusters suffer primarily from the fact that propellant flow rates are very low and internal dimensions (including the constrictor-throat) are correspondingly small and critical. For a specified input power level and specific impulse level (e.g., 2 KW and 1000 seconds), however, both propellant flow rate and flow passage areas can be shown to be directly proportional to efficiency. Since even small increases in flow rate and passage area can be significant in increasing the life capability of low power thrusters, it would appear well worthwhile to attempt to increase the efficiency of such engines above the present 30-33% level from the standpoint of life alone, not to mention the benefits that would accrue from the increase in performance.

It is concluded that the state-of-the-art of low power (1 - 2 KW) arc-jet thrusters has been advanced substantially during the course of the six-month program reported herein. In particular, a much better understanding of how to design successful long life thrusters has been achieved. During this program the first endurance test of significant duration (150 hours) on a low power arc-jet was successfully completed, with reasonably good performance, and the way has been pointed for further increases in life and performance capability.

The capability of demonstrating continuous endurance runs of the order of 500 to 1000 hours (or more) on low power thrusters is now definitely possible within the near future if some further development effort along the present lines is carried out. In addition, it appears quite feasible to increase both specific impulse and efficiency somewhat above the present levels by simply making further refinements in the present design, including the use of established regenerative cooling techniques. If these levels of life

~~CONFIDENTIAL~~

and performance could be demonstrated, it is felt that low power arc-jets could advance into the category of practical engines for near-future space vehicles with solar-cell power supplies.

2.0 THRUSTOR DESIGNS

2.1 General Design Characteristics

The purpose of the program described in this report was to conduct research and advanced development work on continuous-running radiation-cooled arc-jet thrusters at the 2 KW power level in an attempt to achieve long life capability coupled with good performance at that power level. During the course of this program three somewhat different thruster design concepts were investigated. The first design concept was a scaled-down version of a configuration which had earlier proved to be successful at higher power levels; the second was basically identical to the configuration which had been used in a previous 1 KW arc-jet program; and the third and final concept represented an advanced version of the second configuration, incorporating several major modifications and improvements which resulted from the research and development effort.

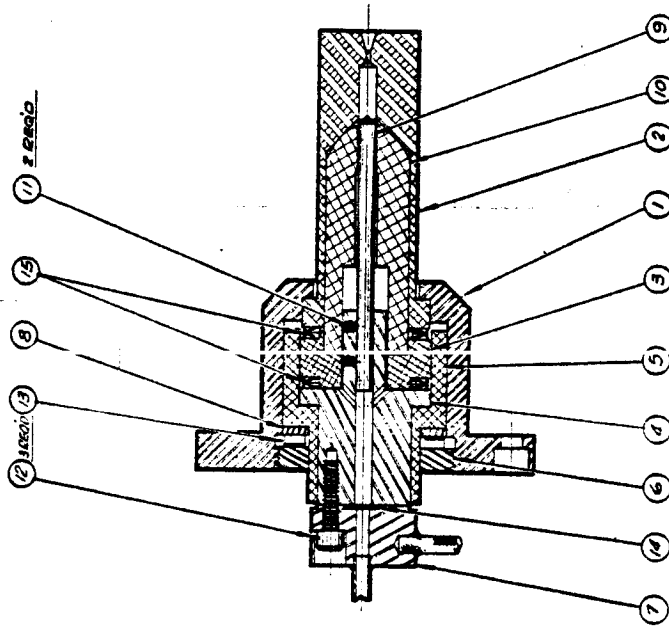
The three different configurations were assigned to the following Plasmadyne designations:

1. Series 142-300 (Arc chamber - throat design)
2. Series 142-400 (Cylindrical constrictor design)
3. Series 142-600 (Cylindrical constrictor design - advanced)

The design characteristics of each series are described in some detail in the following sub-sections.

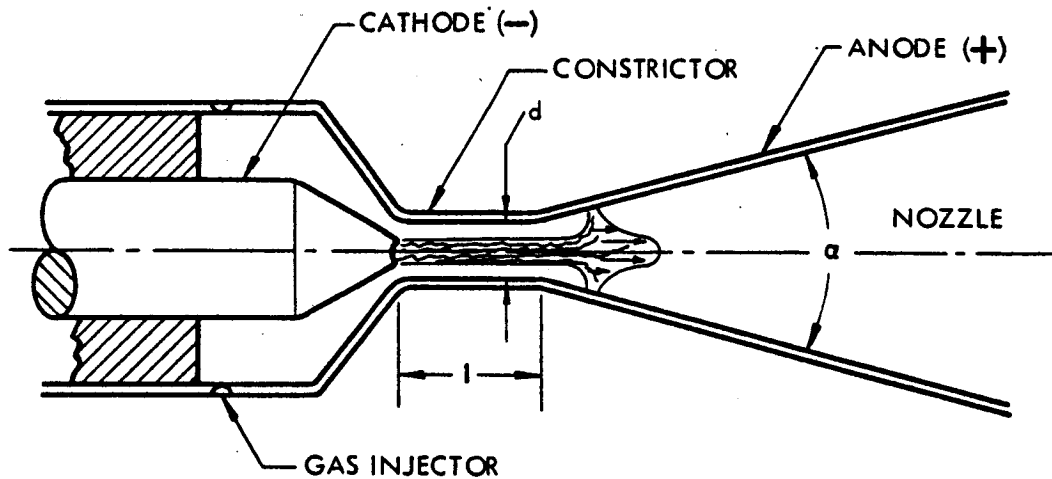
2.1.1 Series 142-300 Thrusters (Arc Chamber - Throat Design)

This design approach was selected in an attempt to scale down to the 2 KW size a configuration which had proved to be very successful at Plasmadyne for higher power levels and moderate specific impulse levels (~ 1000 seconds). The basic design is shown in Figure 2.1. In this design concept a constriction, or throat, is employed at the downstream end of a subsonic arc chamber to form the inlet to the divergent nozzle. The entire arc column is normally confined within the subsonic arc chamber upstream of the throat, rather than extending into the supersonic flow region in the divergent nozzle. Under certain conditions in this design the anode attachment region of the arc may oscillate at high frequency back and forth along the walls of the arc chamber, tending to minimize local overheating and erosion of the anode. Almost all of the propellant heating occurs in the subsonic region upstream of the throat, rather than part of it in the divergent nozzle as in other designs. The result is a tendency toward more uniform distributions of energy flux and gas velocity in the jet at the nozzle exit, and in some cases higher propulsive efficiencies at moderate specific impulse levels. The concept is shown schematically in Figure 2.2 (b).

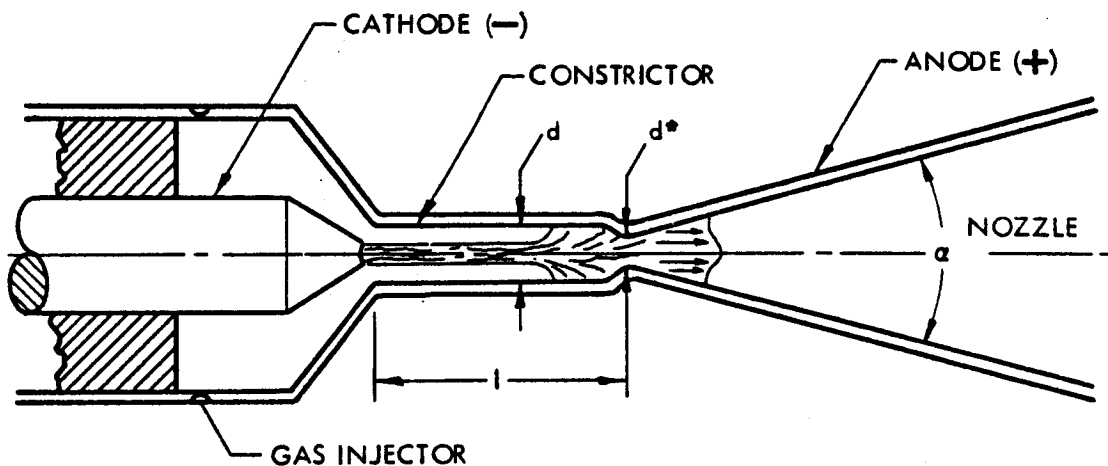


QUANTITY	PART NUMBER	ITEM	DESCRIPTION	MATERIAL
2	HS 4-15	15	K SEAL	INCONEL X
1	HS 174-4	14	K SEAL	INCONEL X
1	AS 15728	13	WAVE WASHER ASSO. SPRING CORP.	INCONEL X
3	MS 35457-7	12	SOC. HD. CAR SCREW	STEEL
2		11	7/6-32 NC X 3/8 LG SET SCREW	STEEL
1	142-320	10	7/1-64 NC X 5/32 LG FORWARD INSULATOR	
1	142-319	9	CATHODE	
1	142-318	8	BEARING RING	
1	142-317	7	CAP ASSEMBLY	
1	142-316	6	RETAINER	
1	142-315	5	INSULATOR, OUTER	
1	142-314	4	CATHODE HOLDER	
1	142-313	3	SEAL SPACER, INSULATOR	
1	142-312	2	ANODE BODY	
1	142-311	1	THRUSTOR HOUSING	

Figure 2.1. 2 KW Arc-Jet Thrustor Assembly, Model 142-300



(a) Constricted Arc Design - Arc attaches to anode downstream of throat in divergent section of nozzle.



(b) Subsonic Arc Chamber Design - Arc attaches to anode upstream of throat in subsonic section of nozzle.

Figure 2.2 Schematic Illustration of the Two Principal Arc Configurations for DC Arc-Jets

The basic geometric parameters of the thruster design shown on Drawing 142-300 (Figure 2.1) are as follows:

Arc chamber length-diameter ratio	$\frac{L_{a. c.}}{D_{a. c.}}$	=	5.54
Throat length-diameter ratio	$\frac{L_{th}}{D_{th}}$	=	1.0
Nozzle area ratio	$\frac{A_e}{A_{th}}$	=	11
Throat diameter	D_{th}	=	0.043"
Cathode tip half angle	γ_o	=	45°
Nozzle divergence half angle	θ	=	15°
Total weight of the thruster	G	=	1.0 lb.

The propellant was guided along the cathode, first axially, then through a spiral, creating a swirl in the arc chamber to stabilize the arc. The cathode and anode material was 2% thoriated tungsten, and the cathode insulator was of boron nitride.

Thruster 142-300 was modified in two steps. Firstly, an interchangeable anode insert, containing the arc chamber, throat and nozzle, was devised to make geometric changes more practical. Secondly, in order to reduce the high radiation losses limited regenerative cooling was provided by channeling the propellant along the high temperature section of the housing and anode before injection into the arc chamber (see Figure 2.3).

Experimental testing of the 142-300 series of thruster was very limited, by direction of the NASA Technical Monitors, and results were interesting but inconclusive.

2.1.2 Series 142-400 Thrusters (Cylindrical Constructor Design)

This second design approach was selected simply as a continuation of the configuration which had been investigated rather extensively at the 1 KW power level during the final phase of the preceding program, Contract NAS 5-651 (see Summary Report, Reference 2). Only a very modest degree of success had been achieved at the 1 KW power level after a substantial amount of effort, probably because of the very low flow rates, very small constrictor sizes, and very low Reynolds numbers associated

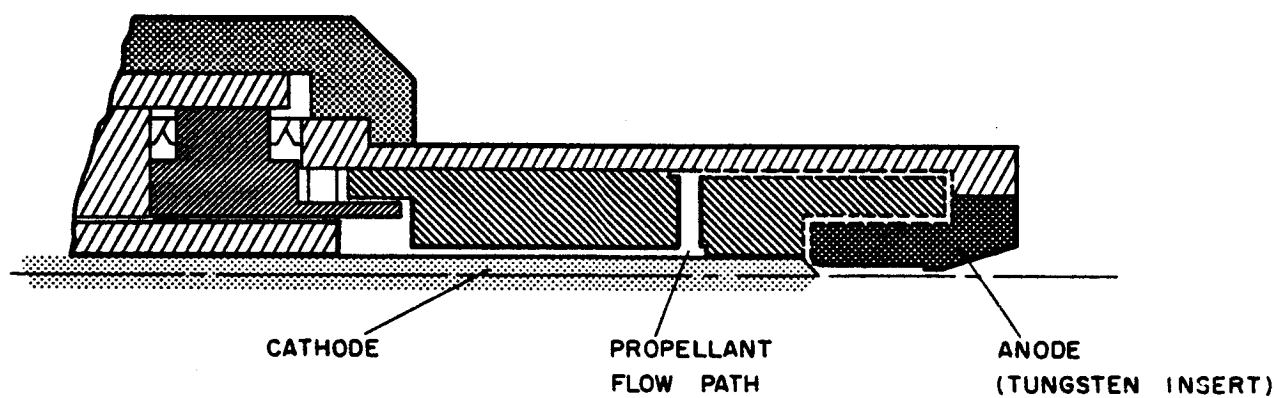


Figure 2.3 Modification of Thrustor 142-300

with that power level. It was finally decided that the research and development effort could be carried out more productively at the 2 KW level, since the mass flow rates would be a little more than twice those at the 1 KW level (because of higher efficiency) and it could be expected that the very difficult problems of low power arc-jets might be solved somewhat more easily at the 2 KW level.

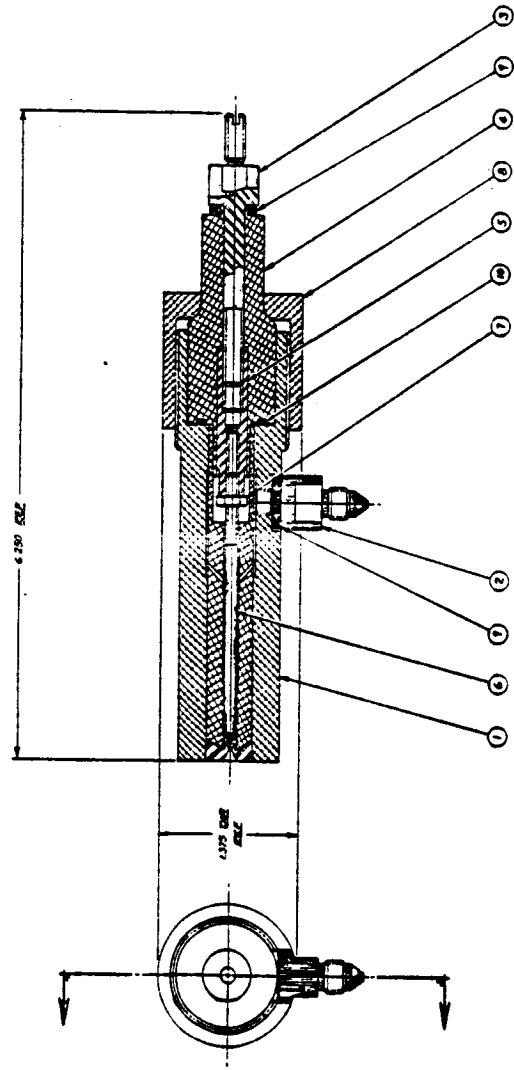
The basic thruster design is shown in Figure 2.4. In this design concept a short straight cylindrical arc constrictor section is employed for the purpose of stretching the arc column completely through the constrictor and out into the divergent section of the nozzle where a diffuse anode attachment region can occur, as shown schematically in Figure 2.2 (a), page 9.

This thruster was designed primarily for research and development work on the electrodes, arc configuration, and nozzle. It was made somewhat longer than is probably necessary in order to minimize the gas seal problems at the "cold" end of the radiation-cooled housing, and it was designed with an interchangeable anode insert to permit easy modification of electrode and nozzle geometry. The thoriated tungsten anode insert is held in position in the molybdenum body by the wedge action of a three degree taper. The three degree taper was found experimentally to produce a very firm and gas-tight connection between the tungsten anode and the molybdenum thruster housing.

The cathode was also made of thoriated tungsten, and was inserted into the boron nitride cathode insulator which was pressed into the precision bore of the housing. The gap between the anode and the cathode could be adjusted for each assembly and then locked in position by means of a lock nut.

Special attention was given to thruster leakage problems since cold leak checks do not necessarily guarantee gas tightness during hot operation because of differential expansion and thermal distortion of the components. In order to check hot thruster leakage a dummy anode insert was made without any nozzle opening, and hot leak checks were performed by pressing the dummy anode insert into the housing, pressurizing the thruster with a propellant supply, and heating the thruster to approximately operating temperature with a torch. The total leakage from the thruster was found to be consistently negligible, thus demonstrating the overall suitability of the design from the propellant leakage standpoint.

Referring to Figure 2.4, the propellant enters the thruster through the side port and is guided by four holes from the outer ring chamber to the center hole in the cathode insulator. From there it flows axially through the annular passage formed by the cathode and the cathode insulator, and then through threaded spiral



QUANTITY	PART NUMBER	ITEM	DESCRIPTION	MATERIAL
1	142 - 517	10	METALLIC "O" RING	321 SS
2	142 - 518	9	HASKEL ENG. K SEAL	INCONEL X
1	142 - 508	8	HASKEL ENG. RETAINING CAP	MOLY
1	142 - 507	7	CATHODE LOCK NUT	MOLY
1	142 - 506	6	CATHODE	2% THORIATED TUNGSTEN
1	142 - 505	5	CATHODE HOLDER	MOLY
1	142 - 504	4	REAR INSULATOR	BORON NITRIDE
1	142 - 503	3	CATHODE CONNECTOR	MOLY
1	142 - 502	2	GAS CONNECTOR	MOLY
1	142 - 500	1	THRUSTOR HOUSING ASSEMBLY	MOLY

Figure 2.4. 2 KW Arc-Jet Thrustor Assembly, Model 142-400

passages into the chamber between the cathode and the anode. The threaded passages were employed to generate a vortex flow for arc stabilization in the constrictor.

By direction of the NASA Technical Monitors, most of the experimental work done under the program reported here was conducted on the series 142-400 thruster design, and, in particular, was devoted to making comprehensive parametric investigations of geometric and operating variables for the basic 142-400 thruster design and its various modifications.

In the first series of tests, Tests 1 - 10, the constrictor - throat diameter was varied in 0.005 inch increments from 0.015 inch to 0.035 inch while the following parameters were held constant:

Ratio of smallest flow area ¹⁾ to throat area	-	A_{\min}/A_{th}
Cathode tip half angle	-	γ_0
Anode inlet half angle	-	α
Cathode tip radius	-	r

Because of the method used in manufacturing the anodes, the ratio L_{th}/D_{th} and the nozzle exit area both varied with throat diameter, but not greatly. The geometric parameters are defined in Table 1 and shown in Figure 2.5

With the geometric parameters listed above held constant, the following parameters varied automatically with variation in throat diameter:

Nozzle area ratio	-	A_e/A_{th}
Throat (constrictor) length	-	L_{th}
Gap between cathode and anode	-	s
Smallest flow section	-	A_{\min}

All values are summarized in Table 2

A second series of tests, Tests 11-21, was conducted with a thruster having a constant constrictor-throat diameter, but a variable gap. The constants and the variables are shown in Table 3

1) For definition of the smallest flow area see paragraph 2.2.1.1, page .

TABLE 1
Definition of Symbols for Thrustor Geometry
(Series 142-400 and 142-600 Thrustors)

D_{th}	=	Constrictor-throat Diameter (in)
L_{th}	=	Constrictor-throat Length (in)
s	=	Cathode-Anode Gap Setting (in)
A_{min}	=	Smallest Cross Section (sq. in)
A_{th}	=	Throat Cross Section (sq. in)
A_e	=	Exit Area of the Nozzle (sq. in)
α	=	Anode inlet half angle (deg)
γ_o	=	Cathode Tip Half Angle (deg)
θ	=	Nozzle Divergence Half Angle (deg.)
L_{th}/D_{th}	=	Constrictor Length - Diameter Ratio
A_e/A_{th}	=	Nozzle Area Ratio
P	=	Performance Test
E	=	Endurance Test

} Type of Test Performed

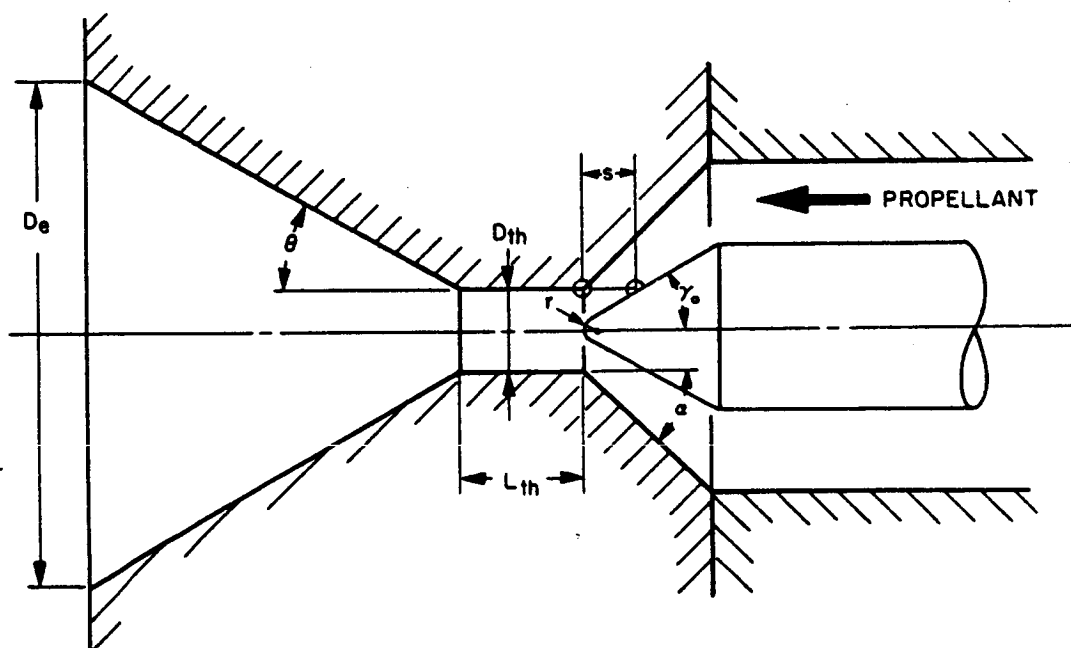


Figure 2.5 Definition of Thrustor Geometry

TABLE 2
Values of Geometric Parameters for Tests 1 - 10
to Determine Effects of Variation of Constrictor-Throat Diameter

Minimum Area to Throat Area Ratio	A_{min}/A_{th}	=	0.666					
Cathode Tip Half Angle	γ_o	=	30°					
Anode Inlet Half Angle	α	=	45°	Constant				
Nozzle Exit Half Angle	θ	=	30°					
Cathode Tip Radius	r	=	0.004"					
Cathode Gap Settings (inches)								
D_{th} (in)	L_{th}/D_{th}	D_e (in)	A_e/A_{th}	Test Number				
				1, 3 0.006	2, 10 0.008	4, 7 0.010	5, 8 0.012	6, 9 0.014
0.015	1.540	0.135	81	XX ²⁾				
0.020	1.625	0.132	43.6		XX			
0.025	1.748	0.127	25.8			XX		
0.030	1.770	0.124	17.1				XX	
0.035	1.737	0.123	12.4					XX

In most cases more than one test was run on a given configuration, either to check on repeatability of performance data obtained, or to make a short endurance test on the configuration.

In the early versions of the 142-400 thruster design some inconsistencies appeared in the measured values of the pressure p_2 downstream of the flowmeter orifice for supposedly identical thrusters operating under identical conditions. Since p_2 was used as a measure of the vortex chamber pressure -- the design was such that it was almost impossible to connect a pressure tap directly into the vortex chamber itself -- this lack of repeatability was relatively serious from the data correlation standpoint. The discrepancies were found to be caused by excessive velocities in the internal cooling passages of the thruster when large throat diameters were tested, together with excessive variations in the cross-sectional areas of the cooling flow passages from one thruster to another. The threaded passage near the cathode tip, as shown on Drawing 142-400, consisted of a two-start multiple thread with rectangular cross section. The total cross-sectional area of the flow passages was 1.5 times the area of the throat when the 0.035" diameter throat was used. The tolerance of the thread, as originally specified on the shop drawing, allowed a variation in cross section of as much as 20%. The small flow passage caused a large gas velocity and, since the pressure drop for

2) Double X means repetition of test

TABLE 3

Values of Geometric Parameters for Tests 11-21
to Determine Effects of Variation of Cathode-Anode Gap Setting
(a)

Throat Diameter	D_{th}	=	0.035"	Constant	
Nozzle Exit Diameter	D_e	=	0.123"		
Nozzle Area Ratio	A_e/A_{th}	=	12.4		
Constrictor-Throat L/D Ratio	L_{th}/D_{th}	=	1.737		
Anode Half Angle	α	=	45°		
Nozzle Divergence Half Angle	θ	=	30°		
Cathode Tip Half Angle	γ_o	=	30°		
Cathode Tip Radius	r	=	0.004"		
Test Number	12, 13	14	11, 15, 19, 20	16, 17	18
Gap Setting s(in)	0.014	0.020	0.026	0.032	0.038
Ratio A_{min}/A_{th}	0.666	0.863	1.000	1.100	1.205

(b)

Constrictor-throat L/D Ratio	L_{th}/D_{th}	=	1.500	Constant
Throat Diameter	D_{th}	=	0.035"	
Nozzle Exit Diameter	D_e	=	0.119	
Ratio	A_e/A_{th}	=	11.5	
Anode Inlet Half Angle	α	=	45°	
Nozzle Exit Half Angle	θ	=	30°	
Cathode Tip Half Angle	γ_o	=	30°	
Cathode Tip Radius	r	=	0.004"	

Test Number	21
Gap Setting s	0.026"
Ratio A_{min}/A_{th}	1.000

pipe flow is proportional to the square of the velocity, the pressure P_2 consequently varied over a large range. A brief study indicated that a high gas velocity in the passage was not necessary for effective cathode cooling.

The situation was corrected by a combination of changes in thruster cooling passage design and changes in procedure for machining, inspecting, and assembling the thrusters. In a first modification of the original 142-400 design, the cross-section of the flow passage was increased. Because of machining tool limitations it was not practical to cut a wider or deeper internal thread into the boron nitride. The problem was solved temporarily by adding two new passages on the outside of the cathode insulator which intersected with the inner channels near the cathode tip. This thruster with a double coaxial gas passage was tested in Test No. 23, and a smaller pressure drop through the gas passages was measured. However, the flow division between the two sets of coaxial gas flow passages was indeterminate, and it was decided to discontinue the design.

A different approach was taken by cutting the grooves into the cathode itself in order to enlarge the flow area and to maintain close tolerances. A number of threaded cathodes were fabricated, but were not tested because the new and superior series 142-600 design (described below) was built and tested before the threaded cathodes became available.

In a second modification of the original 142-400 configuration the upstream face of the anode-nozzle insert was changed in order to provide better vortex flow through the constrictor and to increase the radial heat flux from the throat region for better anode cooling and less erosion. This was accomplished by eliminating the undercut in the upstream face of the insert so that it would be flat, and by rounding the entrance to the constrictor inlet region for better flow conditions. At the same time the cathode insulator was redesigned to mate with the new flat upstream face of the anode-nozzle insert. This design was tested in Tests No. 25 and 26.

2.1.3 Series 142-600 Thrusters (Cylindrical Constrictor Design-Advanced)

The series 142-600 thruster design was derived from the series 142-400 design described above after four months of testing and analysis. It employed the same basic design concepts and arc region geometry as the 142-400 design -- that is, the straight cylindrical arc constrictor arrangement. However, it differed substantially from the previous design in other features, notably in the propellant injector design, the anode and cathode cooling arrangement, and the supersonic nozzle configuration. Features of the 142-300 design were not used because of its brief and inconclusive test program.

A cross-sectional drawing of this configuration is shown in Figure 2.6. The anode-nozzle insert, the cathode tip region, the cathode insulator, and the propellant injector-vortex chamber area had to be completely redesigned from the 142-400 configuration, but the thruster housing and several other parts of the original design were still useable.

The incoming propellant is ducted through the single-start trapezoidal thread on the outside of the cathode insulator toward the outer annular chamber, called receiver. From the receiver, six injector holes inject the gas tangentially into the inner annular chamber, called the vortex chamber. Some axial velocity was imparted by inclining the injector holes. Flow into the cathode tip region was improved by grinding a larger radius on the cathode at the intersection of the cylindrical shaft and the conical tip. This also tended to prevent arcing from the cathode except at the tip.

The propellant flows from the vortex chamber through a coaxial conical passage into the rounded inlet of the constrictor-throat. The coaxial conical passage is formed by the space between the conical tip of the cathode (30° half-angle) and the conical inlet to the constrictor (also 30° half-angle).

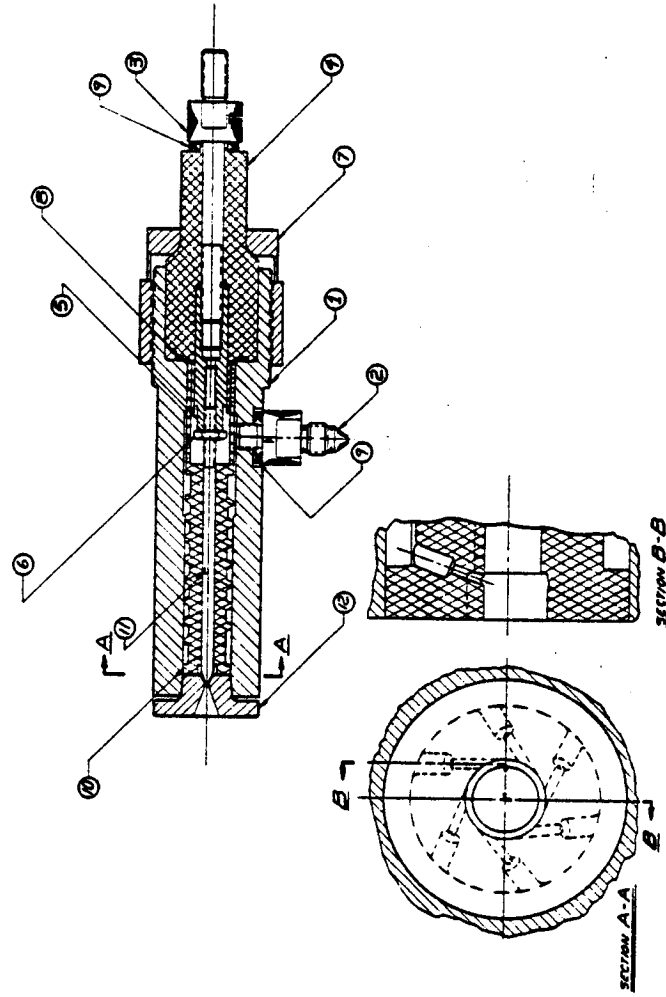
The anode is held in place in the thruster housing by a press fit allowing the possibility of interchanging nozzles. The new insert was designed specifically to increase the radial heat flux in order to more effectively cool the throat region. The large disk on the end of the insert performed the function of a radiator. It was found that a disk of the same diameter as the thruster housing was sufficient to adequately cool the anode. This design was applied in Tests No. 29 and 30.

Prior to the Test No. 29, a similar design was tested in Test No. 28 with four injector holes, but the anode was not equipped with a radiation disk. It was learned from Test No. 28, that a strong swirl improved the arc stabilization as indicated by a very stable and uniform plume. The design used in Tests No. 29 and 30 was arrived at by a refinement of the injection system (6 injector holes) which increased the intensity and uniformity of the vortex, and by adding the radiation disk which lowered the temperature in the hot spot regions.

The series 142-600 thrusters could only be tested to a limited extent before the program ended, but these few tests, including the 150 hour endurance test, were highly successful.

2.1.4 Summary of all Thruster Designs

In Table 4 the geometric parameters of all 2 KW arc-jet engines tested are



1	142 - 603	12	ANODE INSERT	TUNGSTEN
1	142 - 602	11	CATHODE INSULATOR	TUNGSTEN
1	142 - 601	10	K SEAL	BORON NITRIDE
2	142 - 518	9	HASKEL ENG.	INCONEL X
1	142 - 517	8	"O" RING, METALLIC	
1	142 - 508	7	HASKEL ENG.	CRES
1	142 - 507	6	RETAINING CAP	MOLY
1	142 - 505	5	CATHODE LOCK NUT	MOLY
1	142 - 504	4	CATHODE HOLDER	MOLY
1	142 - 503	3	REAR INSULATOR	BORON NITRIDE
1	142 - 502	2	CATHODE CONNECTOR	MOLY
1	142 - 501	1	GAS CONNECTOR	MOLY
1			THRUSTOR HOUSING	MOLY

Figure 2.6. 2 KW Arc-Jet Thrustor Assembly, Model 142-600

SUMMARY OF GEOMETRIC PARAMETERS OF THRUSTORS TESTED

Test Number	D_{th}	δ	L_{th}/D_{th}	ϕ	A_{mlr}/A_{th}	A_e/A_{th}	Anode Drawing Number	Dash Number	Type of Test	Group	Date		
1	0.015	0.006	1.540	30	45	30	0.666	81	142-521	1	P	142-400	3-18-63
2	0.020	0.008	1.625	30	45	30	0.666	43.6	142-521	2	P	142-400	3-19-63
3	0.015	0.006	1.540	30	45	30	0.666	81	142-521	1	P	142-400	3-20-63
4	0.025	0.010	1.748	30	45	30	0.666	25.8	142-521	3	P	142-400	3-21-63
5	0.030	0.012	1.770	30	45	30	0.666	17.1	142-521	4	P	142-400	3-22-63
6	0.035	0.014	1.737	30	45	30	0.666	12.4	142-521	5	P	142-400	3-25-63
7	0.025	0.010	1.748	30	45	30	0.666	25.8	142-521	3	P	142-400	3-27-63
8	0.030	0.012	1.770	30	45	30	0.666	17.1	142-521	4	P	142-400	4-1-63
9	0.035	0.014	1.737	30	45	30	0.666	12.4	142-521	5	P	142-400	4-1-63
10	0.020	0.008	1.625	30	45	30	0.666	43.6	142-521	2	P	142-400	4-3-63
11	0.035	0.026	1.737	30	45	30	1.000	12.4	142-521	5	P	142-400	4-5-63
12	0.035	0.014	1.737	30	45	30	0.666	12.4	142-521	5	P	142-400	4-19-63
13	0.035	0.014	1.737	30	45	30	0.666	12.4	142-521	5	P	142-400	5-2-63
14	0.035	0.020	1.737	30	45	30	0.863	12.4	142-521	5	P	142-400	5-8-63
15	0.035	0.026	1.737	30	45	30	1.000	12.4	142-521	5	P	142-400	5-9-63
16	0.035	0.032	1.737	30	45	30	1.100	12.4	142-521	5	P	142-400	5-9-63
17	0.035	0.032	1.737	30	45	30	1.100	12.4	142-521	5	P	142-400	5-13-63
18	0.035	0.036	1.737	30	45	30	1.205	12.4	142-521	5	P	142-400	5-14-63
19	0.035	0.026	1.737	30	45	30	1.000	12.4	142-521	5	E	142-400	5-15-63
20	0.035	0.026	1.737	30	45	30	1.000	12.4	142-521	5	E	142-400	5-17-63
21	0.035	0.026	1.500	30	45	30	1.000	11.7	142-519	5	E	142-400	5-22-63
22	0.035	0.026	1.737	30	45	30	1.000	12.4	142-521	5	E	142-400	5-27-63
23	0.035	0.026	1.737	30	45	30	1.000	12.4	142-521	5	E	142-400	5-29-63
24	0.035	0.020	1.757	30	45	20	0.863	50	142-520	--	E	142-400	6-6-63
25	0.035	0.014	1.737	30	45	30	0.666	12.4	142-521	5	P	142-400	6-11-63
26	0.035	0.014	1.737	30	45	20	0.666	12.4	142-521	5	E	142-400	6-12-63
27	0.035	0.026	1.757	30	45	20	1.000	50	142-520	--	E	142-400	6-26-63
28	0.035	0.026	1.000	30	30	20	1.000	7.6	--	--	P	142-600	6-28-63
29	0.035	0.026	1.000	30	30	20	1.000	50	142-603	--	E	142-600	7-2-63
30	0.035	0.026	1.000	30	30	20	1.000	50	142-603	--	P	142-600	7-15-63

summarized by test number. The date in the last column specifies the beginning date of the test.

Table 5 lists the major components, with the corresponding drawing numbers, for the three thruster series discussed. This Table provides the key to finding the components of a thruster assembly tested under a particular series and test number. It will be noted that certain parts are used for both the series 142-400 designs as well as the series 142-600 designs.

Some minor design changes were made and tested for which no drawings are shown in this report. However, these changes are described briefly in the "comment" column in Table 5.

2.2 Internal Flow Passage Analysis

2.2.1 Series 142-400

2.2.1.1 Geometry of the Flow Passage

With the constricted arc configuration high velocities occur in the anode inlet region, in the throat, and in the nozzle. These three regions influence the performance of an arc-jet engine directly in terms of cathode-anode cooling, arc stabilization, heat transfer from the arc to the propellant, and thrust after expansion in the nozzle. At a given mass flow the flow pattern is governed primarily by the minimum inlet area and by the throat area. The throat area is simply the cross-sectional area of the cylindrical bore in the anode. The minimum inlet area is defined as the smallest flow section between the anode and cathode.

The areas A_{\min} and A_{th} were part of the parametric investigation as described in paragraph 2.1. For Tests No. 1 through 6, constants and variables are shown in Table 2. The relation between the cathode gap setting s and the throat diameter D_{th} for a constant area ratio $A_{\min}/A_{th} = \text{constant}$ was found by the method described in the following paragraph.

A_{\min} may be approximated as a cut of a cone of which the large diameter is equal to the throat diameter and of which the generating line is perpendicular to the generating line of the cathode cone. This is an approximation only because orthogonality of the two generating lines does not necessarily define A_{\min} as will be shown later. However, the assumption above is sufficient for parametric studies.

TABLE 5
SUMMARY OF ALL THRUSTOR DESIGNS TESTED

Group	Common Parts	Parts Exchanged	Drawing Number	Test Number	Comment
142-300	Assembly Drawing		142-300		
142-300	Modification		142-300A		
142-400	Assembly Drawing		142-400	1-22	
142-400	Thrustor Housing Subassembly		142-500	23	Test Number 23 used the cathode Insulator 142-515 modified with an additional gas passage on the outside
142-400	Thrustor Housing		142-501	25, 26	
142-400	Cathode		142-506	24-27	
142-400		Cathode Insulator	142-515		
142-400	Cathode Holder		142-505		Test Number 25, 28 used the cathode Insulator 142-515 and the anode Insert 142-519 modified as shown in Fig. page
142-400	Cathode Connector		142-503		
142-400	Retaining Cap		142-508		
142-400	Rear Insulator		142-504		
142-400	Gas Connector		142-502		
142-400	Anode	Anode Insert	142-519		
142-400		Anode Insert	142-520	28, 29, 30	
142-600	Assembly Drawing		142-600		Test Number 28 employed the Cathode Insulator 142-601, but with 4 injector holes D_{inj} . Hole = 0.025" and a larger diameter of the vortex chamber $D_{vortex} = 0.165"$. The anode was essentially 142-603, but without a radiation disk, and $A_e/A_{th} = 7.6$.
142-600	Thrustor Housing		142-501		
142-600	Cathode		142-602		
142-600		Cathode Insulator	142-601		
142-600	Cathode Holder		142-505		
142-600	Cathode Connector		142-503		
142-600	Retaining Cap		142-508		
142-600	Rear Insulator		142-504		
142-600	Gas Connector		142-502		
142-600		Anode Insert	142-603		

The area of the cone cut becomes

$$A_{\min} = \pi(R \zeta_2 - r \zeta_1) \quad (1)$$

$$\zeta_1 = \frac{2}{3} \sqrt{3} r$$

$$\zeta_2 = \frac{2}{3} \sqrt{3} R$$

Then, eq. (1) reduces to

$$A = \frac{2}{3} \pi \sqrt{3} (R^2 - r^2)$$

It is

$$h = R - r$$

$$\left. \begin{aligned} s_1 &= \frac{h}{\tan 30^\circ} = \sqrt{3} h \\ s_2 &= \frac{h}{\tan 60^\circ} = \frac{\sqrt{3}}{3} h \end{aligned} \right\} \text{Fig. 2.7}$$

$$s = s_1 + s_2 = \frac{4}{3} \sqrt{3} h \text{ and } h = \frac{1}{4} \sqrt{3} s$$

Therefore,

$$R - r = \frac{\sqrt{3}}{4} s \quad \text{and} \quad r = R - \frac{\sqrt{3}}{4} s$$

The flow area A_{\min} may be expressed as

$$A_{\min} = \frac{2}{3} \pi \sqrt{3} (R + r)(R - r), \quad \text{or}$$

$$A_{\min} = \frac{2}{3} \pi \sqrt{3} \left(2R - \frac{\sqrt{3}}{4} s\right) \frac{\sqrt{3}}{4} s, \text{ or with the substitution } D_{th} = 2R$$

$$A_{\min} = \frac{\pi}{2} s \left(D_{th} - \frac{\sqrt{3}}{4} s\right) \quad (3)$$

Equation (3) is valid for $r \geq 0$ or $s \leq \frac{2}{3} \sqrt{3} D_{th}$

$$\text{For } r = 0, \quad h = \frac{D_{th}}{2} \quad \text{and} \quad s = \frac{2}{3} \sqrt{3} D_{th}$$

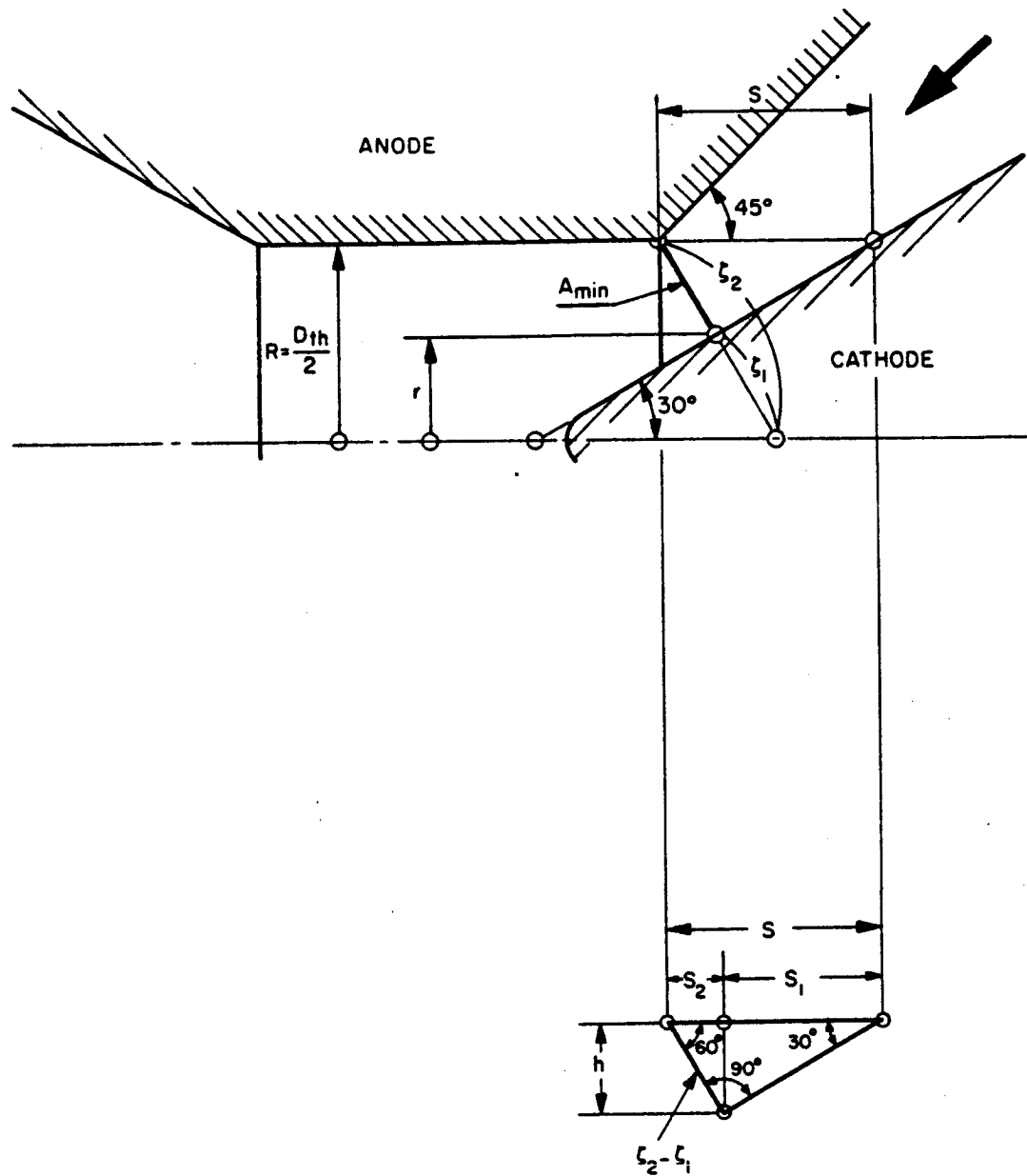


Figure 2.7 Diagram of Cathode-Anode Geometry and Geometry of Cathode Gap Region

Since $A_{\min}/A_{th} = c$ ($c = 0.666$)

and $A_{th} = \frac{\pi}{4} D_{th}^2$, there is

$$\frac{2s(D_{th} - \frac{\sqrt{3}}{4}s)}{D_{th}^2} = c, \text{ or}$$

$$\frac{\sqrt{3}}{2} \left(\frac{s}{D}\right)^2 - 2\left(\frac{s}{D}\right) + c = 0$$

$$\left(\frac{s}{D}\right)_{1,2} = \frac{2 \pm \sqrt{4 - 2\sqrt{3}c}}{\sqrt{3}} = \frac{2\sqrt{3} \pm \sqrt{6(2 - \sqrt{3}c)}}{3}$$

The maximum value $\left(\frac{s}{D_{th}}\right)$ was shown earlier to be equal

to $\frac{2}{3}\sqrt{3}$. Therefore, the positive sign in the quadratic equation has no geometric meaning within the range $0 \leq \frac{s}{D_{th}} \leq \frac{2}{3}\sqrt{3}$.

The gap-diameter ratio becomes:

$$\frac{s}{D_{th}} = \frac{2\sqrt{3} - \sqrt{6(2 - \sqrt{3}c)}}{3}, \text{ and with } c = 0.666$$

$$\frac{s}{D_{th}} = 0.41 \quad (4)$$

Table 6 lists the cathode gap setting "s" as a function of the throat diameter D_{th} for the area ratio $A_{\min}/A_{th} = 0.666$.

TABLE 6
Tabulation of Minimum Flow Sections

D_{th} (in)	s (in)	A_{min} (sq. in)
0.015	0.006	117 . 810 x 10 ⁻⁶
0.020	0.008	209 . 439 x 10 ⁻⁶
0.025	0.010	327 . 249 x 10 ⁻⁶
0.030	0.012	471 . 238 x 10 ⁻⁶
0.035	0.014	641 . 408 x 10 ⁻⁶

It has long been apparent that in very small arc-jet thrusters, such as the one under investigation here, anode and cathode cooling problems are unusually difficult because of the very low propellant flow rates. In the 142-400 design the problem was attacked both analytically and experimentally in an effort to better understand the nature of the fluid flow patterns and heat transfer mechanisms in the constricted inlet region. The first step was to establish the flow sections between the cathode and the anode. From this calculation the exact value of A_{min} was deduced and compared to the approximate value obtained in the previous calculation.

The constrictor inlet region consists of the flow passage formed by two concentric cones whose generating lines are "a" for the anode, and "c" for the cathode (see Fig. 2.8).

The flow area between "a" and "c" is a function of x_0 . Let the points $P_0(x_0, y_0)$ and $P(\xi, \eta)$ on the contour of the anode and cathode respectively. For a given point P_0 there is one curve containing P_0 and intersecting with "c" at P, which is the generating line of a surface of revolution defining the smallest area with respect to P_0 . In the calculation the smallest surface of revolution is taken as the minimum surface element of a cone "d" with the half angle γ and the point P_0 on its generating line. Thus, the problem may be formulated as one of finding the half angle γ which produces the smallest frustum for a given point P_0 . It is necessary to recognize that the problem is of spatial character and not as simple as it might at first appear because the smallest flow area associated with the point P_0 is not necessarily determined by the shortest distance between P_0 and "c". The origin of the coordinate system coincides with the apex of the cathode cone as shown in Figure 2.8 (a) The cathode tip is assumed to be pointed, or having a small radius only. Figure 2.8 (b) shows schematically the flow area as a function of x_0 .

The flow area may be written as:

$$a = \pi(y_0 + \eta) \sqrt{(\xi - x_0)^2 + (\eta - y_0)^2} \quad (5)$$

$$\xi = \xi(\gamma)$$

$$\eta = \eta(\gamma)$$

The angle γ of the minimum flow area is established by

$$\frac{d}{d \tan \gamma} [a (\tan \gamma)] = 0 \quad (6)$$

With the substitutions $\tan \gamma = m$ and $\tan \gamma_0 = m_0$, the coordinates ξ and η become:

$$\xi = \frac{y_0 - m x_0}{m_0 - m} \quad (7)$$

$$\eta = \frac{m_0}{m_0 - m} (y_0 - m x_0) \quad (8)$$

Differentiation of equation (5) gives

$$\frac{1}{\pi} \left(\frac{da}{dm} \right) = \frac{\partial \eta}{\partial m} \sqrt{(\xi - x_0)^2 + (\eta - y_0)^2} + (y_0 + \eta) \frac{\left[(\xi - x_0) \frac{\partial \xi}{\partial m} + (\eta - y_0) \frac{\partial \eta}{\partial m} \right]}{\sqrt{(\xi - x_0)^2 + (\eta - y_0)^2}} \quad (9)$$

Taking the first derivative of equations (7) and (8) gives

$$\frac{\partial \xi}{\partial m} = \frac{y_0 - m_0 x_0}{(m_0 - m)^2} \quad (10)$$

$$\frac{\partial \eta}{\partial m} = m_0 \left(\frac{\partial \xi}{\partial m} \right) \quad (11)$$

Substituting equations (9) and (11) into equation (6) gives

$$m_0 \frac{\partial \xi}{\partial m} \frac{\sqrt{(\xi - x_0)^2 + (\eta - y_0)^2} + (y_0 + \eta) \left[(\xi - x_0) \frac{\partial \xi}{\partial m} + m_0 \frac{\partial \xi}{\partial m} (\eta - y_0) \right]}{\sqrt{(\xi - x_0)^2 + (\eta - y_0)^2}} = 0 \quad (12)$$

Since $\frac{\partial \xi}{\partial m} \neq 0$, equation (12) may be divided by $\frac{\partial \xi}{\partial m}$

Thus,

$$m_0 \left[(\xi - x_0)^2 + (\eta - y_0)^2 \right] + (y_0 + \eta) \left[(\xi - x_0) + m_0 (\eta - y_0) \right] = 0 \quad (13)$$

After replacing ξ and η by their equivalent terms, we obtain from equation (13) a quadratic equation with respect to m :

$$\begin{aligned} & \left[2 m_0^2 x_0 (m_0 x_0 - y_0) \right] m^2 + \\ & \left[m_0^2 x_0^2 - y_0^2 - 2 m_0^2 y_0 (m_0 x_0 - y_0) \right] m + \\ & \left[3 m_0 y_0^2 - 4 m_0^2 x_0 y_0 + m_0^3 x_0^2 \right] = 0 \end{aligned} \quad (14)$$

With the following substitutions

$$u = \left[2 m_0^2 x_0 (m_0 x_0 - y_0) \right] \quad (15a)$$

$$v = \left[m_0^2 x_0^2 - y_0^2 - 2 m_0^2 y_0 (m_0 x_0 - y_0) \right] \quad (15b)$$

$$w = \left[3 m_0 y_0^2 - 4 m_0^2 x_0 y_0 + m_0^3 x_0^2 \right] \quad (15c)$$

the quadratic equation reduces to

$$u m^2 + v m + w = 0$$

and

$$m_{1,2} = \frac{-v \pm \sqrt{v^2 - 4uw}}{2u} \quad (16)$$

The value m has only one valid solution. It can readily be seen that for the notation chosen in Figure 2.8 m is always negative ($90 < \gamma < 180^\circ$). In equation (15a) the term in parenthesis ($m_0 x_0 - y_0$), is negative since $y_0 > m_0 x_0$ (compare with Figure 2.8. Thus, u is always negative.

The expression for w in equation (15 c) can be written as

$$\frac{w}{m_0} = \left[3 y_0^2 - 4 m_0 x_0 y_0 + (m_0 x_0)^2 \right]$$

Looking at the sign of w we have to consider two limits, namely $m_0 \ll 1$ and $m_0 x_0 = y_0$. In the first case we find $\frac{w}{m_0} = 3 y_0^2$ and in the second case

$\frac{w}{m_0} = 0$. Therefore, w is always positive. Finally, the parameter v in equation (15b) may be expressed in the following form

$$v = (m_0 x_0 - y_0) (m_0 x_0 + y_0 - 2 m_0^2 y_0).$$

Whereas the first factor in the expression above is always negative, the second one may be positive or negative. As a result, v is either positive or negative.

Concluding, we find that the root $\sqrt{v^2 - 4uw}$ in the expression for m assumes a value always greater than $|v|$. Making use of the fact that m is always negative, the minus sign in the quadratic expression for m must be truncated.

$$m = \frac{\text{Thus, } -v + \sqrt{v^2 - 4uw}}{2u}$$

In order to simplify the calculation it is convenient to express the equations in dimensionless form.

With $\eta = m_0 \xi$ and $\frac{x_0}{y_0} = R$ the dimensionless flow area

becomes

$$A = \frac{a}{y_0^2} = \pi \left[\frac{m_0}{m_0 - m} (1 - mR) + 1 \right] \sqrt{\left[\frac{1}{m_0 - m} (1 - mR) - R \right]^2 + \left[\frac{m_0}{m_0 - m} (1 - mR) - 1 \right]^2} \quad (17)$$

and, for the parameters u, v, w , we obtain

$$U = \frac{u}{y_0^2} = 2 m_0 R (m_0 R - 1) \quad (18a)$$

$$V = \frac{v}{y_0^2} = m^2 R^2 - 2 m_0^2 (m_0 R - 1) - 1 \quad (18b)$$

$$W = \frac{w}{y_0^2} = 3 m_0 - 4 m_0^2 R + m_0^3 R^2 \quad (18c)$$

The tangent of the angle γ is

$$m = \frac{-V + \sqrt{V^2 - 4UW}}{2U} \quad (19)$$

For equation (17) two distinct cases are of interest

$$\begin{cases} m = 0 \\ \gamma = 180^\circ \end{cases} \quad \text{and} \quad \begin{cases} m = \infty \\ \gamma = 90^\circ \end{cases}$$

$$A \Big|_{m=0} = 2\pi \left(\frac{1}{m_0} - R \right), \text{ since } y_0 = \eta \text{ at } \gamma = 180^\circ$$

$$\frac{y_0}{m_0} = \frac{\eta}{m_0} = \xi \text{ and } y_0 R = x_0 \text{ thus,}$$

$$a \Big|_{m=0} = 2\pi y_0 (\xi - x_0)$$

which is the surface of a cylinder.

$$A \Big|_{m=\infty} = \pi (m_0 R + 1) (m_0 R - 1) = \pi \left[(m_0 R)^2 - 1 \right]$$

which is the area of an annulus.

The range of R for a given m_0 becomes:

If $A = 0$ then,

$$\left[\frac{m_0}{m_0 - m} (1 - mR) + 1 \right] = 0$$

and also

$$\sqrt{\left[\frac{1}{m_0 - m} (1 - mR) - R \right]^2 + \left[\frac{m_0}{m_0 - m} (1 - mR) - 1 \right]^2} = 0$$

The latter expression leads to a relationship between R and m_0 , namely

$$R = \frac{1}{m_0}$$

Consequently, $y_0 = x_0 m_0 = \eta$

The geometric meaning of $y_0 = \eta$ where $m \neq 0$ and $m \neq \infty$, is the coincidence of the two points P_0 and P .

$$\begin{aligned} \gamma_0 = 30^\circ ; m_0 &= \frac{\sqrt{3}}{3} & 0 \leq R \leq \sqrt{3} \\ \gamma_0 = 45^\circ ; m_0 &= 1.0 & 0 \leq R \leq 1.0 \end{aligned}$$

The dimensionless parameter A , representing the exact flow section in the anode inlet and constrictor region, was calculated for $\gamma_0 = 30^\circ$ with R as parameter. The data are summarized on Table 7. The minimum flow sections were recalculated for the geometries applied in Tests No. 1 through 6. Table 8 shows the comparison of A_{\min}/A_{th} between the approximate and exact method. The actual area ratio A_{\min}/A_{th} is approximately 1.5% greater than the proposed ratio of 0.666. The deviation is not a severe error for a parametric type of investigation.

TABLE 7
Flow Areas in The Anode

R = 0.1	TAN GAMMA = -5.9002	ARC TAN GAMMA = -1.4029	A = 3.12257
R = 0.2	TAN GAMMA = -3.8342	ARC TAN GAMMA = -1.3157	A = 3.07352
R = 0.3	TAN GAMMA = -3.0260	ARC TAN GAMMA = -1.2516	A = 3.00026
R = 0.4	TAN GAMMA = -2.5724	ARC TAN GAMMA = -1.2000	A = 2.90547
R = 0.5	TAN GAMMA = -2.2739	ARC TAN GAMMA = -1.1565	A = 2.79079
R = 0.6	TAN GAMMA = -2.0588	ARC TAN GAMMA = -1.1186	A = 2.65735
R = 0.7	TAN GAMMA = -1.8943	ARC TAN GAMMA = -1.0851	A = 2.50598
R = 0.8	TAN GAMMA = -1.7632	ARC TAN GAMMA = -1.0549	A = 2.33735
R = 0.9	TAN GAMMA = -1.6556	ARC TAN GAMMA = -1.0274	A = 2.15199
R = 1.0	TAN GAMMA = -1.5650	ARC TAN GAMMA = -1.0022	A = 1.95035
R = 1.1	TAN GAMMA = -1.4873	ARC TAN GAMMA = -0.9789	A = 1.73280
R = 1.2	TAN GAMMA = -1.4197	ARC TAN GAMMA = -0.9571	A = 1.49966
R = 1.3	TAN GAMMA = -1.3600	ARC TAN GAMMA = -0.9368	A = 1.25123
R = 1.4	TAN GAMMA = -1.3069	ARC TAN GAMMA = -0.9176	A = 0.98775
R = 1.5	TAN GAMMA = -1.2591	ARC TAN GAMMA = -0.8996	A = 0.70945
R = 1.6	TAN GAMMA = -1.2157	ARC TAN GAMMA = -0.8824	A = 0.41653
R = 1.7	TAN GAMMA = -1.1761	ARC TAN GAMMA = -0.8661	A = 0.10919

Symbols:

$R = \frac{x_0}{y_0}$: Coordinate ratio of point P_0

TAN GAMMA = $m = \tan \gamma$: Tangent of the angle which defines the flow area

ARC TAN GAMMA = γ : Angle defining the flow area

$A = \frac{a^2}{y_0^2}$: Flow area in dimensionless form

For definitions and explanations see paragraph 2.2.1.1 and Figure 2.8

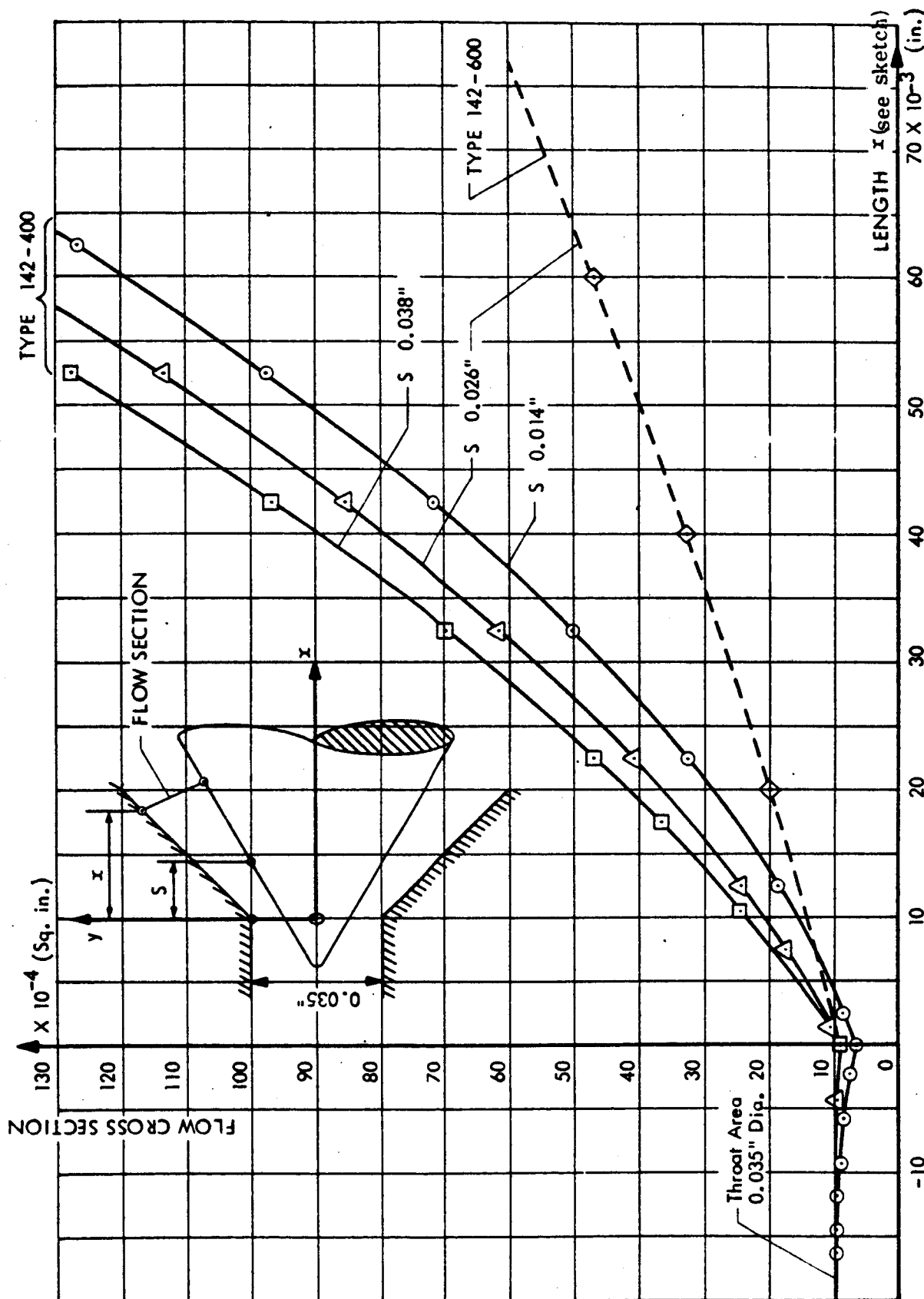


Figure 2.9 Flow Section in the Constrictor at Variable Cathode Gap Settings

~~CONFIDENTIAL~~

TABLE 8
Calculated Values of Minimum Area to Throat Area Ratio

Test Number	A _{min} /A _{th}		Deviation %
	Approximate	Exact	
1	0.666	0.674	1.20
2	0.666	0.678	1.80
3	0.666	0.674	1.20
4	0.666	0.675	1.35
5	0.666	0.673	1.05
6	0.666	0.676	1.50

Figure 2.9 shows the flow sections for the geometries employed in Tests No. 13 through 18. For parametric studies, it is necessary to consider the fact that not only the size but also the shape of the flow area changes with varying gap settings.

2.2.1.2 Flow Through the Constrictor

The flow through the constrictor is a three dimensional problem. Using cylindrical coordinates the dynamic and thermodynamic properties of the gas are functions of x , r , and φ . In the constrictor inlet region the tangential velocity $r \frac{d\varphi}{dt}$ is in the same order as the axial velocity $\frac{dx}{dt}$. The truncation of the third coordinate φ would lead to an incomplete picture of the flow patterns. However, the conventional one dimensional analysis may be applied if integrated properties such as average pressures and velocities are sufficient to explain certain phenomena.

The following calculation is based on slug flow. It gives a rough estimation of the axial pressure-and velocity distribution through the constrictor. The result proved to be useful for design purposes.

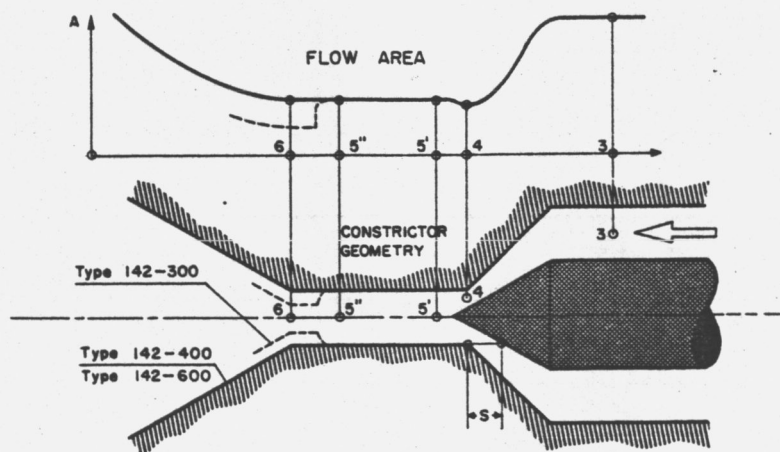


Figure 2.10. Schematic of Flow Cross-Sectional Areas in Arc Region

~~CONFIDENTIAL~~

The constrictor design shown in Figure 2.10 has two distinct sections which control the flow. They are represented by orifices 4 and 6 in Figure 2.10, with the flow areas A_4 and A_6 respectively. The ratio A_6/A_5 of engines 142-400 and 142-600 is unity. For all engine types the area A_4 may be smaller or equal to A_6 depending on the cathode gap setting s . In operation most of the heat will be transferred to the propellant between stations 4 and 6. For a simplified analysis it is reasonably accurate to assume that all of the gas heating occurs in the constant area section between stations 5' and 5''.

Both cold flow and hot flow conditions were investigated for both the 142-400 and 142-600 series thrusters.

Cold Flow Conditions

For expansion into a near-vacuum, sonic velocity occurs in station 4 ($A_4/A_6 < 1$). Between 4 and 5' some expansion takes place, with an increase in velocity. If the constrictor length is small compared to its diameter, the friction losses are small and the flow does not change from supersonic to subsonic condition between the station 5' and 6'.

The mass flow through a sonic orifice is calculated by

$$\dot{m} = A_4 \rho_{3st} \sqrt{\gamma R T_{3st}} \left(\frac{2}{\gamma + 1} \right)^{1/2 (\gamma + 1)/(\gamma - 1)} \quad (20)$$

where

\dot{m} = Mass flow

ρ = density

R = gas constant

T = Temperature

γ = ratio of specific heat

st = denotes the stagnant gas condition before entering the constrictor

The numerical subscript denotes the location as shown in Figure 2.10. Since the velocity V_3 is small, the total pressure may be replaced by the static pressure P_3 . The pressure P_3 upstream of the cathode tip becomes

$$P_3 = \frac{\dot{m} R T_3}{A_4 \sqrt{\gamma R T_3}} \left(\frac{2}{\gamma + 1} \right)^{1/2 (\gamma + 1)/(\gamma - 1)} \quad (21)$$

By introducing the atmospheric pressure P_o , equation (21) may be expressed in the following form:

$$\frac{P_3}{P_o} = \left[\frac{\dot{m} \sqrt{\gamma R T_3}}{\gamma P_o A_6} \left(\frac{\gamma + 1}{2} \right)^{1/2(\gamma + 1)/(\gamma - 1)} \right] \frac{1}{A_4/A_6} \quad (22)$$

The pressure ratio P_3/P_o is indirectly proportional to the area ratio A_4/A_6 , or in other words, the pressure function is of hyperbolic character with respect to the area.

The curve $\frac{P_3}{P_o} = f\left(\frac{A_4}{A_6}\right)$ was plotted (Fig. 2.11) for the following conditions:

$$\begin{aligned} \dot{m} &= 2 \times 10^{-5} \text{ lb/sec.} \\ T_3 &= 550^\circ \text{ R} \\ P_o &= 760 \text{ mmHg} \\ D_6 &= 0.035'' \\ R &= 2.466 \times 10^4 \text{ ft}^2/\text{sec}^2 \text{ } ^\circ\text{R} \\ \gamma &= 1.4 \end{aligned}$$

For these conditions the term in the brackets in equation (22) has the value 0.236, and the equation for P_3/P_o is reduced to

$$\frac{P_3}{P_o} = \frac{0.236}{A_4/A_6} \quad (23)$$

When the area ratio approaches unity, the curve flattens out. Thus, for $0.8 < (A_4/A_6) < 1$ there is no appreciable change in P_3 . This fact may be considered as the answer to the observation made in Tests 14 and 15, in which no significant changes in P_2 ($\approx P_3$) were measured, since A_4/A_6 was 0.863 and 1.0 for Tests 14 and 15 respectively.

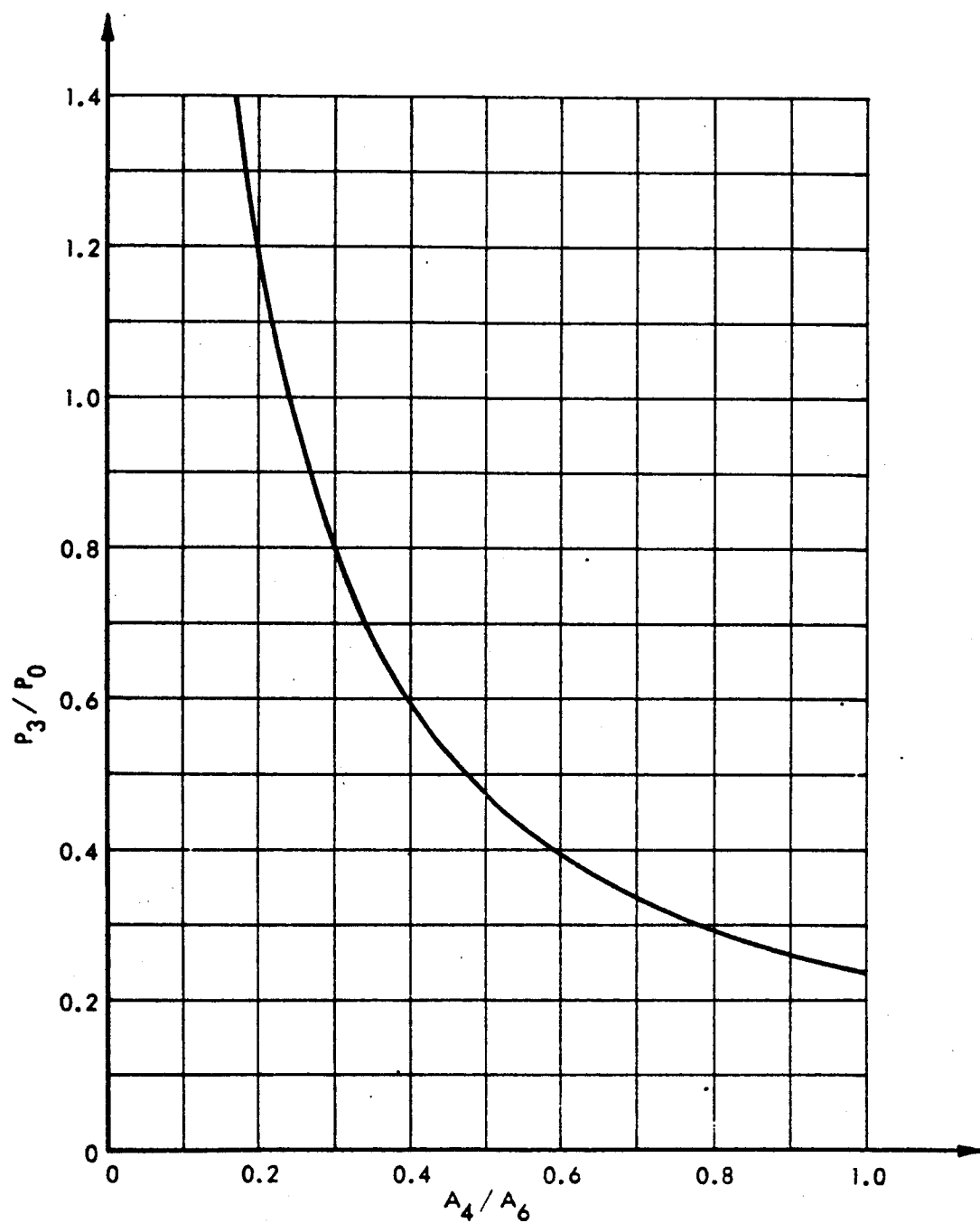


Figure 2.11 Flow Through the Constrictor - Cold Flow Condition
Upstream pressure ratio P_3/P_0 as a function of the opening area ratio A_4/A_6

Hot Flow Condition

The idealized thermodynamic process of an arc-jet engine is shown schematically in the enthalpy-entropy diagram of Figure 2.12

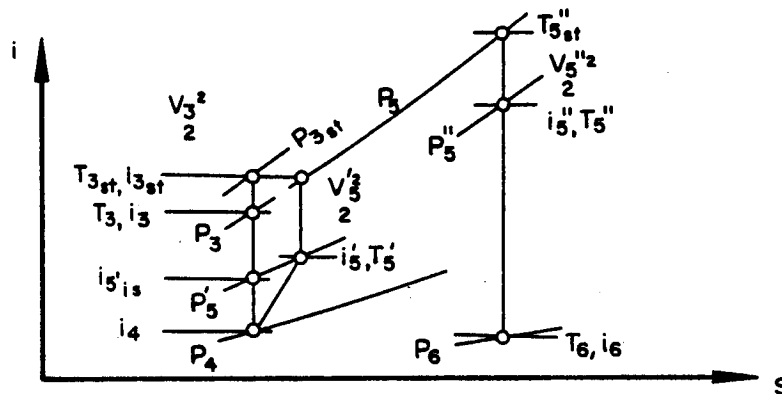


Figure 2.12 Enthalpy-Entropy Diagram for Arc Heating Process

The numerical subscripts refer to the stations shown in Figure 2.10

The subscript (st) stands for stagnation

The subscript (is) stands for isentropic

The superscript (') denotes the condition before heat transfer

The superscript (') denotes the condition after heat transfer

The gas expands isentropically from the vortex chamber (station 3) to the smallest flow section (station 4). At high enthalpies i_5'' the flow will choke before entering the nozzle. As a result the gas velocity between the stations 3 and 6 is in the subsonic flow regime. For the geometry A_4/A_5' ($A_4 = A_{\min}$ and $A_5' = A_{th}$) this flow passage is, in effect, a diffuser which causes the flow to decelerate with an accompanying pressure rise. The pressure rise is polytropic, with a compression efficiency denoted by η . The value of η depends on the shape of the constrictor contour between the sections 4 and 5'. The relationship between pressures, temperatures and velocities follows from the mass flow balance and conservation of energy, the perfect gas law and from the momentum theorem.

The conditions in the flow passages of the thruster type 142-600 have been analyzed using a gap setting $s = 0.026''$ and an operating condition $I_{sp} = 1000$ seconds. The flow area, pressure, velocity and local Reynolds numbers are plotted in Fig. 2.13. The Reynolds number was found to be in the laminar flow regime throughout.

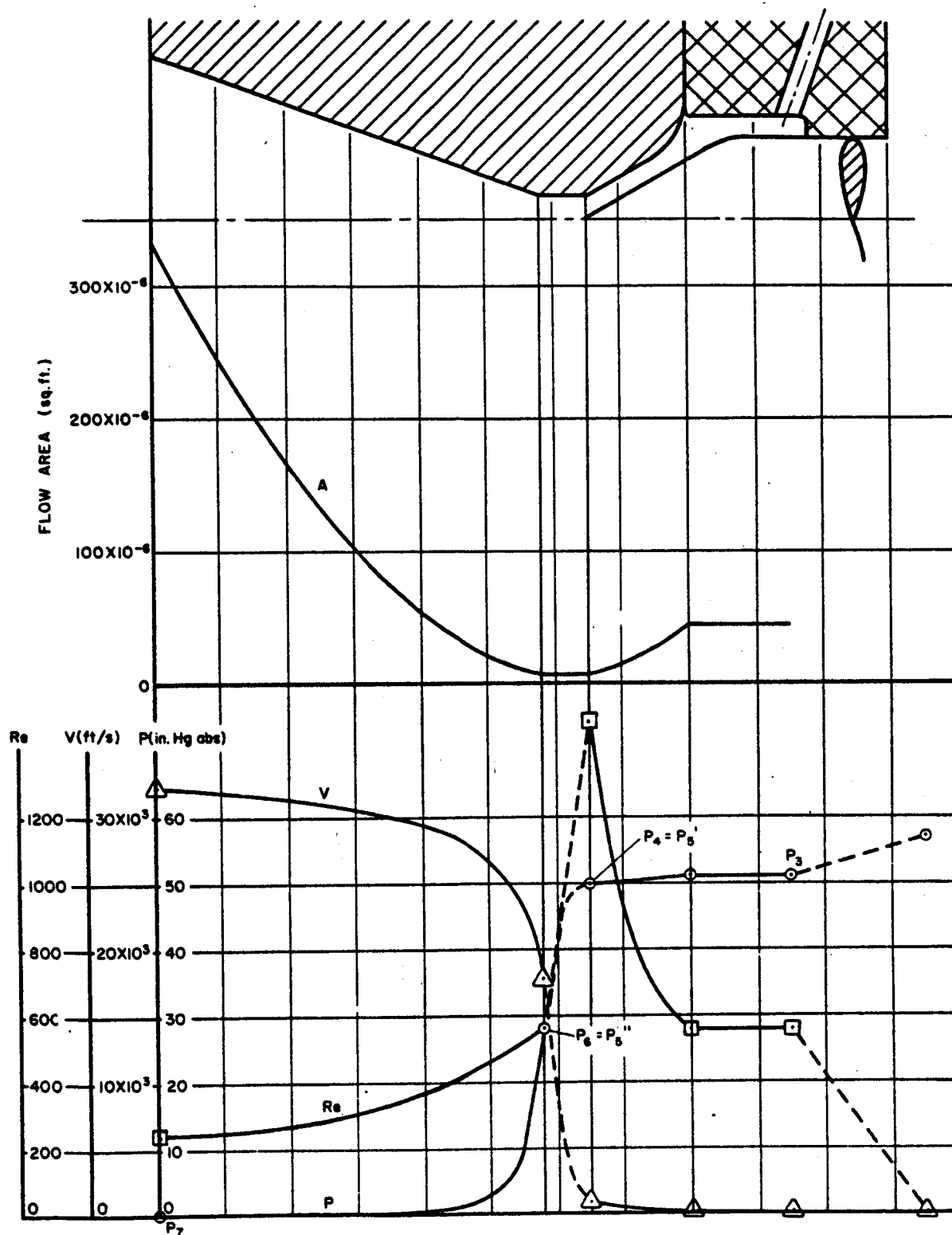


Figure 2.13 Plot of Flow Area, Velocity, Pressure, and Reynolds Number vs Axial Station - Hot Flow Condition (Type 142-600)

2.2.1.3 Friction in the Propellant Passages

Figure 2.11 shows schematically the propellant lines and flow passages

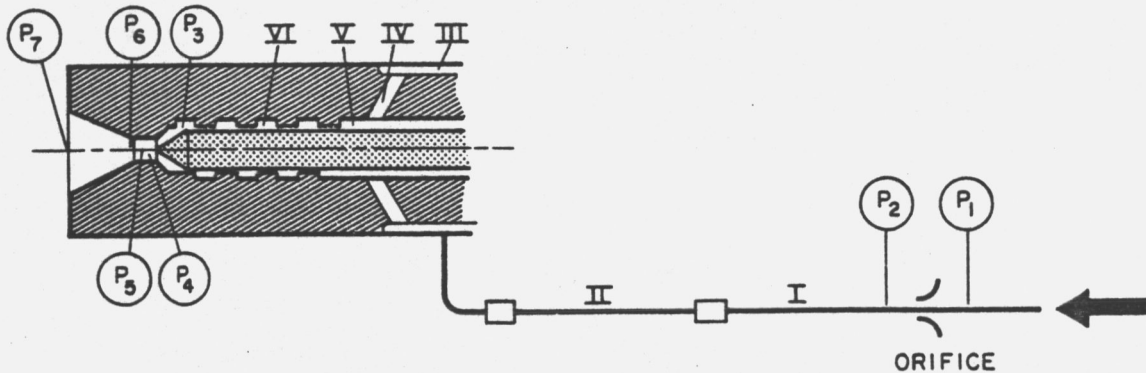


Figure 2.14 Schematic Diagram of Propellant Flow System

In the following analysis the pressure drop caused by friction is calculated for all segments between the flow meter and the constrictor in the arc-jet engine, based on cold flow throughout.

For pipe flow the pressure drop ΔP is

$$\Delta P = \lambda \frac{l}{D_e} \frac{\rho}{2} v^2 \quad (24)$$

- λ = friction coefficient ($\lambda = \lambda(Re)$)
- l = length of the line
- D_e = equivalent diameter
- ρ = density of the propellant
- v = velocity of the propellant

In addition to the frictional pressure losses in the passages, other pressure losses are caused by sudden area changes, obstructions, and bends. These losses can be calculated individually for each obstruction from the relation

$$\Delta P = \xi \frac{\rho}{2} v^2 \quad (25)$$

where ξ = loss coefficient for obstruction (for a sharp 90° angle $\xi = 0.5$)

$$\Delta P_{\text{total}} = \sum_I^{VI} \left[\frac{\rho}{2} v^2 \left(\lambda \frac{l}{D_e} + \xi \right) \right] \quad (26)$$

Data:

\dot{m}	=	2×10^{-5} lb/sec	Mass flow (Hydrogen)
P_2	\approx	20 psia	Pressure after orifice
R	=	766 ft/°R	Gas constant
μ	=	0.01 CP	Abs. viscosity
T_2	=	550°R	Temperature
ρ_2	\approx	0.007 lb/ft ³	Density (approx.)
ν	=	9.57×10^{-4} ft ² /s	Viscosity
R_e	=	$\frac{V D_e}{\eta \mu}$	Reynolds number
V	=	$\frac{\dot{m}}{\rho A}$	Velocity
D_e	=	$\frac{4 A}{u}$	Equivalent diameter

u = Wetted perimeter

A = Cross-sectional area

In Table 9, the pressure losses due to friction are summarized. The total amount of pressure drop calculated is 9.3 psi.

The friction loss may be extrapolated from "cold" to "hot" operating conditions as follows:

$$\Delta P \sim \rho V^2$$

Since $V \sim \frac{1}{\rho}$ the pressure drop is

$$\Delta P \sim \frac{1}{\rho}$$

$$\Delta P_{\text{hot}} \sim \left(\frac{\rho_{\text{cold}}}{\rho_{\text{hot}}} \right) \left(\frac{1}{\rho_{\text{cold}}} \right)$$

~~CONFIDENTIAL~~

TABLE 9
Friction Losses in the Propellant Passages

Passage	Number of Passages	Geometry	Length (in.)	Area (sq. in.)	De (in.)	ρ lb/ft ³	$\frac{L}{D_e}$	V (ft/s)	Re	$\frac{\rho}{2} V^2$ (lb/ft ²)	ΔP (psi)
I	1	Pipe	222	0.0270	0.186	0.007	1190	15.2	246	0.025	0.3
II	1	Pipe	78	0.0086	0.105	0.007	740	47.7	437	0.246	1.4
III	1	Annulus	1	0.0220	0.030	0.007	33	18.6	48	0.037	0.0
IV	4	Hole	0.212	0.0008	0.032	0.007	7	128	356	1.780	0.1
V	1	Annulus	0.913	0.0037	0.018	0.007	50	111	174	1.330	0.5
VI	2	Thread	2.16	0.0007	0.023	0.007	94	293	588	9.330	7.0

Total pressure drop $\Delta p_{tot} = 9.3$ psi

~~CONFIDENTIAL~~

$$\frac{\rho_{\text{cold}}}{\rho_{\text{hot}}} = \left(\frac{P_{\text{cold}}}{P_{\text{hot}}} \right) \left(\frac{T_{\text{hot}}}{T_{\text{cold}}} \right)$$

$$P_{\text{cold}} \approx 20 \text{ psia}$$

$$P_{\text{hot}} \approx 40 \text{ psia}$$

$$T_{\text{cold}} \approx 550^{\circ}\text{R}$$

$$T_{\text{hot}} \approx 1000^{\circ}\text{R} \quad (\text{in the region of the highest friction})$$

The density ratio becomes:

$$\frac{\rho_{\text{cold}}}{\rho_{\text{hot}}} = 0.5 \times 1.8 = 0.9$$

There is no significant difference between the densities ρ_{cold} and ρ_{hot} ; therefore the friction losses are about the same in both conditions. As a result, the pressure P_3 (before anode inlet) is approximately 10 psi below the pressure P_2 (after flow meter).

2.2.2 Series 142-600

2.2.2.1 Geometry of the Flow Passage

The constrictor geometry of the type 142-600 is characterized by a short throat with $L_{\text{th}}/D_{\text{th}} = 1$, and with 30° half angles on both the cathode tip and the anode inlet. The inlet flow area is plotted in Figure 2.9. The flow areas are as much as 50% smaller in the series 142-600 thrusters compared to series 142-400 thrusters with the same gap setting $s = 0.026''$.

2.2.2.2 Flow Through the Constrictor

Effective cathode and anode cooling in the inlet region requires a high flow velocity. The absolute velocity is the sum of the axial and tangential velocity vectors. The new 142-600 design provides an increase in both vectors over the earlier 142-400 design. The angular velocity is increased as a result of the stronger vortex generated by the injector holes near the anode inlet.

~~CONFIDENTIAL~~

Figure 2.15 indicates the flow pattern in the vortex chamber.

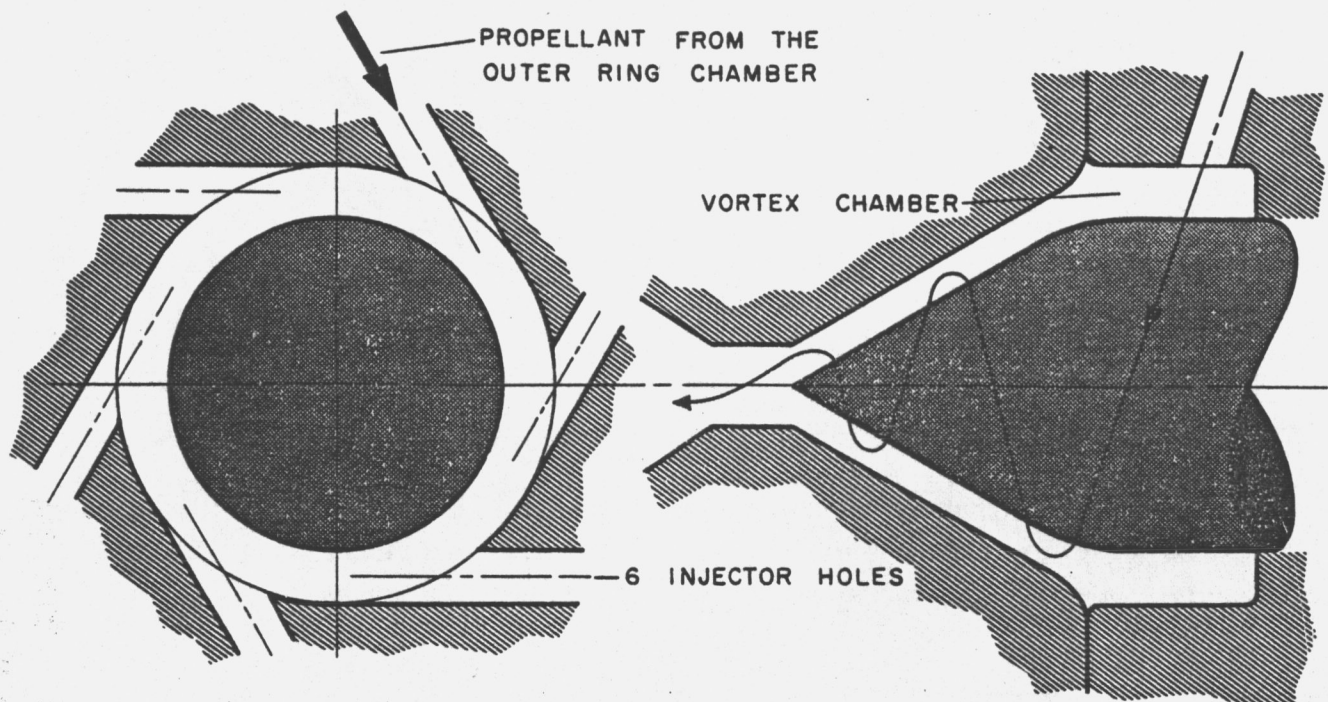


Figure 2.15 Sketch of Propellant Flow Pattern in Vortex Chamber of Series 142-600 Thrustors

Table 10 summarizes the geometries and flow velocities in the different propellant passages. The data are based on an average density

$$\rho = 4.7 \times 10^{-3} \text{ lb/ft}^3 \text{ (p = 25 psia, T = 1000}^\circ\text{R)} \text{ and } \dot{m} = 3 \times 10^{-5} \text{ lb/sec}$$

TABLE 10
Flow Passage Geometry and Flow Velocities in Series 142-600 Thrustors

Part	Name	Number	Diameter (in.)	Total Cross Section (ft ²)	Velocity (ft/s)
1	Thread (Cathode insulator)	1	---	52×10^{-6}	123
2	Inj. hole	6	0.018	10.6×10^{-6}	602
3	Vortex Chamber axial	1	0.155/0.125	45.5×10^{-6}	140
4	Throat	1	0.035	6.66×10^{-6}	5880*

*Sonic velocity $V_s = \sqrt{\gamma RT}$ (no heat added)

The injector holes are inclined by 20° to the vertical to impart some axial velocity. The axial velocity in the vortex chamber was calculated as 140 ft/sec (Table 10). The axial velocity imposed by the injector hole becomes

$$V_{\text{axial}} = V_{\text{hole}} \times \sin 20^\circ = 206 \text{ ft/sec}$$

Because of an increase in cross section from the injector hole to the vortex chamber, the latter velocity will be reduced so that the two axial velocity vectors are about of the same magnitude.

The exact calculation of the flow pattern in the constrictor inlet region could not be finished within the contract period because the description of the decay of the vortex through the action of viscosity and surface friction constitutes a very complex problem. However, it might be instructive to estimate the angular velocity in the throat by making the following assumptions:

- 1) Half of the kinetic energy of the propellant in the injector orifice is lost due to friction in the vortex chamber.
- 2) The flow from the vortex chamber to the throat is potential flow.

For the above assumptions, the effective tangential velocity in the vortex chamber becomes

$$V_{\text{eff}} = \sqrt{0.5 (V_{\text{hole}} \times \cos 20^\circ)^2} = 400 \text{ ft/sec}$$

The vortex strength may be expressed by the circulation

$$\Gamma = \oint \vec{V} \cdot d\vec{s} = 2 \pi r^2 \omega$$

where r = radius
 ω = angular velocity

Hence, the tangential velocity as a function of the diameter reduces to

$$\frac{D}{D_0} = \frac{V}{V_0}$$

Looking at the throat diameter $D = 0.035''$, the corresponding tangential velocity is calculated as

$$V_{\text{throat}} = V_{\text{chamber}} \times \frac{D_{\text{chamber}}}{D_{\text{throat}}} = 1600 \text{ ft/sec}$$

The axial velocity near the cathode tip was found to be of the order of 970 ft/sec. Both components add up to the absolute velocity $V_{\text{abs}} = 1870 \text{ ft/sec}$

Consideration of the heat transfer mechanisms indicates that 142-400 and 142-600 designs have the same Graetz number and consequently the same Nusselt number. Hence, the ratio of the heat transfer coefficients may be expressed by

$$\frac{h_2}{h_1} = \sqrt{\frac{A_1}{A_2}} \approx \sqrt{\frac{U_2}{U_1}} \approx \sqrt{2}$$

A = flow section

h = heat transfer coefficient

u = total velocity

The subscripts 1 refers to the 142-400 designs

2 refers to the 142-600 designs

The cathode tip of the 142-600 thruster releases about 40% more heat to the propellant than the cathode tip of the 142-400 thruster.

An intensive surface cooling of the cathode tip is also advantageous from the point of restarting. Near the rim of an eroded cathode the electric field is higher because of the edge effect. The arc tends to strike off-center after restart. In order to avoid a non-uniform energy flux, the arc foot on the cathode should be displaced from point 1 to point 2 (Figure 2.16). A good surface cooling lowers the rim temperature. The highest temperature gradually builds up on the center line where no convective cooling takes place. As a result the greatest electron emissivity occurs near point 2 which subsequently becomes the location of the arc foot.

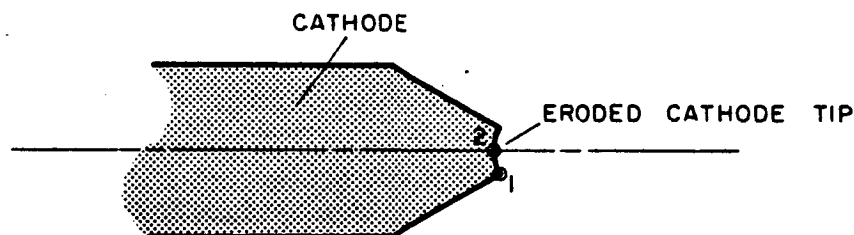


Figure 2.16 Sketch of Cathode Tip Configuration After Erosion

2.2.2.2 Friction in the Propellant Passages

The total pressure drop due to friction between the flow meter and the vortex chamber was calculated as $\Delta P_{\text{tot}} = 3$ psi. The injector holes are practically the only restriction upstream of the throat; therefore, the friction losses are smaller than those in thruster 142-400.

2.3 Anode Design and Heat Transfer in Anode

2.3.1 Series 142-400

The original anode design of the thruster 142-400 had an undercut (Figure 2.17) to provide some convective cooling near the hot spot region.

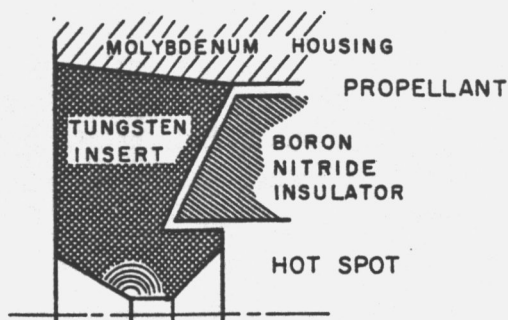
~~CONFIDENTIAL~~

Figure 2.17 Original Anode Insert With Undercut Series 142-400 Thrustor

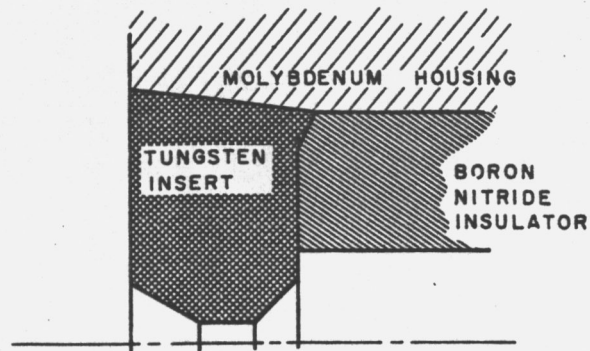


Figure 2.18 Modified Anode Insert With Undercut Eliminated Series 142-400 Thrusters

It was found that the heat picked up by convective cooling was a fraction of the heat conducted radially to the outside and radiated to the surroundings. Hence, the undercut acted as somewhat of a heat dam. The NASA Technical Monitors suggested that the undercut be eliminated in order to allow a better radial heat conduction (Figure 2.18). This design change was made, but it alone did not provide the desired improvement as far as life was concerned. (Test No. 25, 26 - 1 hour test).

The introduction of a longer nozzle with area ratio = 50, shown in Figure 2.19, proved to be more successful in terms of heat dissipation from the hot regions.

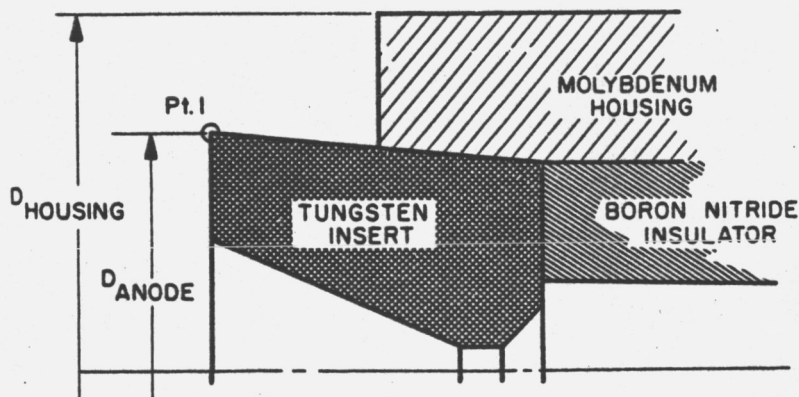


Figure 2.19 Second Modification of Anode Insert-Series 142-400

~~CONFIDENTIAL~~

The front portion of the anode extended forward of the thruster housing at a diameter ratio $\frac{D_{\text{anode}}}{D_{\text{housing}}} = 0.5$, providing increased heat dissipation by radiation in test

No. 27, a 25 hour test.

2.3.2 Series 142-600

A further development of the design shown in Figure 2.19 was achieved by the addition of a radiation disk (Drawing 142-600). Pyrometric readings near point 1 (Figure 2.18) indicated a 100° C lower temperature after increasing the disk diameter ratio from 0.5 to 1.0 (width of the disk = 0.150"). This new design reduced the temperature gradient considerably. Erosion due to excessive overheating was eliminated to a large extent. (Tests No. 29 and 30 - 150 hour test).

2.4 Optimum Nozzle Performance

In order to increase thruster performance and at the same time permit a higher mass flow for better life at the specified design point operating conditions, a detailed analysis was made to optimize the geometry of a supersonic nozzle operating in the laminar flow regime in terms of divergence angle and area ratio, taking into account the effects of friction and non-axial flow.

The exhaust nozzles of electric propulsion devices operate mostly in the laminar flow regime. In any complete analysis many "non-ideal" factors must be taken into account, including the effects of wall friction, non-axial flow, heat transfer between the propellant and the nozzle walls, atomic and ionic recombination, flow rotation, flow separation, and radially non-uniform distributions of velocity and energy flux at the nozzle inlet.

The problem of fully optimizing nozzles under these circumstances is very complex. A major simplification was made in this case in that the only non-ideal effects taken into account in the analysis were wall friction and non-axial flow. It was the purpose of this investigation to guide experimental work rather than to analyze the problem thoroughly. The result is restricted to a conical nozzle, and no attempt has been made to find the optimum contour or shape.

Furthermore, the calculation of the friction losses is simplified by considering a short nozzle element as a pipe; thus, the Hagen-Poiseuille theorem for laminar flow could be applied. The theorem is based on a parabolic velocity distribution. The bell shaped curve of the velocity profile in an arc-jet engine may be

approximated by a parabola without introducing too large an error.

In most cases friction losses are combined with an entropy increase. In this calculation reheating of the gas is neglected; the expansion process is assumed to be isentropic.

The result is shown on Figure 2.20. The ratio of the squares of the velocities of a real and an ideal nozzle $\left(U/U_{\text{ideal}}\right)^2$ is plotted as a function of the exit area ratio A/A_0 with the divergent half angle θ as a parameter. Since the square of the velocity is proportional to the kinetic energy, the ratio $\left(U/U_{\text{ideal}}\right)^2$ represents the nozzle efficiency based on the semi-ideal assumptions described above.

Symbols

f = Friction force	r = Radius
p = Pressure	a = Length
ρ = Density	L = Length
v = Specific volume	ν = Kinematic viscosity
T = Temperature	μ = Absolute viscosity
γ = Isentropic exponent	R_e = Reynolds number
C_p = Specific heat at constant pressure	θ = Divergence half angle
R = Gas constant	α = Angle
i = Enthalpy	λ = Friction coefficient
u = Velocity	\dot{m} = Mass flow
M = Momentum	t = Time

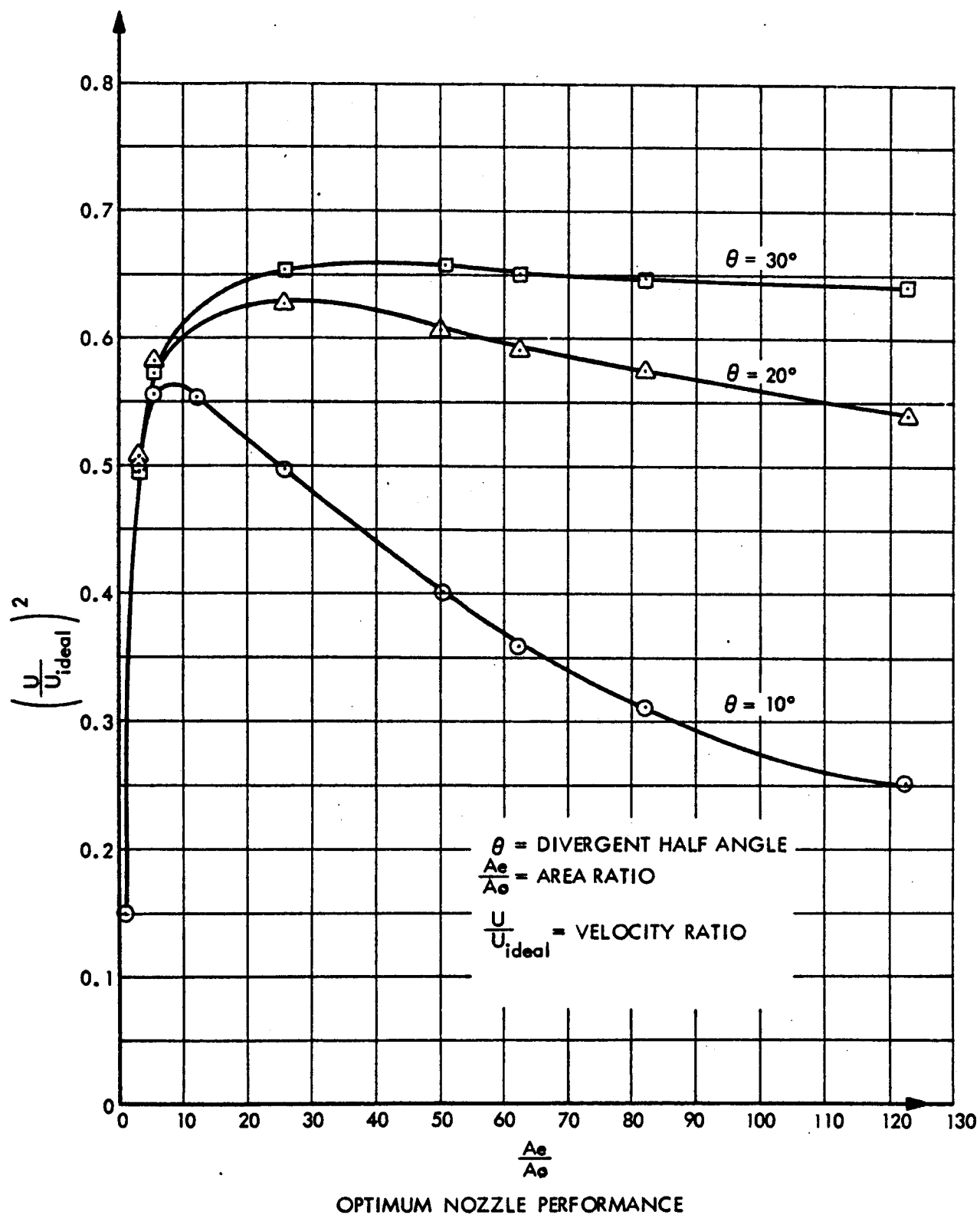


Figure 2.20 Calculated Nozzle Efficiency vs Area Ratio and Divergence Half-Angle (Simplified Analysis)

Subscripts

- c = Chamber; denotes the stagnation condition of the gas before entering the throat
 th = Throat
 e = Exit
 t = Tank
 r = With respect to the radius

Definitions

$$\psi = \frac{\rho}{\rho_c}$$

$$\zeta = \frac{\dot{m}}{\pi r_{th}^2 \rho_c \sqrt{2 C_p T_c}}$$

$$\xi = \frac{\mu \dot{m} \sqrt{\zeta}}{r_{th}^3 \rho_c^2 \zeta^2 u_{ideal}^2}$$

2.4.1 Laminar Friction in a Nozzle

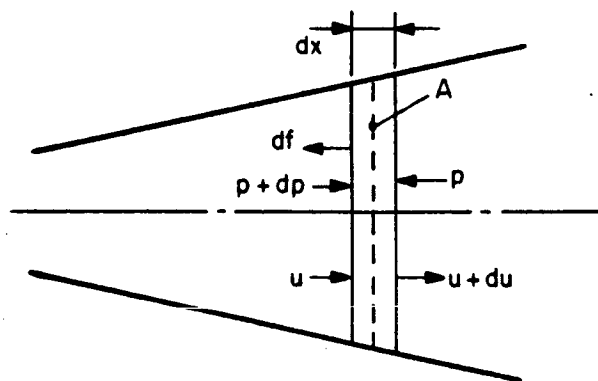


Figure 2.21 Description of Forces in a Divergent Nozzle

The forces acting on a fluid particle are the inertia forces, the pressure forces, and the friction forces. Therefore,

$$d p A - \rho A d x \frac{d u}{d t} - d f = 0 \quad (27)$$

after division by ρA and considering that $u = \frac{d x}{d t}$ equation (27) becomes

$$\frac{d p}{d x} - u \frac{d u}{d x} - \frac{d f}{\rho A} = 0 \quad (28)$$

and since $\frac{1}{\rho} = v$

$$v d p - u d u - \frac{d f}{\rho A} = 0 \quad (29)$$

or

$$d i - u d u - \frac{d f}{\rho A} = 0 \quad (30)$$

Integration of equation (30) gives

$$\frac{u^2}{2} = \frac{u_0^2}{2} + i_0 - i_e - \int \frac{d f}{\rho A} \quad (31)$$

Referring to the chamber condition, equation (31) becomes

$$\frac{u^2}{2} = i_c - i_e - \int \frac{d f}{\rho A} \quad (32)$$

The friction force may be expressed as

$$d f = A \lambda_r \frac{d s}{r} \frac{\rho}{2} u^2 \quad (33)$$

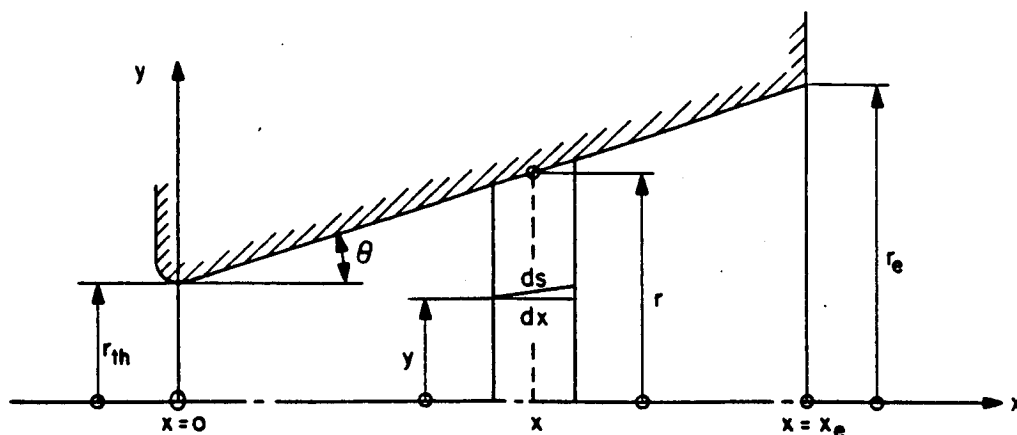


Figure 2.22 Description of Nozzle in the Cylindrical Coordinate System

Simplifying equation (33) by setting $dx \approx ds$ gives

$$\frac{df}{\rho A} = \lambda_r \frac{dx}{r} \frac{u^2}{2} \quad (34)$$

Using the friction term from the Hagen-Poiseuille equation for laminar flow through a pipe

$$\lambda_r = \frac{16}{Re_r} \quad \text{where} \quad Re_r = \frac{ur}{\nu}$$

equation (34) may be written as

$$\frac{df}{\rho A} = \frac{8 \mu u}{\rho r^2} dx \quad (35)$$

With the mass flow $\dot{m} = \pi r^2 \rho u$ equation (35) becomes

$$\frac{df}{\rho A} = \frac{8 \mu \dot{m}}{\pi r^4 \rho^2} dx \quad (36)$$

thus,

$$\frac{u^2}{2} = (i_c - i_e) - \frac{8}{\pi} \mu \dot{m} \int_0^L \frac{dx}{r_x^4 \rho_x^2} \quad (37)$$

where

$$\frac{8}{\pi} \mu \dot{m} \int_0^L \frac{dx}{r^4 \rho} = \frac{8 \mu \dot{m}}{\pi r_{th}^4 \rho_c^2} \int_0^L \frac{dx}{\left(\frac{r}{r_{th}}\right)^4 \left(\frac{\rho}{\rho_c}\right)^2}$$

The integral in the equation above represents the friction term, and F denotes the friction function

$$\int_0^L F(x) dx = \int_0^L \frac{dx}{\left(\frac{r}{r_{th}}\right)^4 \left(\frac{\rho}{\rho_c}\right)^2} \quad (38)$$

There is

$$\frac{r}{r_{th}} = \frac{1}{r_{th}} \sqrt{\frac{A}{\pi}} \quad (\text{circular cross section})$$

From the mass flow balance it follows that

$$A = \frac{\dot{m}}{\left(\frac{\rho}{\rho_c}\right) u_{\rho c}}$$

The velocity at the temperature T is calculated by

$$u = \sqrt{2 C_p (T_c - T)}$$

Hence,

$$A = \frac{\dot{m}}{\rho_c \left(\frac{\rho}{\rho_c}\right) \sqrt{2 C_p T_c \left[1 - \frac{T}{T_c}\right]}}$$

With the substitution

$$\psi = \frac{\rho}{\rho_c} = \left(\frac{T}{T_c}\right)^{\frac{1}{\gamma - 1}}$$

$$A = \frac{\dot{m}}{\rho_c \psi \sqrt{2 C_p T_c [1 - (\psi)^{\gamma-1}]}}$$

$$\frac{r}{r_{th}} = \sqrt{\frac{\dot{m}}{\pi r_{th}^2 \rho_c \psi \sqrt{2 C_p T_c [1 - (\psi)^{\gamma-1}]}}}$$

combining all constants in

$$\zeta = \frac{\dot{m}}{\pi r_{th}^2 \rho_c \sqrt{2 C_p T_c}}$$

the radius ratio becomes

$$\frac{r}{r_{th}} = \frac{\sqrt{\zeta}}{\sqrt{\psi \sqrt{1 - (\psi)^{\gamma-1}}}} \quad (39)$$

The contour of the nozzle is expressed by

$$r = (\tan \theta) x + r_{th} \quad (40)$$

After dividing equation (40) by r_{th} and substituting for $\frac{r}{r_{th}}$ from equation (39) we obtain

$$x \frac{\tan \theta}{r_{th}} + 1 = \frac{\sqrt{\zeta}}{\sqrt{\psi \sqrt{1 - (\psi)^{\gamma-1}}}}$$

and

$$dx = \frac{r_{th} \sqrt{\zeta}}{\tan \theta} \left\{ \frac{\gamma-1}{4} (\psi)^{\frac{2\gamma-5}{2}} [1 - (\psi)^{\gamma-1}]^{-\frac{5}{4}} - \frac{1}{2} (\psi)^{-\frac{3}{2}} [1 - (\psi)^{\gamma-1}]^{-\frac{1}{4}} \right\} d\psi$$

After a transformation of variables the friction term (38) takes the following form:

$$\int_0^L F(x) dx = \frac{r_{th} \sqrt{\zeta}}{\tan \theta} \int_{\psi_{th}}^{\psi_e} \frac{\frac{\gamma-1}{4}(\psi) \frac{2\gamma-5}{2} [1-(\psi)^{\gamma-1}]^{\frac{-5}{4}} - \frac{1}{2}(\psi)^{\frac{-3}{2}} [1-(\psi)^{\gamma-1}]^{\frac{-1}{4}}}{\frac{\zeta^2}{\psi^2 [1-(\psi)^{\gamma-1}]} \psi^2} d\psi$$

The above equation, simplified algebraically, becomes

$$\int_0^L F(x) dx = \frac{r_{th} \sqrt{\zeta}}{4 \zeta^2 \tan \theta} \int_{\psi_{th}}^{\psi_e} \left[(\gamma-1) \frac{\psi^{\frac{2\gamma-5}{2}}}{1-\psi^{\gamma-1}} - 2 \psi^{\frac{3}{2}} \right] (1-\psi^{\gamma-1})^{\frac{3}{4}} d\psi$$

Equation (37) may be written as

$$\frac{u^2}{2} = i_c - i_e - \frac{2 \mu \dot{m} \sqrt{\zeta}}{\pi r_{th}^3 \rho_c^2 \zeta^2 \tan \theta} \int_{\psi_{th}}^{\psi_e} \left[(\gamma-1) \frac{\psi^{\frac{2\gamma-5}{2}}}{1-\psi^{\gamma-1}} - 2 \psi^{\frac{3}{2}} \right] [1-(\psi)^{\gamma-1}]^{\frac{3}{4}} d\psi \quad (41)$$

$$\xi = \frac{\mu \dot{m} \sqrt{\zeta}}{r_{th}^3 \rho_c^2 \zeta^2 u_{ideal}^2} \quad (42)$$

$$F(\psi) = \left[(\gamma-1) \frac{\psi^{\frac{2\gamma-5}{2}}}{1-\psi^{\gamma-1}} - 2 \psi^{\frac{3}{2}} \right] [1-(\psi)^{\gamma-1}]^{\frac{3}{4}} \quad (43)$$

Expressing all constants by ξ (equation 42) and the friction function by $F(\Psi)$ (equation 38), equation (41) written in dimensionless form then becomes

$$\left(\frac{u}{u_{\text{ideal}}} \right)_{\text{friction}}^2 = \frac{C_p T_c \left(1 - \frac{T_c}{T_c} \right)}{C_p T_c \left(1 - \frac{T_{\text{tank}}}{T_c} \right)} - \frac{2}{\pi} \frac{\xi}{\tan \theta} \int_{\Psi_{\text{th}}}^{\Psi} F(\Psi) d\Psi \quad (44)$$

In the testing of the arc-jets the flow is expanded through the nozzle into a test tank maintained at low pressure in order to partly simulate space conditions. The ideal nozzle is defined as the nozzle which expands the propellant from the arc chamber pressure P_c to the tank pressure P_{tank} without losses. Introducing the density ratio Ψ , equation (44) may then be written as

$$\left(\frac{u}{u_{\text{ideal}}} \right)_{\text{friction}}^2 = \frac{1 - \Psi_e^{\gamma-1}}{1 - \Psi_{\text{tank}}^{\gamma-1}} - \frac{2}{\pi} \frac{\xi}{\tan \theta} \int_{\Psi_{\text{th}}}^{\Psi_e} F(\Psi) d\Psi \quad (45a)$$

In most of the tests, P_{tank} is smaller than 0.4 mm Hg, thus, $\Psi_{\text{tank}} \ll 1$ and equation (45) reduces to

$$\left(\frac{u}{u_{\text{ideal}}} \right)_{\text{friction}}^2 = \left(1 - \Psi_e^{\gamma-1} \right) - \frac{2}{\pi} \frac{\xi}{\tan \theta} \int_{\Psi_{\text{th}}}^{\Psi_e} F(\Psi) d\Psi \quad (45b)$$

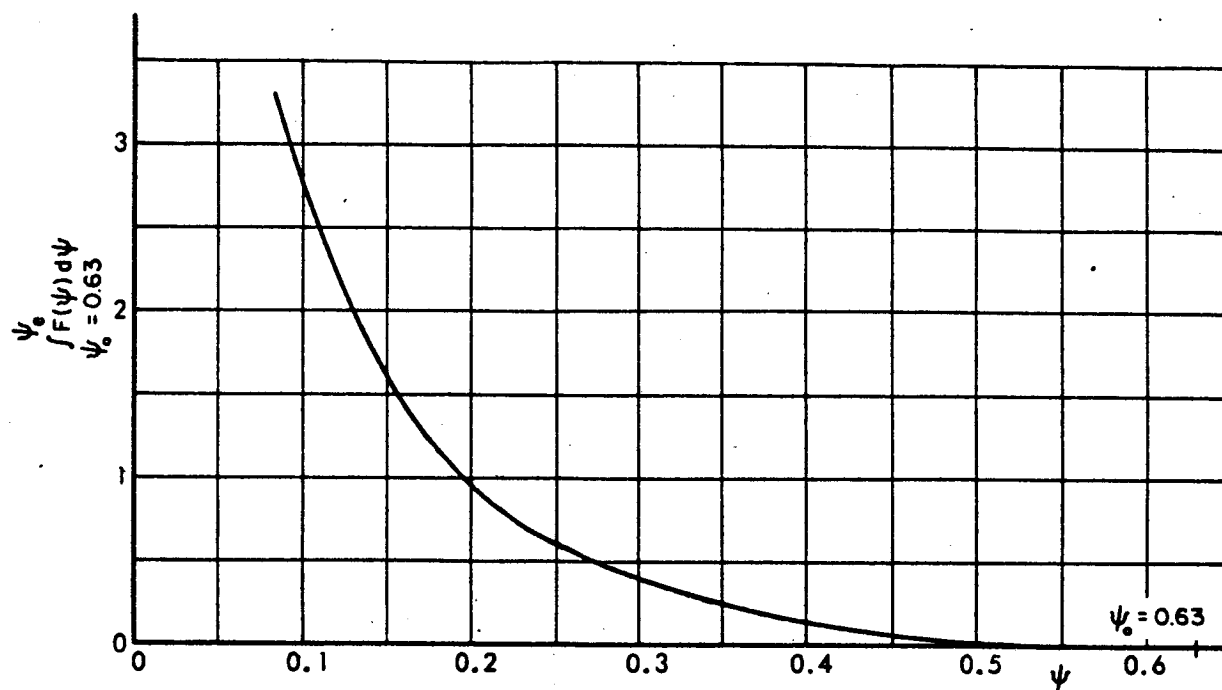
The integral $F(\Psi) d\Psi$ may be solved with any numerical method. In this analysis the Adam's method was applied taking steps of $\Delta \Psi = 0.005$. The integration curve is shown on Figure 2.23. The correlation between x and Ψ is expressed by the equation

$$\frac{x}{r_{\text{th}}} = \frac{1}{\tan \theta} \left[\frac{\sqrt{\xi}}{\sqrt{\Psi \sqrt{1 - \Psi^{\gamma-1}}}} - 1 \right] \quad (46a)$$

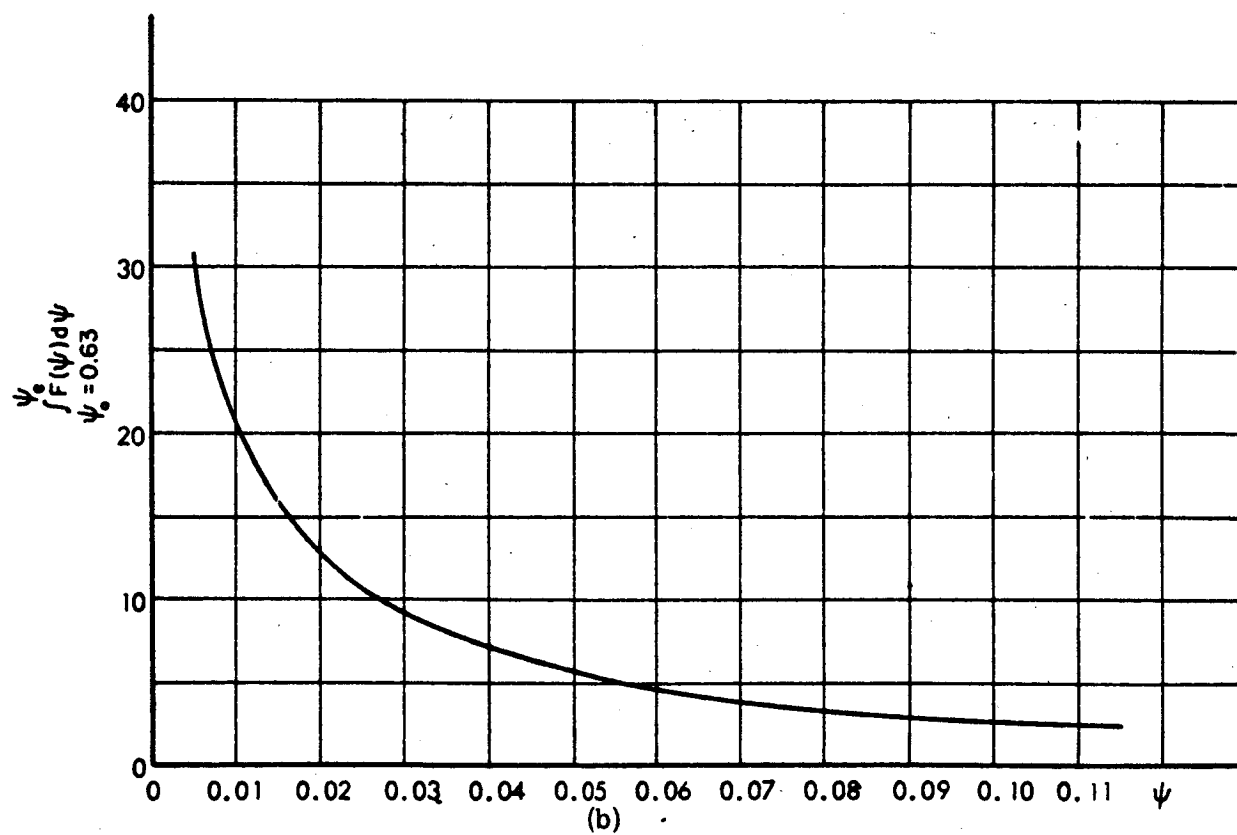
Boundary conditions are:

$$x = 0 \longrightarrow \Psi = \Psi_{\text{th}}$$

$$x = x_e \longrightarrow \Psi = \Psi_e$$



(a)



(b)

Figure 2.23 Plot of Integral of Friction Function

thus,

$$\frac{x_e}{r_{th}} = \frac{1}{\tan \theta} \left[\frac{\sqrt{\xi}}{\sqrt{\psi_e} \sqrt{1 - \psi_e^{\gamma-1}}} - 1 \right] \quad (46b)$$

and the area ratio is

$$\frac{A_e}{A_{th}} = \left(\frac{r_e}{r_{th}} \right)^2 = \frac{\xi}{\psi_e \sqrt{1 - \psi_e^{\gamma-1}}} \quad (47)$$

2.4.2

Effects of Non-Axial Flow

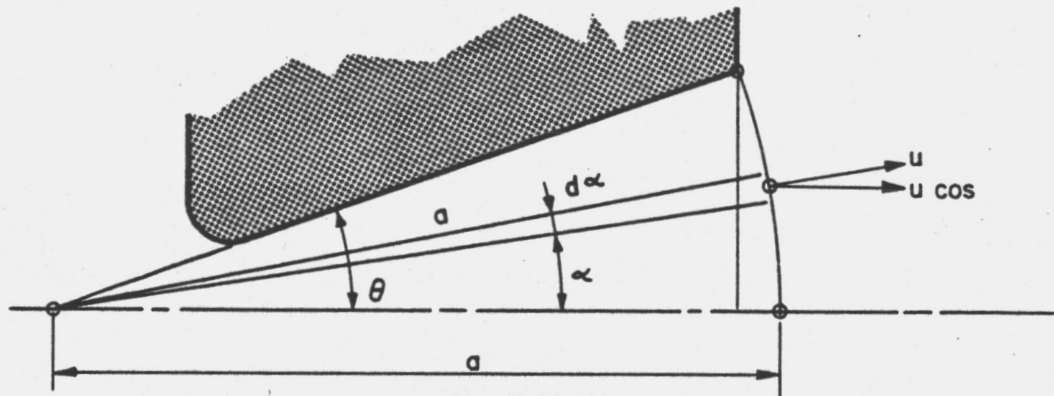


Figure 2.24 Description of Nozzle Coordinate System for Non-Axial Flow

The reduction in thrust caused by the presence of non-axial velocity components in the jet leaving the nozzle can be determined by computing the difference between the axial component of momentum flux and the total momentum flux of the jet.

The axial component of momentum flux through a ring element is

$$dM_{axial} = d\dot{m} u \cos \alpha \quad (48)$$

$$d\dot{m} = 2\pi a^2 \rho u \sin \alpha d\alpha$$

$$M_{\text{axial}} = 2 \pi a^2 u^2 \rho \int_0^\theta \sin \alpha \cos \alpha d \alpha \quad (49)$$

$$M_{\text{axial}} = \frac{\pi}{2} a^2 u^2 \rho (\cos 2 \theta - 1)$$

$$M_{\text{angular}} = 2 \pi a^2 u^2 \rho \int_0^\theta \sin \alpha d \alpha$$

$$M_{\text{angular}} = 2 \pi a^2 u^2 \rho (\cos \theta - 1)$$

$$\frac{M_{\text{axial}}}{M_{\text{angular}}} = \frac{1}{4} \frac{\cos 2 \theta - 1}{\cos \theta - 1} = \frac{1}{4} \frac{(2 \cos^2 \theta - 1) - 1}{\cos \theta - 1} = \frac{1}{2} \frac{(\cos \theta + 1)(\cos \theta - 1)}{\cos \theta - 1}$$

$$\frac{M_{\text{axial}}}{M_{\text{angular}}} = \frac{1}{2} (\cos \theta + 1) \quad (50)$$

Since $M = \dot{m} u$, the momentum flux ratio is also the ratio of the velocities, thus

$$\frac{u_{\text{axial}}}{u_{\text{angular}}} = \frac{1}{2} (\cos \theta + 1) = \epsilon \quad (51)$$

The reduction of the momentum flux as shown in equation (48) is on the pessimistic side because the method proposed is based on a constant velocity profile. In reality, the velocity profile in an arc-jet engine is a bell shaped curve. The velocity near the axis exceeds the velocity near the nozzle wall by a large factor. Therefore, the greater portion of the momentum flux is generated by flow with nearly-axial velocity factors.

Combining friction and non-axial flow effects, the effective velocity may be derived as follows:

$$\frac{u_{\text{eff}}}{u_{\text{ideal}}} = \left(\frac{u}{u_{\text{ideal}}} \right)_{\text{friction}} \times \epsilon \quad (52)$$

The results were shown in Figure 2.20, page 57, for a thruster operating at $I_{\text{sp}} = 1000$ seconds.

The curves show a steep increase in efficiency up to an area ratio of 8. The following are the calculated optimum area ratios as a function of divergence half-angle θ :

TABLE 11

Optimum Nozzle Area Ratio as a Function of Divergence Half Angle

θ	$\frac{A_e}{A_{th}}$	$\left(\frac{u_{eff}}{u_{ideal}}\right)^2$
10°	8	0.564
20°	30	0.630
30°	50	0.658

It appears that the best nozzle efficiency is obtained at $\theta = 30^\circ$ and $A_e/A_{th} = 50$. However, flow separation might become an important factor for $\theta \geq 30^\circ$. Since the 20° and 30° curves are not too much different from each other, a half angle of 20° was chosen. A calculation made prior to this analysis is based on $\theta = 20^\circ$, showed an optimum exit area ratio of 50. Thus, a nozzle half angle of 20° and an exit area ratio of 50 were selected for the tests.

These results are entirely different from the results of a similar analysis made several years ago in which it was concluded that short nozzles with large divergence angles would be optimum for low power thrusters. It is now believed that an error was made in formulating one of the differential equations in the earlier analysis, and that this led to an erroneous conclusion. This belief tends to be substantiated by test results in this program. Early nozzles were designed in accordance with the earlier criteria, while the last few nozzles were designed in accordance with the criteria described above. Performance was found to be substantially improved in the latter case.

One comparison of nozzle performance is shown in Figure 2. 25 for two thrusters of similar configuration except for nozzle design, operating at the same conditions. One nozzle was short, with a small area ratio and an intermediate divergence area ($\theta = 30^\circ$, $A_e/A_o = 12.4$), while the other was designed in accordance with the new analysis and was longer, with a larger area ratio and a smaller divergence angle ($\theta = 20^\circ$, $A_e/A_o = 50$). The thruster with the longer nozzle developed

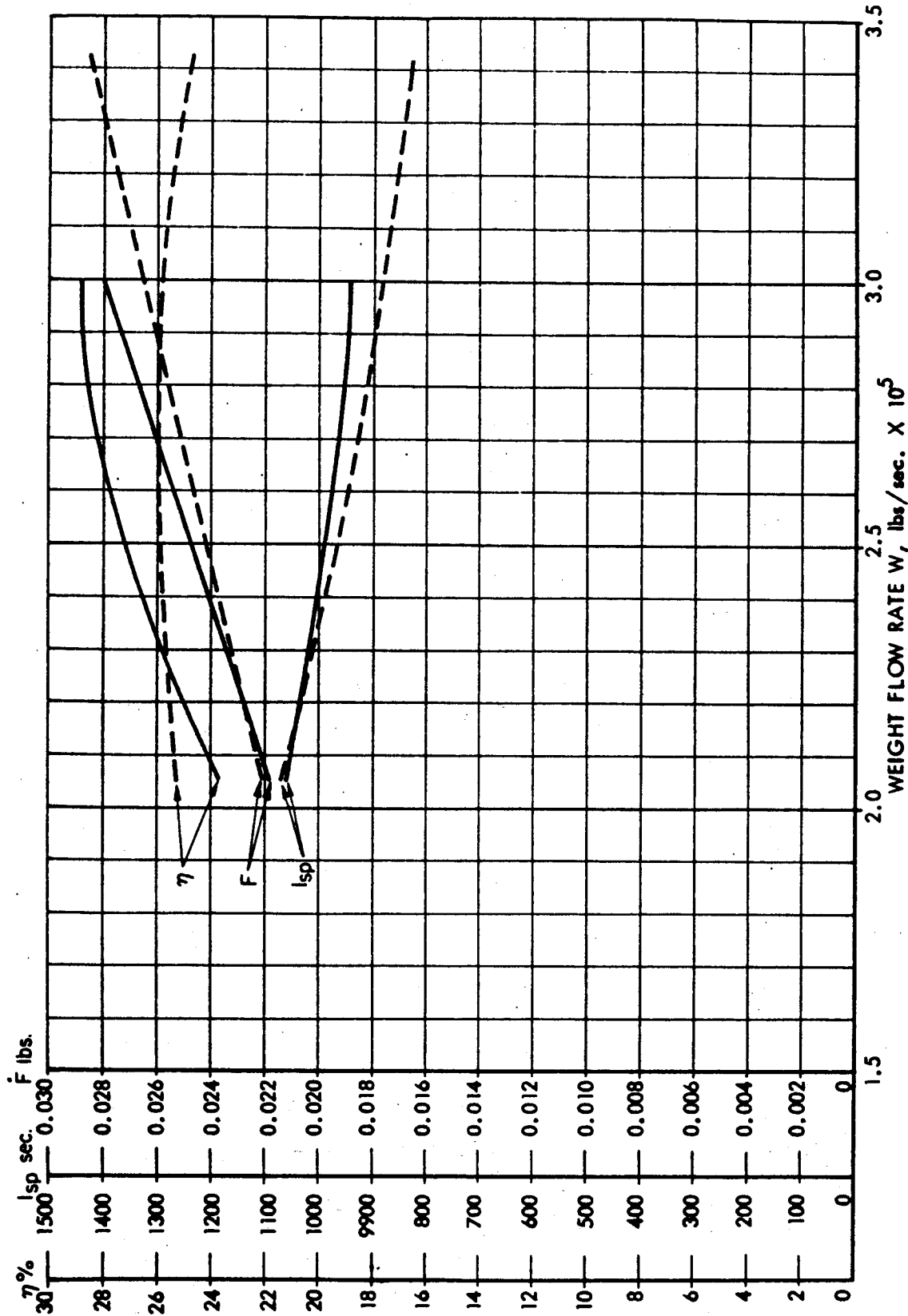


Figure 2.25 Comparison Between a Short and a Long Nozzle With the Same Half Angle $\theta = 20^\circ$
 Solid Curve: Long Nozzle $A_e/A_{th} = 50$ - Test No. 24
 Dotted Curve: Short Nozzle $A_e/A_{th} = 12.4$ - Test No. 14

~~CONFIDENTIAL~~

6% higher thrust, 6% higher specific impulse, and 12% ¹⁾ higher efficiency for the same input power and propellant flow rate. While this does not provide a direct quantitative comparison with the original wide divergence angle nozzle (no direct experimental comparison using similar thrusters was made), it is qualitatively indicative of the better performance of the new longer nozzles compared to all of the earlier short nozzles.

1) Efficiency increased from 26% to 29% at $\dot{m} = 3 \times 10^{-5}$ lbs/sec.

~~CONFIDENTIAL~~

3.0 EXPERIMENTAL RESULTS

The experimental tests can be grouped into three categories: (1) The experimental determination of the optimum nozzle throat diameter; (2) the systematic determination of the optimum cathode-anode axial gap spacing; and (3) a series of changes in design to improve the life of the thruster. These tests culminated in the achievement of a 150 hour continuous run without any indication of failure. The endurance test was terminated only because of contract funds allocated to experimental work.

Table 12 lists all the tests performed under this contract, together with the purpose, pertinent geometrical factors and specific remarks about each test. Results of all tests have been reported individually in some detail in the monthly reports under this contract, and therefore have not been repeated in detail in this final report. Instead, the results of the experimental work have been summarized here, with details presented only for the most significant results.

3.1 Systematic Variation of Throat Diameter

Tests 1 through 12 involved the systematic variation of throat diameter to obtain the optimum throat diameter for operation of a 2 KW thruster. The design variables involved in this test series have been described in Section 2 of this report.

This series of tests was plagued by several time-consuming problems. Two of the major ones were the difficulties encountered in obtaining reliable thrust data and the difficulties encountered in insuring consistent assembly procedures. The difficulties with the thrust balance were caused primarily by the fact that the balance had been designed and developed under a preceeding program for good transient performance, and it was found that both the uncooled balance structure and the transducer circuitry were excessively sensitive to thermal effects arising from prolonged continuous running. Most of these difficulties were caused by thermal distortion of the thrust beam. These problems were finally solved satisfactorily after Test No. 12. A full discussion of the thrust balance problems and their solutions are covered in Section 4 of this report. Thruster assembly procedures were modified after Test No. 12 by having only one person assemble all thrusters, by instituting rigid quality control on parts manufactured, and by providing sufficient instrumentation to assure reproducibility of thruster assembly.

Figure 3.1 summarizes the results of Tests 2 through 7. These tests were run as performance tests in that several data points were taken over a range of mass flow rates at a constant power level of 2.0 ± 0.05 KW. Test No. 2 involved only three data points and this data is not considered reliable. The results of the other tests pointed out inconsistency of manufacture in the variation of performance for identical geometries but different thruster assemblies.

~~CONFIDENTIAL~~

TABLE 12
SUMMARY OF EXPERIMENTAL TESTS ON 2 KW THRUSTOR

Test No.	Test Date	Test Purpose	Gap	Throat Diameter	Remarks
1	3/18	Throat diameter	.006	.015	Failed
2	3/19	Parametric	.008	.020	
3	3/20	Study	.006	.015	
4	3/21		.010	.025	
5	3/22		.012	.030	Failed
6	3/25		.014	.035	
7	3/27		.010	.025	
8	4/1		.012	.030	
9	4/1		.014	.035	
10	4/3		.008	.020	Thrust Beam
11	4/5	Axial gap spacing	.026	.035	Failed
12	4/19	parametric study	.014	.035	
13	5/2		.014	.035	
14	5/8		.020	.035	
15	5/9		.026	.035	
16	5/9		.032	.035	
17	5/13		.032	.035	
18	5/14		.038	.035	
19	5/16	Life	.026	.035	Thrust beam failed
20	5/17	Life	.026	.035	21 1/2 hour run
21	5/24	Life l/d change	.026	.035	75 min. run
22	5/27	Life	.026	.035	65 min. run
23	5/29	Modified gas passages	.026	.035	
24	6/6	New nozzle area ratio	.020	.035	
25	6/11	New nozzle inlet	.014	.035	Thrust beam failed
26	6/24	Life-new inlet	.014	.035	Failed
27	6/26	Life-new area ratio	.026	.035	25 hour run
28	6/28	New nozzle and gas passages	.026	.035	
29	7/2	Life-new nozzle and injector	.026	.035	150 hour run
30	7/11	Demonstration engine	.026	.035	Demonstration and High I_{sp}

~~CONFIDENTIAL~~

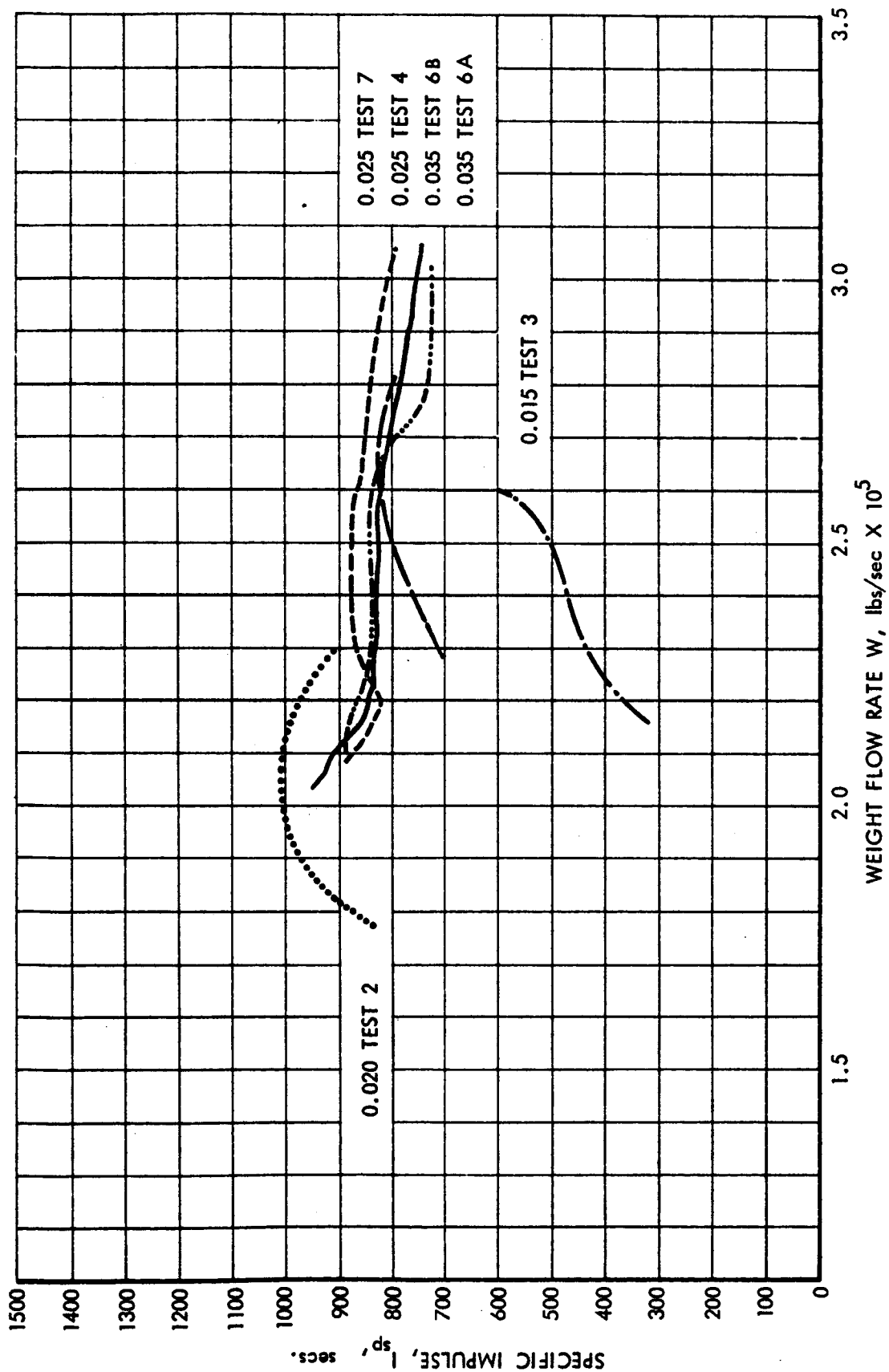


Figure 3.1 Specific Impulse as a Function of Constrictor-Throat Diameter and
Propellant Flow Rate -- Type 142-400 Thrustor

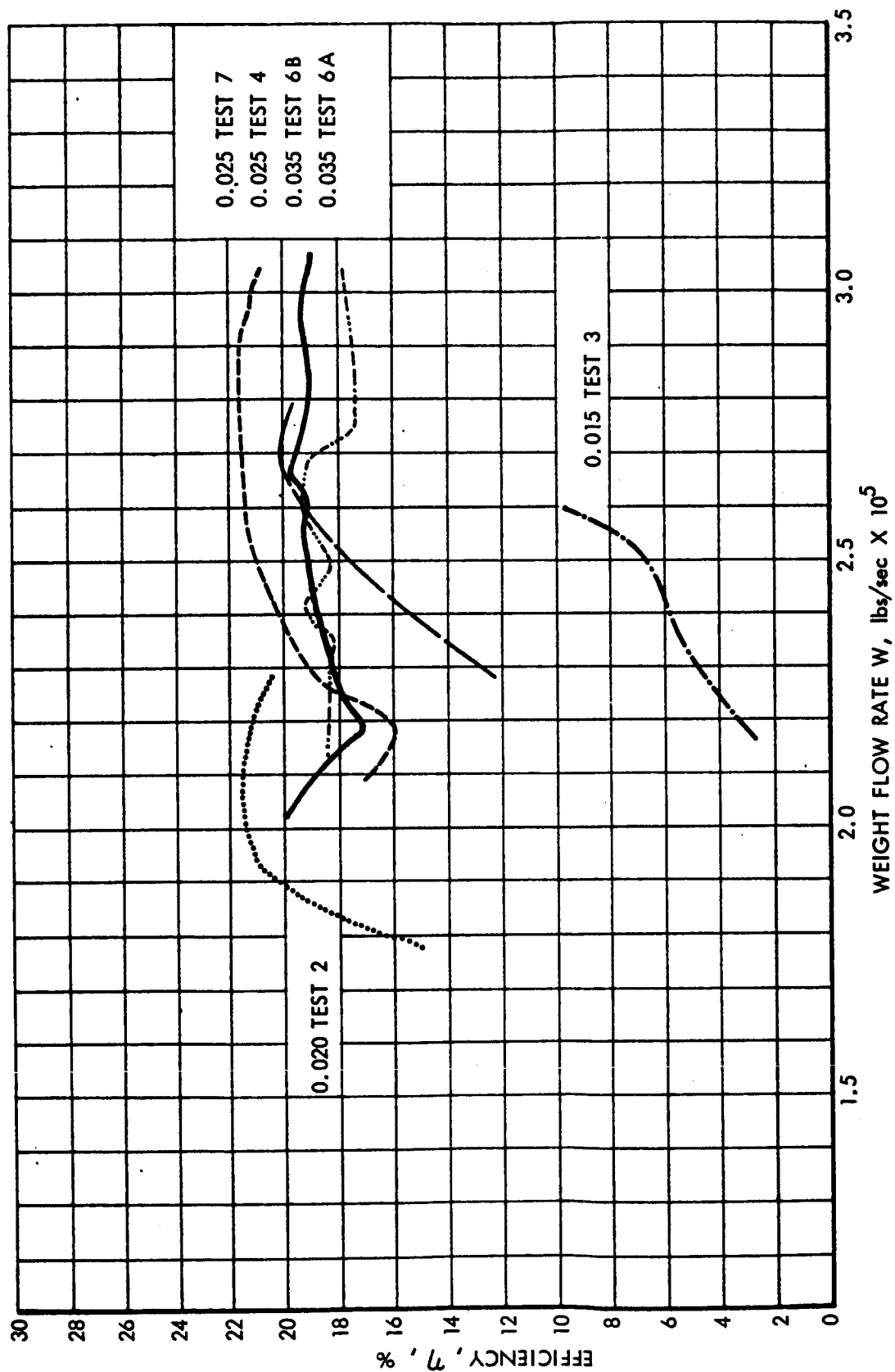
~~CONFIDENTIAL~~

Figure 3.2 Efficiency as a Function of Constrictor-Throat Diameter and Propellant Flow Rate -- Type 142-400 Thrustor

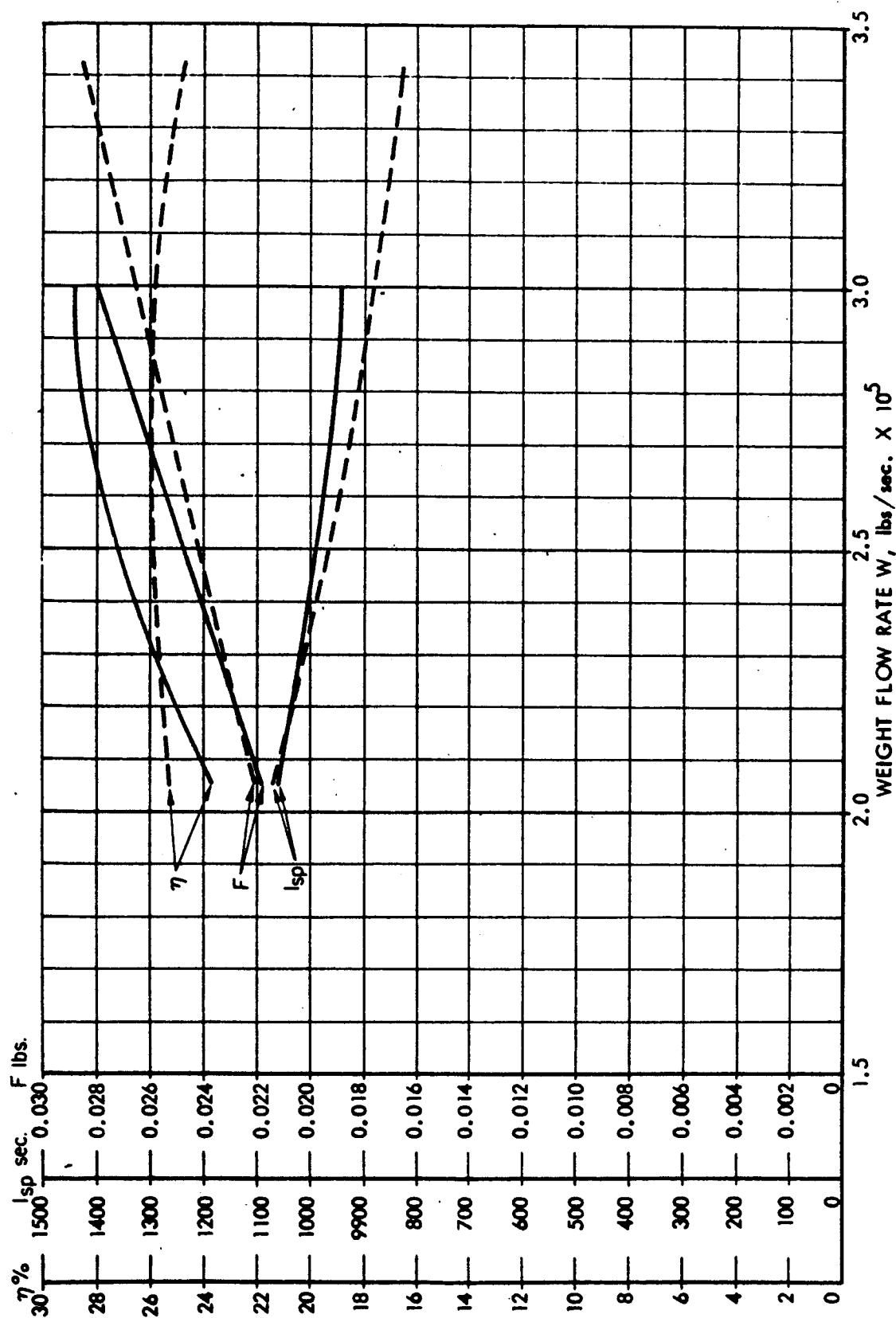


Figure 35 Comparison Between a Short and a Long Nozzle With the Same Half Angle $\theta = 20^\circ$
 Solid Curve: Long Nozzle $A_e/A_{th} = 50$ - Test No. 24
 Dotted Curve: Short Nozzle $A_e/A_{th} = 12.4$ - Test No. 14

recording paper on the thrust readout device. When the test was voluntarily terminated, the operating conditions were:

Mass flow	- 3.01×10^{-5} lbs/sec. H_2
Thrust	- 2.82×10^{-2} lbs
Specific impulse	- 935 sec
Efficiency	- 27.9%

The initial portion of Test 27 was run with a mass flow of about 2.5×10^{-5} lbs/sec. After about 8 hours of operation, some expulsion of molten tungsten was noted and the mass flow was increased to about 3.0×10^{-5} lbs/sec. for the remainder of the test. After the mass flow increase, a slight decrease in specific impulse occurred along with a significant increase in overall efficiency. The full details of Test 27 were reported in the Fifth Monthly Progress Report on this contract.

Figure 3.6 is a photograph showing the cathode after completion of the 25 hour test. The cathode tip was blunted and had a concave or dimpled appearance in the center. The tip had eroded back a distance of 0.012 inch in the 25 hours. Figures 3.7 and 3.8 show the anode-nozzle used in the 25 hour test. Figure 3.7 is a view from the nozzle exit and Figure 3.8 shows the inlet side. Anode erosion was quite severe, and the erosion was not evenly distributed. It is believed that the majority of the anode erosion, especially the non-symmetrical portion, occurred during a short run made of the same thruster after completion of the 25 hour test.

Two important phenomena were noted during Test 27. The anode foot point of the arc was observed to move at fairly regular intervals from one location to another. This was manifested in a flickering of the arc. The second phenomenon was the fairly wide temperature difference between the anode ($1500^\circ C$) and the body ($1000^\circ C$) as read on an optical pyrometer. Observation of this latter phenomenon led to the final design of the anode which lasted for 150 hours.

3.4 150 Hour Endurance Test

The last three tests conducted under this contract were made on the new series 142-600 thruster designs, as described in Section 2. Test 28 was a short test to determine how well the new gas injector port and vortex chamber design would work. Test 29 involved a short performance check at six different mass flow rates. The thruster was then operated continuously for a total of 150 hours. The time averaged operating conditions were as follows:

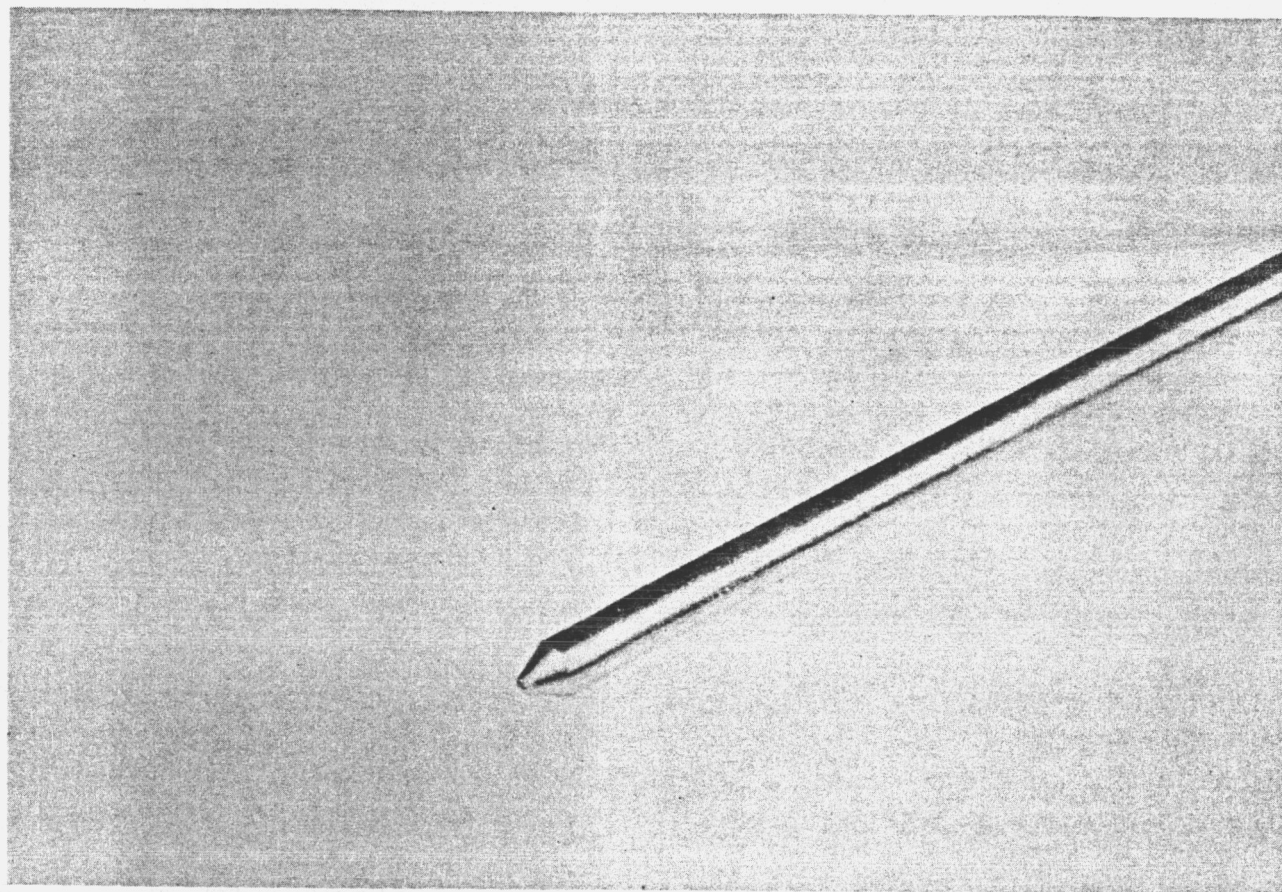


Figure 3.6. Photograph of Cathode After 25-Hour Endurance Test
on Series 142-400 Thrustor (Test No. 27)

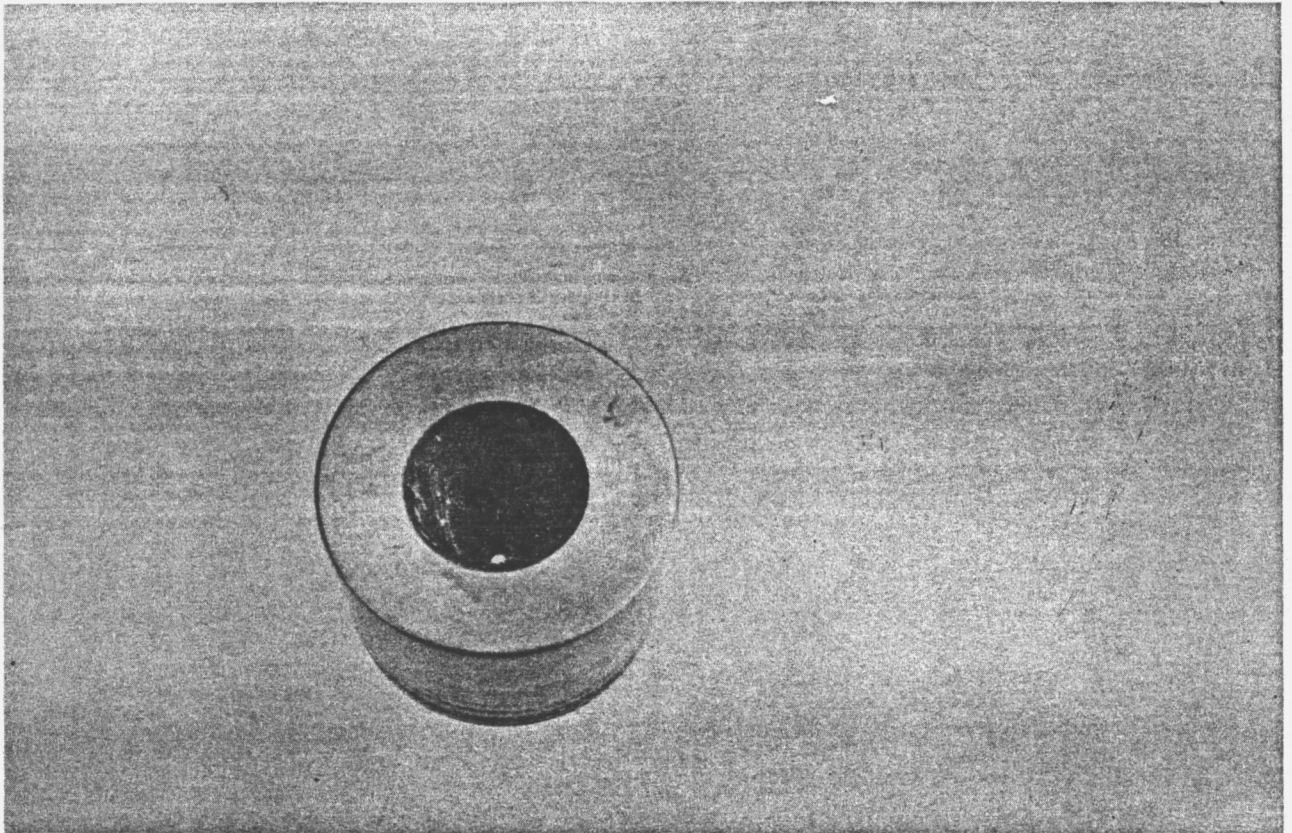
~~CONFIDENTIAL~~

Figure 3.7. Photograph of Anode-Nozzle Insert from Exit End After 25-Hour
Endurance Test on Series 142-400 Thrustor (Test No. 27)

~~CONFIDENTIAL~~

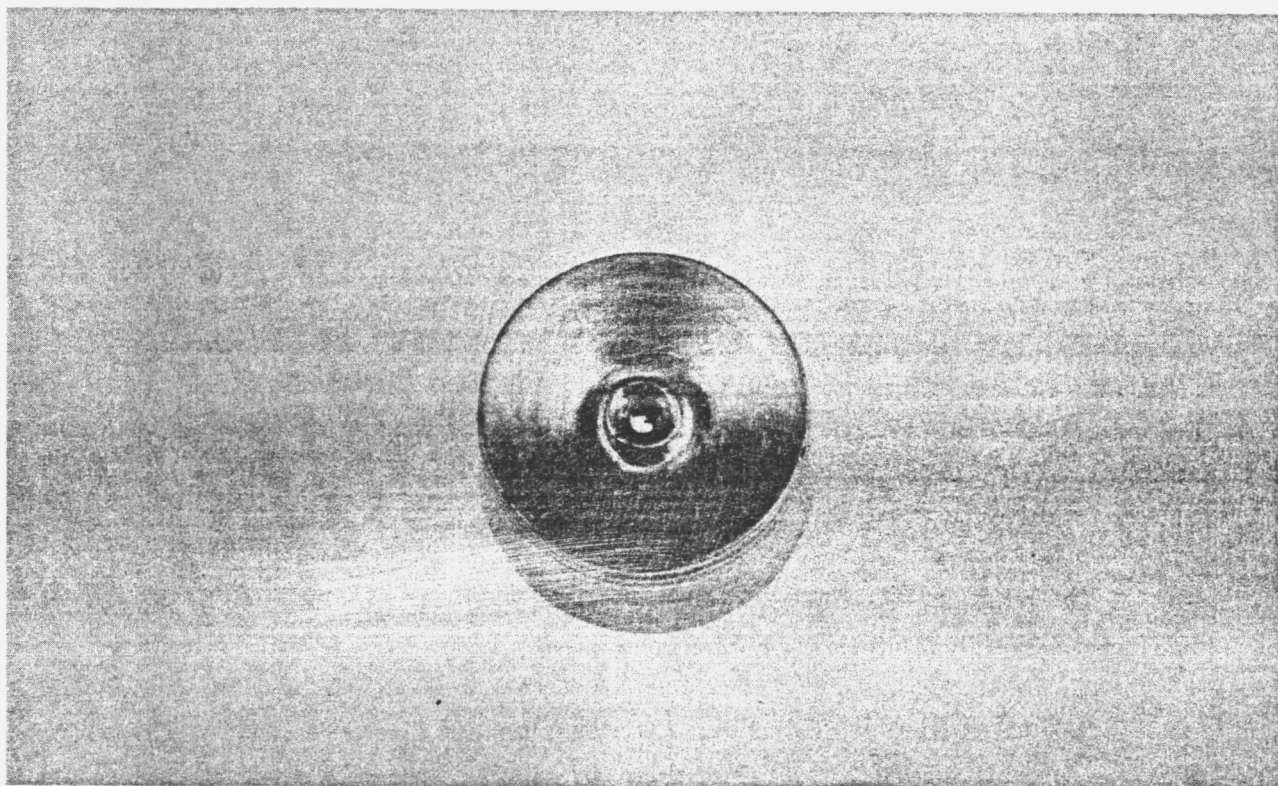


Figure 3.8. Photograph of Anode-Nozzle Insert from Inlet End After 25-Hour Endurance Test on Series 142-400 Thrustor (Test No. 27)

~~CONFIDENTIAL~~

Mass flow rate	= 3.2×10^{-5} lbs/sec.
Thrust	= 3.01×10^{-2} lbs
Specific impulse	= 935 secs
Efficiency	= 30.7%
Power input	= 2.0 KW

Figure 3.9 is a photograph of the thruster operating. This picture was taken after 145 hours of continuous operation. All significant parameters have been plotted as a function of time and are presented in Figures 3.10 through 3.13. It is noteworthy that the performance parameters were approximately equal to the time averaged values at the end of 150 hours of operation. This indicates that the thruster could have performed for a significantly longer period before any failure occurred.

The peak performance was obtained at the 108 hour mark of the test. The values of the parameters at the peak were:

Mass flow rate	= 3.23×10^{-5} lbs/sec. H_2
Thrust	= 3.14×10^{-2} lbs
Specific impulse	= 973 secs
Efficiency	= 33.4%
Power input	= 2.00 KW

Several interesting comparisons of the data presented in Figures 3.10 through 3.13 have been made. Maximum thrust and efficiency were obtained when the voltage was at a maximum and when the anode temperature and housing temperature were at a minimum. Since propellant mass flow was an externally controlled independent variable, this parameter did not enter into these comparisons. Over relatively short intervals of time, it was noted that the thrust, specific impulse and efficiency were at a maximum when the orifice downstream pressure (p_2) was at a minimum. This is particularly evident in the period between hours 62 and 80. The anode temperature and housing temperature remained at a fairly constant ratio throughout the duration of the test.

Since the most stable overall operation and highest thrust, specific impulse, and efficiency were all obtained when the voltage was highest, it appears that the relative location of the anode foot point of the arc along the axis of the thruster has a significant bearing on the performance of the thruster. The observation that maximum specific impulse and efficiency during the 150 hour test coincided with minimum anode-nozzle temperature and maximum arc voltage (using a fixed cathode-anode gap setting) is generally consistent with the previous discussions about the probable effects of gap settings.

~~CONFIDENTIAL~~

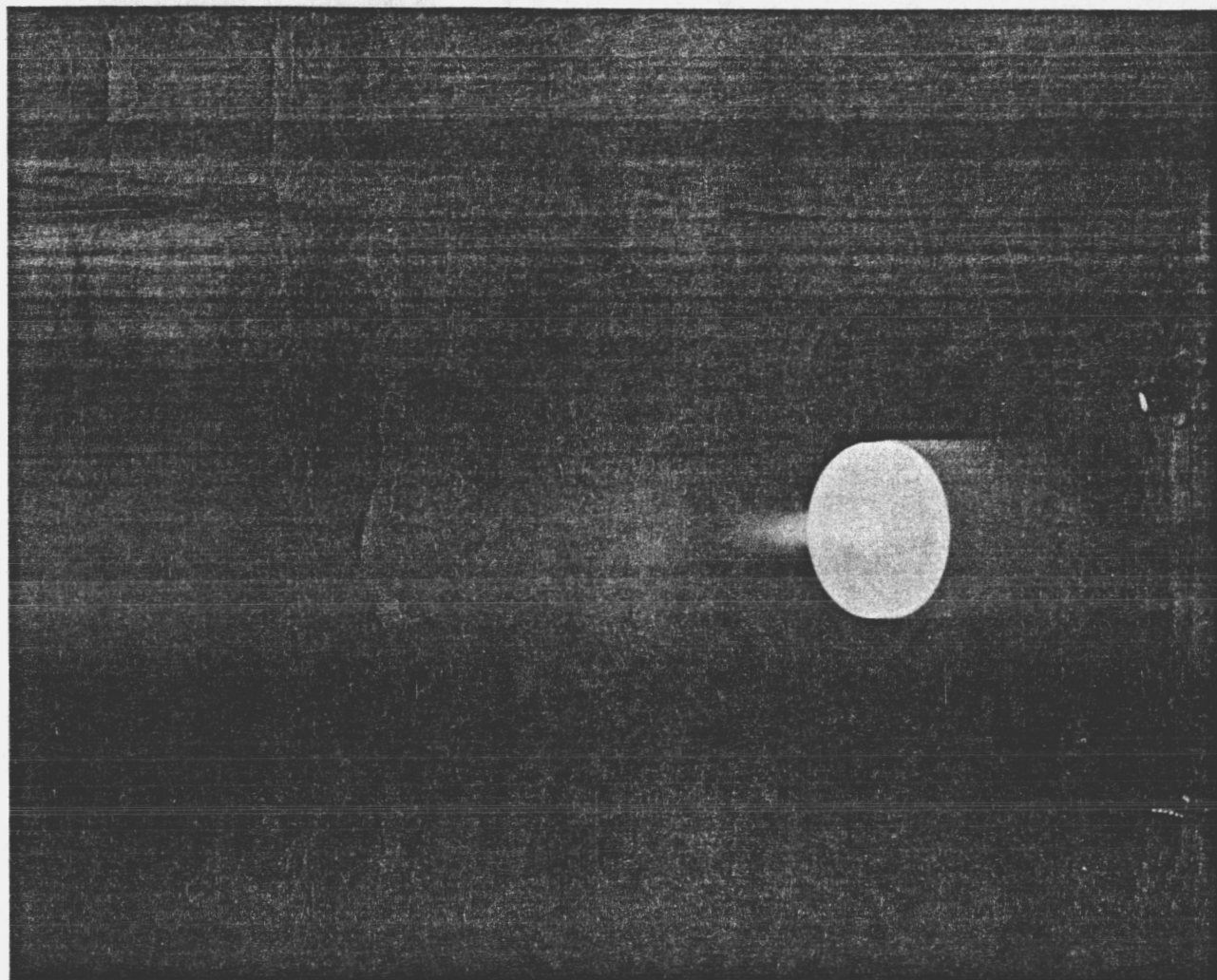
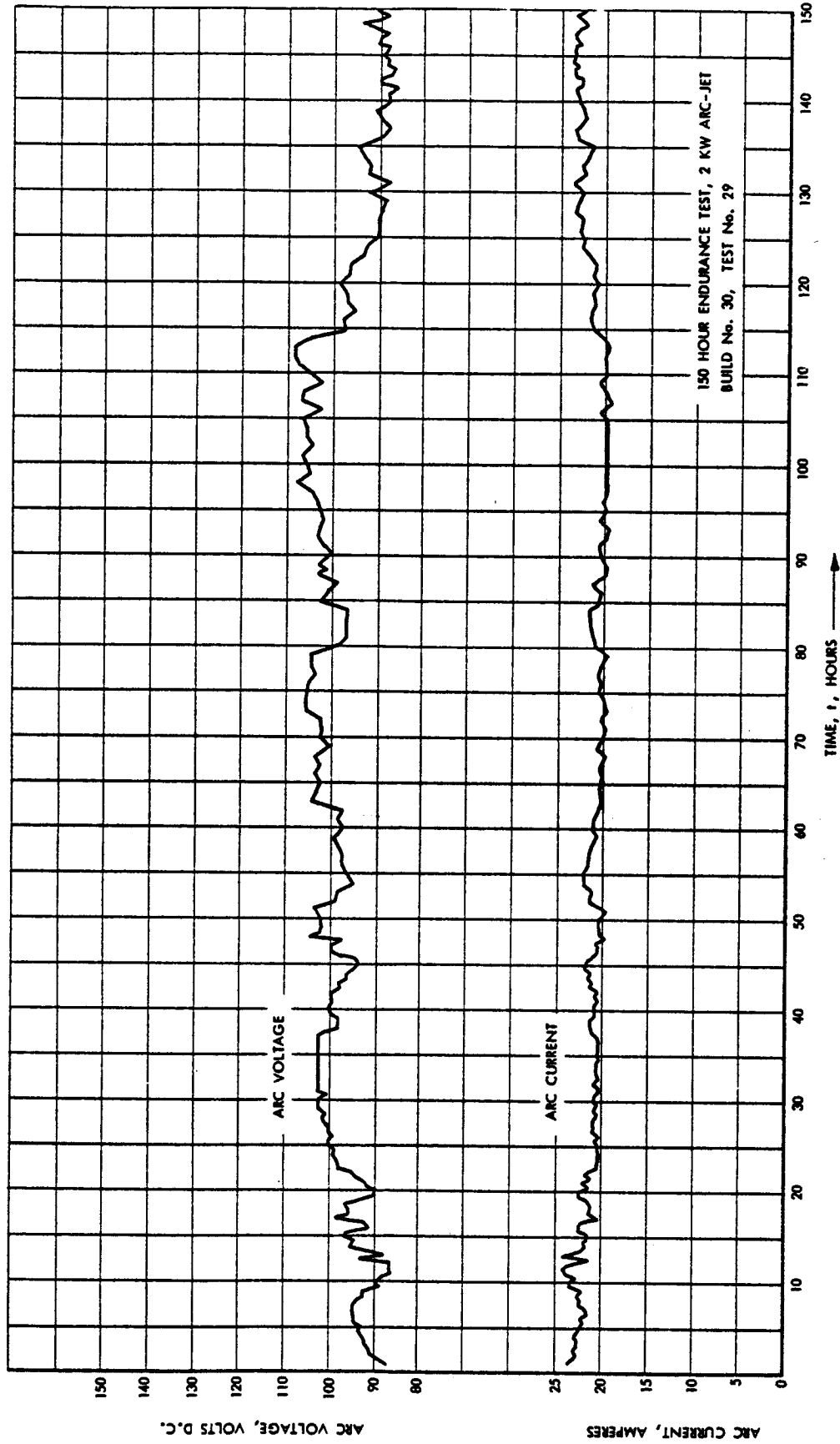


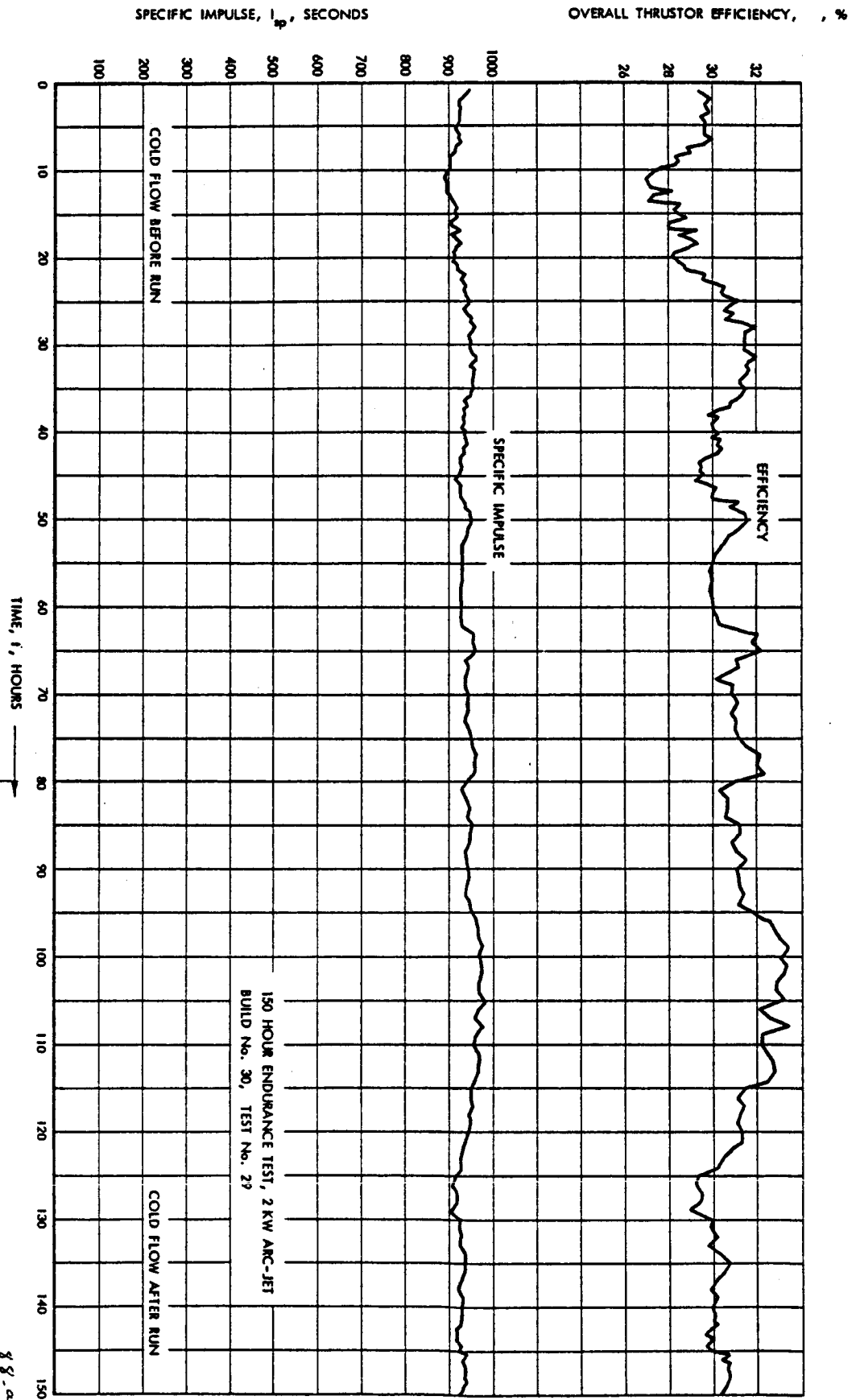
Figure 3.9. Photograph of Series 142-600 Thrustor in Operation After 145 Hours of Continuous Running During Test No. 29 (Test Chamber Pressure \approx 0.08 mmHg abs.)



87

Preceding page blank

Figure 3.10. Plot of Thrustor Inlet Pressure and Propellant Flow Rate vs Time -- 150-Hour Endurance Test



CONFIDENTIAL

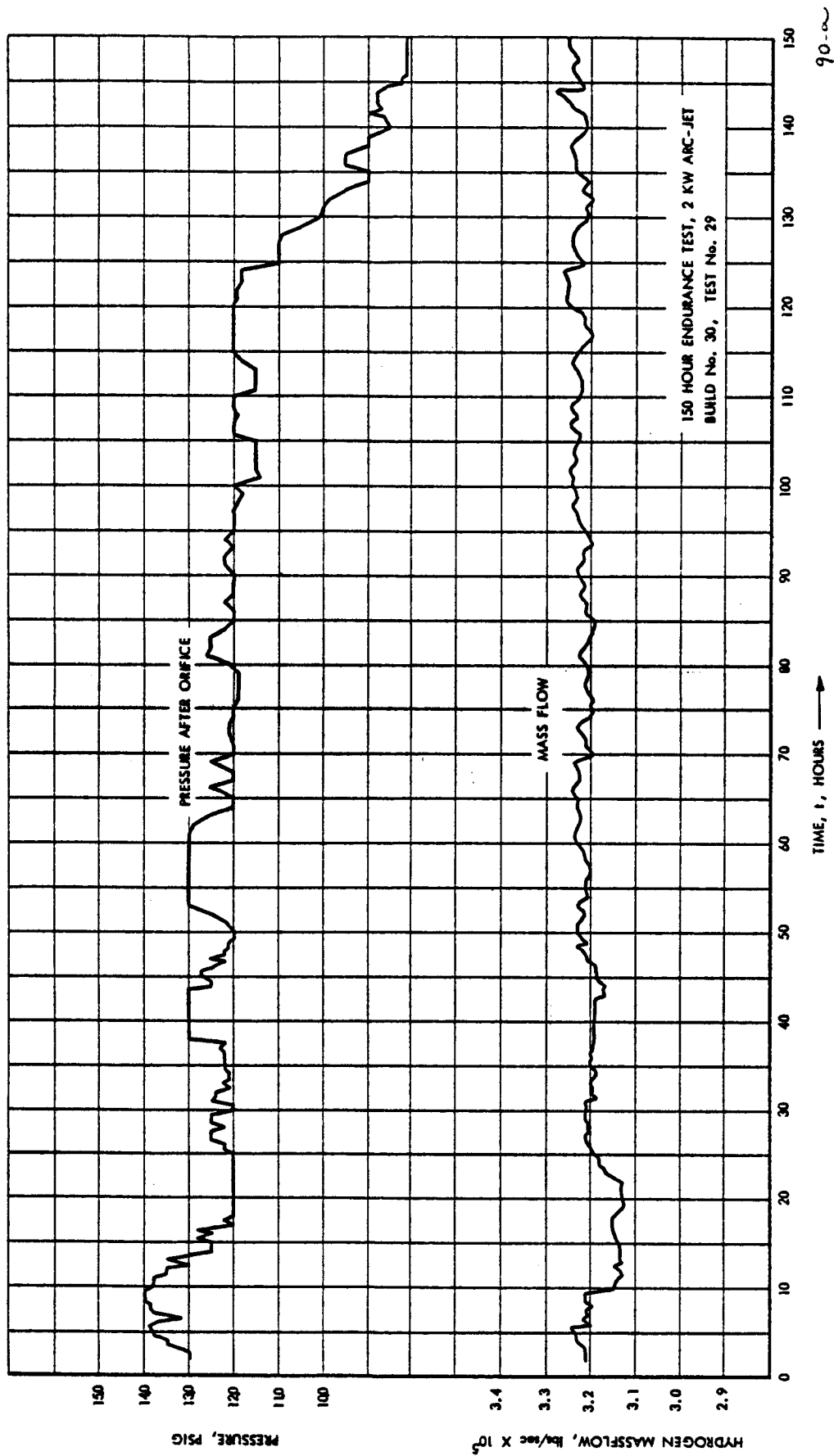


Figure 3.13. Plot of Thrustor Input Voltage and Current vs Time -- 150-Hour Endurance Test

CONFIDENTIAL

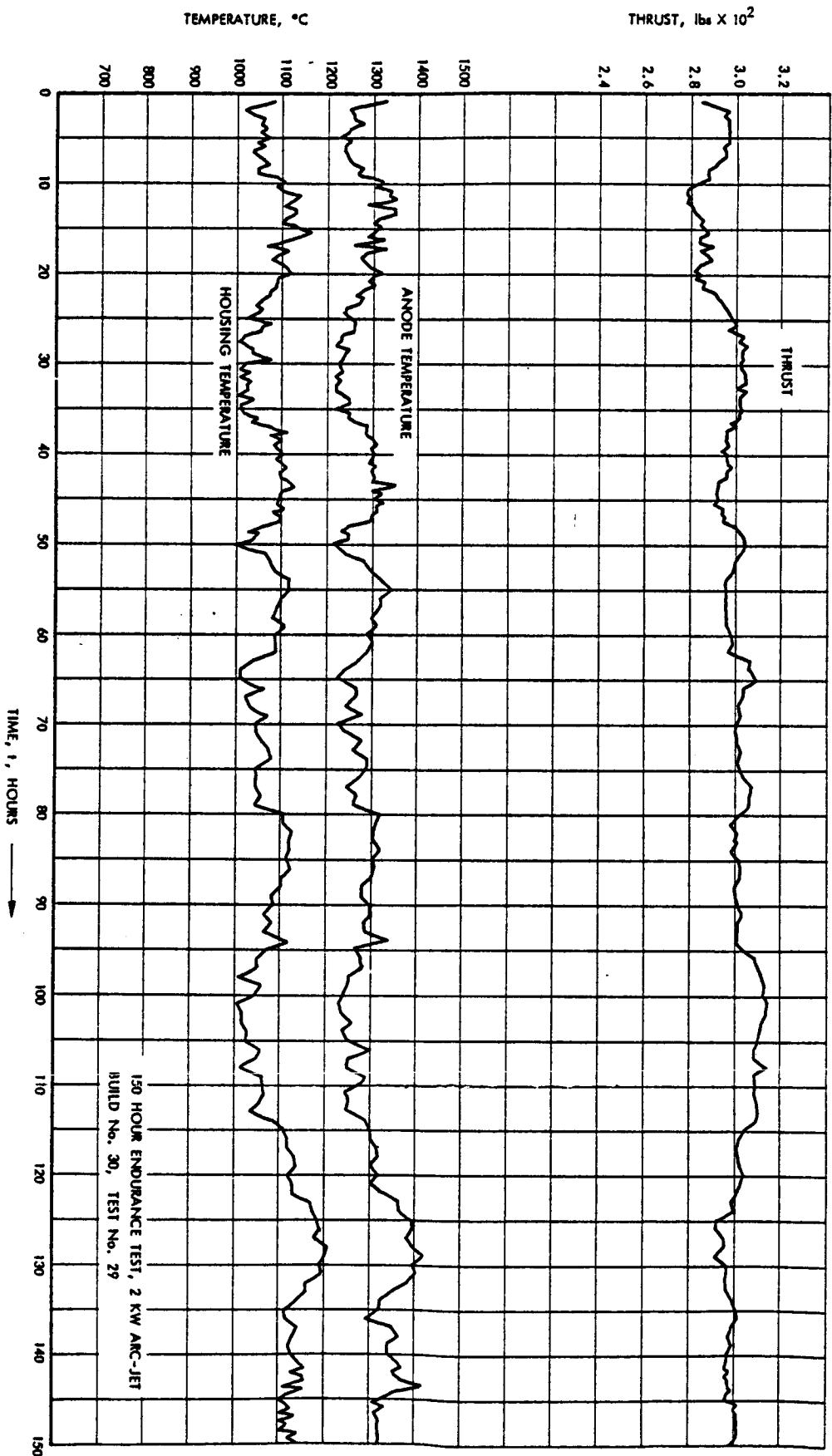


Figure 3.12. Plot of Thrustor Efficiency and Specific Impulse vs Time -- 150-Hour Endurance Test

CONFIDENTIAL

During the high voltage period of operation it is probable that the arc was being stretched out well into the divergent section of the longer nozzle, with the anode attachment region located on the nozzle walls downstream of the throat. Since a moderately large cathode-anode axial gap of 0.026 inch was used, a comparatively long arc with relatively high voltage and low current could and did occur whenever conditions were such as to cause the anode foot point to locate in the divergent section of the nozzle. These arc conditions -- elongated arc column located largely upstream of the throat, high voltage and low current -- were all conducive to transferring a maximum of useable energy to the gas while dissipating a minimum of energy in the anode in the form of heat, thereby producing maximum thrust, specific impulse, and efficiency for fixed values of input power and propellant flow rate. The lower arc current contributed by decreasing the fraction of the total input power dissipated in the anode drop region.

The fact that the higher arc voltage was associated with a longer arc length was further substantiated by visual observation. During periods when the voltage was in excess of 100 volts, the arc foot point appeared to be located in the exit cone of the nozzle, and arc operation appeared to be very stable. At other times the movement of the anode foot point of the arc was erratic, and periodically the anode foot point would relocate inside the throat section or near the exit of the throat section, reducing the arc voltage and increasing the anode temperature. This relocation of the anode foot point of the arc was readily observed visually during operation of the thruster. The short, low voltage arc produced a large amount of radio frequency noise which was monitored on a receiver with an antenna located in the test chamber. It appeared that each successive movement of the anode foot point of the arc from the low voltage position to the high voltage position was accompanied by expulsion of a small quantity of vaporized material, probably from the anode. The lower chamber pressure at the higher voltages would be expected from the above theories on the location of the arc foot point.

After disassembly, the critical parts of this thruster provided a good insight into the operation of the 2 KW arc-jet engine during the endurance test. Figure 3.14 shows the cathode and cathode insulator in their relative positions after disassembly of the thruster. Figure 3.15 shows the same two parts separated. The thoriated tungsten cathode tip was eroded, with a small cavity in the center as is readily apparent from both pictures. The boron nitride cathode insulator was eroded slightly at the hot end, and had a slightly spongy appearance. Probably the lower melting point boron oxide binder used in the boron nitride piece melted and vaporized during the run, leaving a slightly porous boron nitride structure.

Figure 3.16 shows the full assembly of the thruster without the housing. The anode is positioned at the end of the cathode insulator. An enlarged photo of the anode

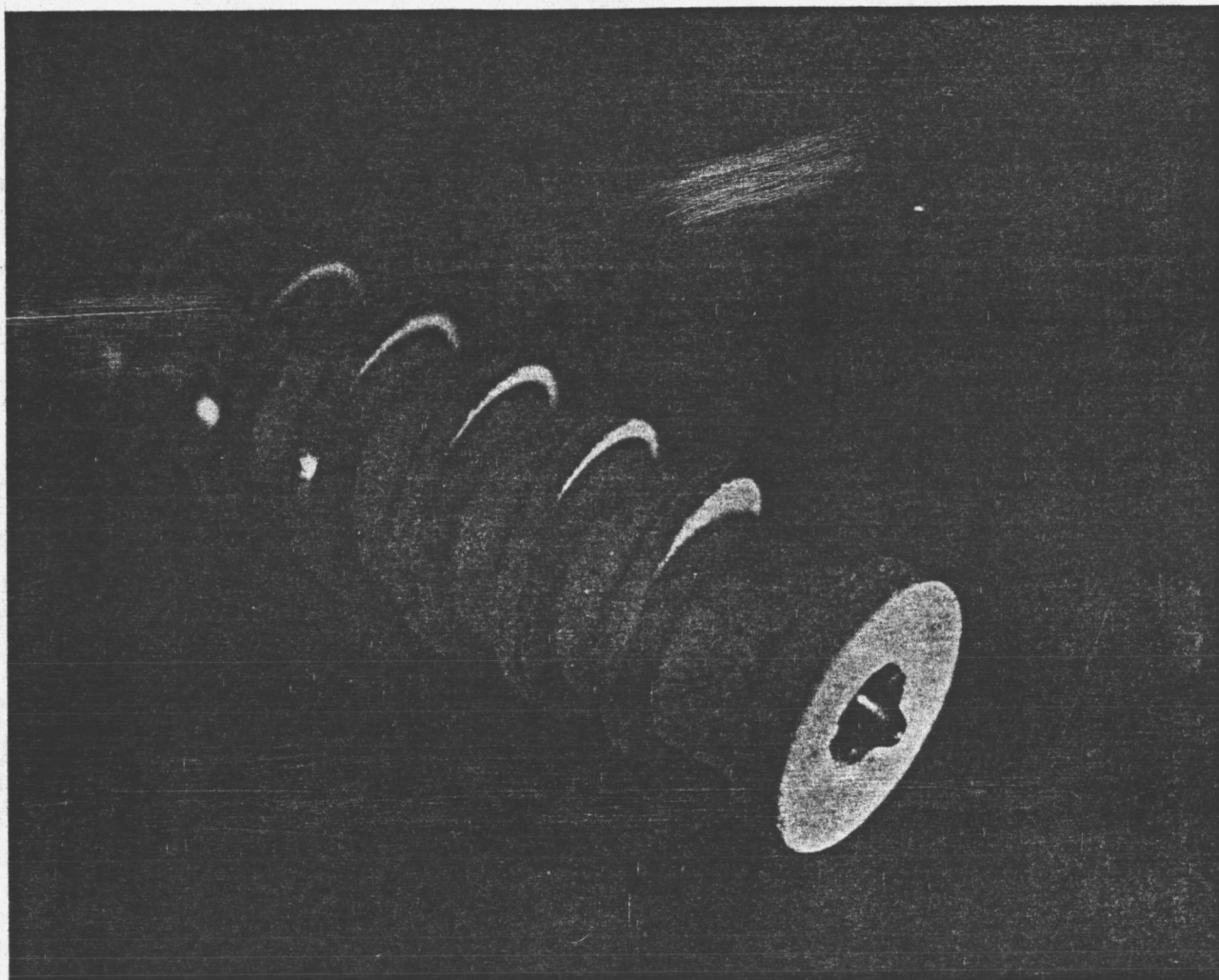


Figure 3.14. Photograph of Cathode Mounted in Cathode Insulator After Disassembly of Series 142-600 Thrustor Following Completion of 150-Hour Endurance Test (Test No. 29)

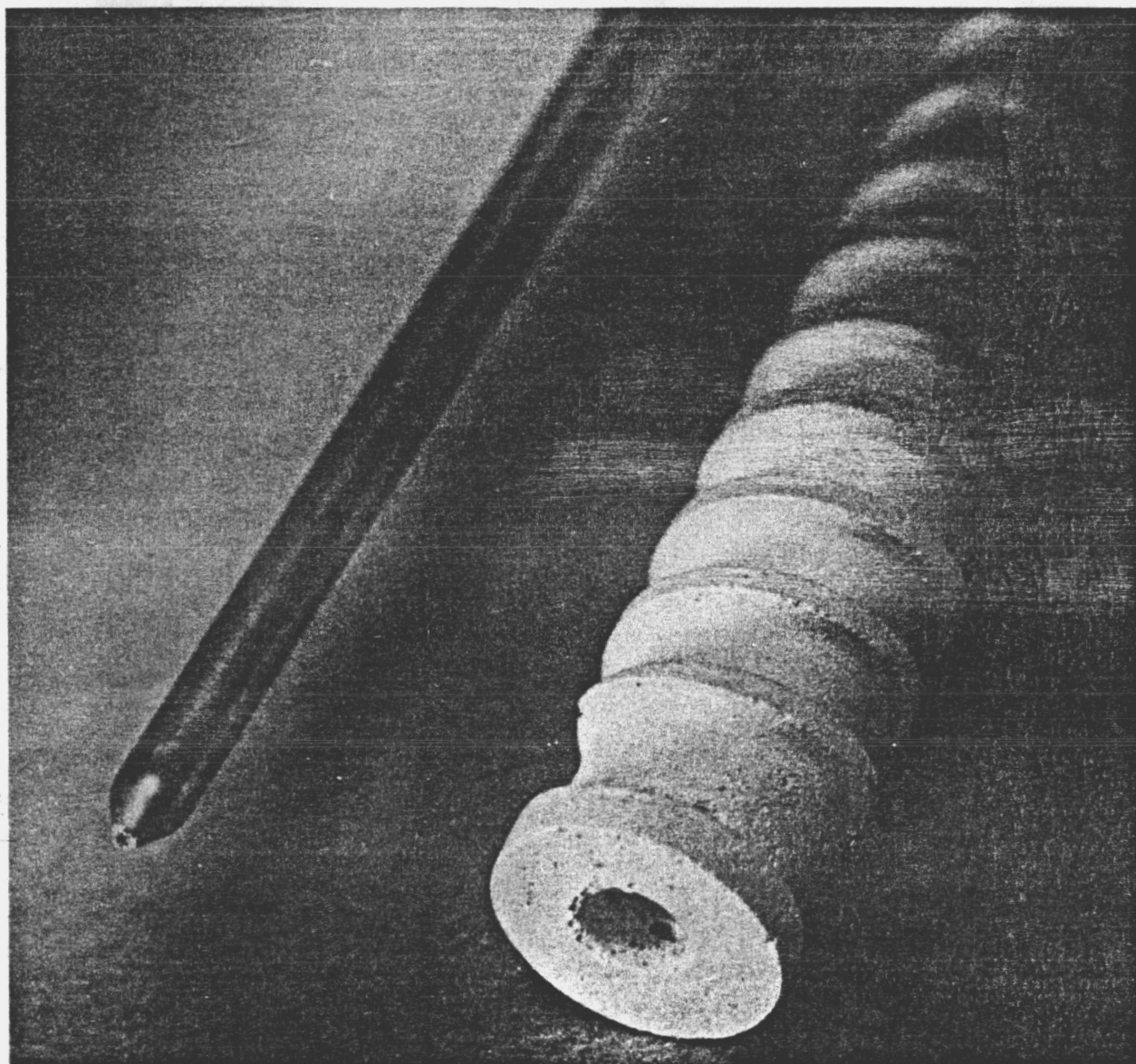


Figure 3.15. Photograph of Cathode and Cathode Insulator After Disassembly of Series 142-600 Thrustor Following Completion of 150-Hour Endurance Test (Test No. 29)

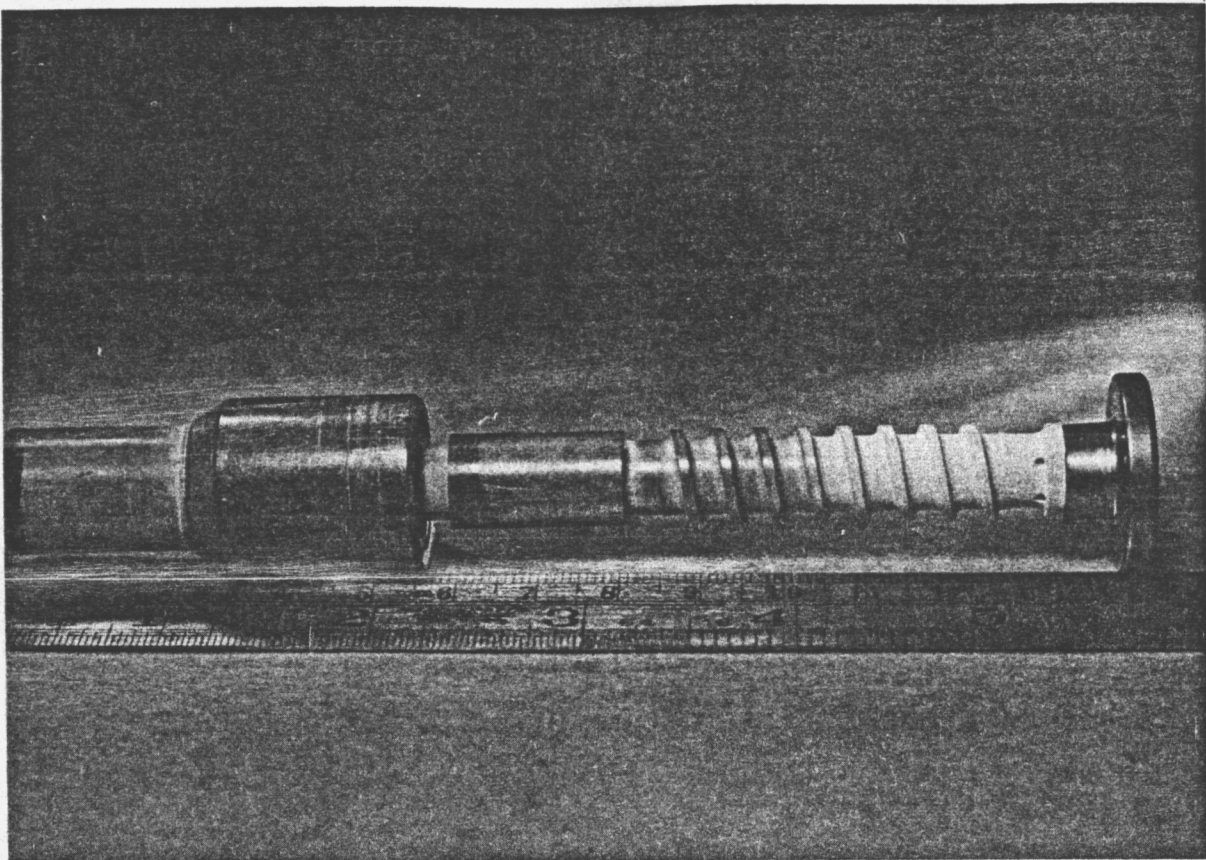
~~CONFIDENTIAL~~

Figure 3.16. Photograph of Internal Parts of Series 142-600 Thrustor Assembled Without Molybdenum Outer Housing After Completion of 150-Hour Endurance Test (Test No. 29)

~~CONFIDENTIAL~~

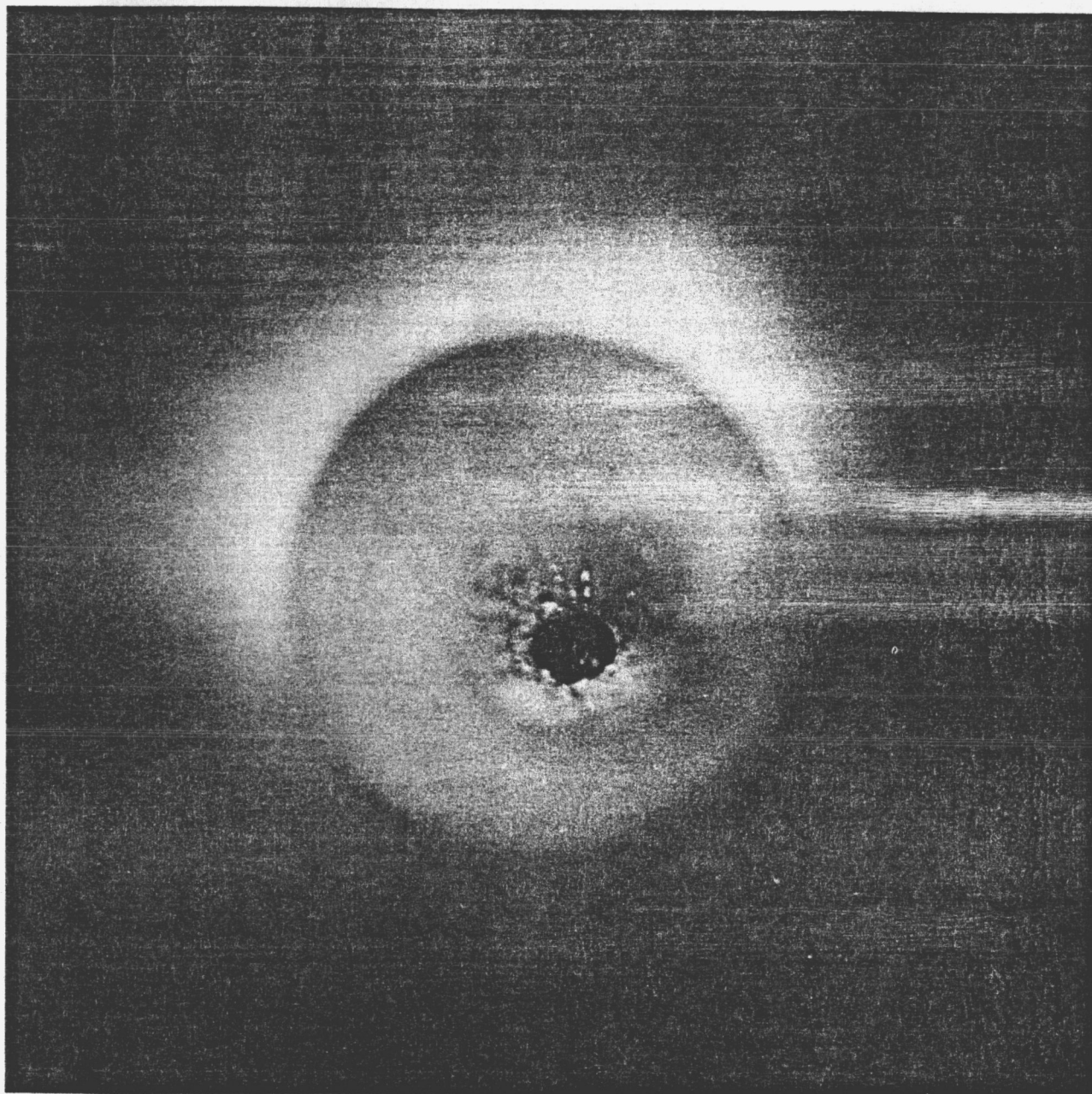


Figure 3.17. Photograph of Nozzle Exit End of Anode-Nozzle Insert After Completion of 150-Hour Endurance Test (Test No. 29)

~~CONFIDENTIAL~~

exhaust section is shown in Figure 3.17. The slightly irregular shape of the throat and the existence of some droplets of material in the exhaust section can be seen on this photograph.

In a careful inspection of the thruster after disassembly, the cathode length was found to be reduced by 0.041 inches, the average throat diameter was found to be 0.0415 inches, and the cathode weight loss was found to be 0.024 grams. The changes in dimensions of both parts were measured by using a 50 power comparator. After disassembly, a slightly higher arc chamber pressure under cold flow testing with helium was found compared to the value measured prior to the test, indicating an increased flow restriction in one of the minimum area passages.

During initial start-up of this thruster for Test No. 29, the power controller was accidentally left on a high setting. A peak power of approximately 4 kilowatts was recorded during the starting transient, and a shower of sparks was emitted by the thruster during this start. It is believed that the shower was tungsten particles eroded from the cathode tip by the excessive current, and that this erosion caused the thruster operation to be modified somewhat.

It seems apparent from this test that the combined use of a modified gas injector design and a large anode radiation area materially increased the life of the thruster. The relative importance of these and various other factors which were incorporated in this design were not individually determined since there was no time remaining in the program for individual variation of these parameters.

Following the completion of Test No. 29, a duplicate thruster was manufactured and assembled at the request of the NASA Technical Monitors in order that they might view the operation of this thruster design during their visit to the Plasmadyne facility. This demonstration test was made as Test No. 30, with slightly different results from those obtained in Test No. 29. The principal difference was in the lower voltage level at which the new thruster operated. This difference in the voltage level is thought to have been caused by the fact that the new thruster was started in Test No. 30 at a power level slightly below 2 KW, without any apparent erosion of the cathode tip. The other performance parameters -- thrust, specific impulse and efficiency -- were approximately equal to those obtained in the first hour of Test No. 29.

The thruster employed for Test No. 30 was run at higher power levels with the same mass flow used in the 150 hour test in order to determine approximately the maximum specific impulse attainable with this particular design. The maximum value obtained and the other parameters are as follows:

~~CONFIDENTIAL~~

Mass flow rate	= 2.56×10^{-5} lbs./sec. hydrogen
Thrust	= 3.26×10^{-2} lbs.
Specific impulse	= 1,270 sec.
Efficiency	= 25.9%
Power input	= 3.5 KW

This high specific impulse performance is thought to be representative of this radiation-cooled thruster design. Specific impulse levels approaching the 1,270 seconds were achieved over a range of power levels and propellant flow rates. Reduction of the mass flow below approximately 2.5×10^{-5} lbs./second resulted in erratic thruster operation and erosion of the anode, probably because the propellant injectors were designed specifically for a H_2 flow of 3.0×10^{-5} lbs./second. It is thought that higher specific impulse levels could be obtained at the lower power levels and lower flow rates if the gas injectors were redesigned for those lower flow rates.

Detailed information on the test parameters measured and results obtained in Tests No. 29 and 30 were included in the Sixth Monthly Progress Report under this contract.

3.5 Tests of Series 142-300 Thruster Design

A brief testing program was performed on a thruster built to the series 142-300 design as described in Section 2 of this report. These tests were run at relatively high mass flows and low power levels in order to start evaluation of the design. Very low specific impulse levels and rather high efficiency levels were noted during these preliminary tests. The tests were stopped at the direction of the NASA Technical Monitors before any conclusive data on this design could be obtained.

3.6 Interpretation of Test Results

The test results obtained in this development program strongly indicate that long life and reasonably high efficiencies can be obtained from properly designed low power (approximately 2 KW) arc-jet thrusters operated at approximately 1000 seconds specific impulse.

The test results also indicate that particular attention must be paid to the design of the anode-nozzle from the heat transfer standpoint in order to avoid any dam effects which tend to cause local overheating and excessive erosion of the anode. In the present 2 KW program it appears that the anodes were not being adequately cooled, because of various heat dam effects, until the series 142-600 design was evolved, with its larger radiating surface. Temperature measurements made on the anode surface and on the thruster housing surface for the various anode designs tend to confirm the presence of

~~CONFIDENTIAL~~

heat dam effects in the earlier designs and their elimination in the last design, and this conclusion is substantiated by the results of the life tests.

The test results further indicate that close attention must also be paid to the design of the propellant injectors in low power thrusters because of the adverse effects of the very low Reynolds numbers in the arc chamber on vortex flow. All of the 2 KW thrusters tested before the series 142-600 design was evolved employed threaded passages as propellant injectors and vortex generators, while the latter design employed injection orifices. It can be concluded from the test results that the various threaded passage configurations provided inadequate control over the velocity and direction of injection of the gas into the arc chamber, while the new injector ports did provide the needed control, with the result that an adequate vortex was apparently maintained through the constrictor.

The relative effects of the different parameters which were changed simultaneously in going to the 142-600 design cannot be isolated at the present time. It will be necessary to run a parametric study of these variables to evaluate their affect on life and other performance parameters.

The use of a regeneratively-cooled jacket to recover most of the energy radiated from the thruster body would increase the efficiency and specific impulse at the mass flows and power levels used in Test No. 29. Very favorable results were obtained when regenerative cooling was applied to a higher power level thruster.

A throat diameter of 0.035 inch was used in the majority of these tests. Larger diameters were not tested, and an increased performance might or might not be obtained through the use of larger throat diameters. At any rate, a further parametric study of performance versus throat diameter should be run to obtain the optimum diameter in thrusters of this power level. The axial gap tests which were made indicated that there is in fact an optimum gap setting for which performance is maximum in a given design. For the design investigated this maximum performance was obtained at a gap setting of approximately 0.026 inch. It would be desirable to re-optimize the gap setting using the new longer nozzle design as described in Section 2 of this report.

~~CONFIDENTIAL~~

4.0 TEST FACILITY AND INSTRUMENTATION

4.1 Thrust Balance

All 2 KW arc-jet thrusters were tested on an uncooled vertical pendulum-type thrust balance in this program. The pendulum was suspended on two flexure joints which were attached to the cover plate of an extension pipe on top of the vacuum test chamber. This thrust balance had been originally designed and developed specifically for transient thrust measurements during the preceding 1 KW program, contract NAS 5-651. The pendulum type thrust balance had an advantage over the horizontal balance for transient measurements in that counterbalancing masses were not necessary, permitting a lower moment of inertia and faster response. Transient testing was not required in the present program, but long duration continuous testing with the existing thrust balance was required, and it was found that a long series of changes had to be made in the thrust balance in order to adapt it for continuous testing.

The uncooled thrust balance was subjected to continuous heating by conduction and radiation during steady state operation, and much effort was necessary to eliminate thermal distortions and thermal drift. A radiation shield was installed around the thruster and attached to the tank. It eliminated most of the reheating by plasma radiation. Several heat barriers installed between the thruster mount and the thrust beam minimized the heat input by conduction.

For the transient tests a null-balance (zero displacement) type of force transducer had been used to achieve fast response. The system was adjusted to give zero output at equilibrium position without thrust. As the thruster moved from the center position a voltage proportional to distance was produced by a linear variable differential transducer, and this served as an error signal for a servo system which energized solenoid coils to return the balance to the zero signal position. Engine thrust was calibrated as a function of the solenoid coil current required to balance thrust.

In continuous testing it was found that the resistance of the solenoid coils was temperature-sensitive, causing severe calibration drift. Since it was not feasible to develop a satisfactory temperature compensation circuit in a short time, the null-balance system was abandoned for continuous testing.

Another approach was taken by converting the balance to an open loop system. The core of the Schaevitz linear variable differential transformer was mounted on the thrust beam, and the coil was mounted on the stationary structure. The displacement of the core relative to the coil produced a voltage which was linear with the core position. This system worked satisfactorily for short runs as far as accuracy of the thrust reading was concerned, but the radial clearance between the core and coil had to be kept small for proper transducer operation, and binding between core and coil would occur during longer

runs because of differential expansion between the pendulum and the stationary structure. This approach was also abandoned after several attempts to eliminate the differential expansions.

In a third attempt, a Bytrex-force transducer was installed to measure small thrust forces. The smallest commercially available transducer which was temperature compensated and insensitive to vacuum had a nominal rating of 0.5 lb force. The resolution was specified by the manufacturer as $\pm 1/2\%$ of full scale, or ± 1.1 grams. The thrust of a 2 KW arc-jet engine at design point is about 10 grams. For testing purposes the thrust measurement error should not exceed 2% of rated thrust, or 0.2 grams. Therefore, it was not feasible to apply the thrust force directly to the transducer. Further study of the problem indicated that acceptable accuracy could be achieved by means of a frictionless mechanical force amplification device which could be designed so that 10 grams of thrust would apply a force of 225 grams on the transducer. In this case the theoretical error of the system was $1/2\%$ of full scale thrust or 0.05 grams. The force amplification device consisted of a thin taut wire stretched horizontally from a fixed point to the transducer. The thrust beam applied a force (thrust minus any restoring gravitational force) perpendicular to the wire in the middle. This caused a displacement of the center, and reaction forces along the wire at the two ends which were essentially equal to the applied thrust force times the mechanical amplification factor, (greater than 10 in this case). A schematic arrangement of the apparatus is shown in Figure 4.1.

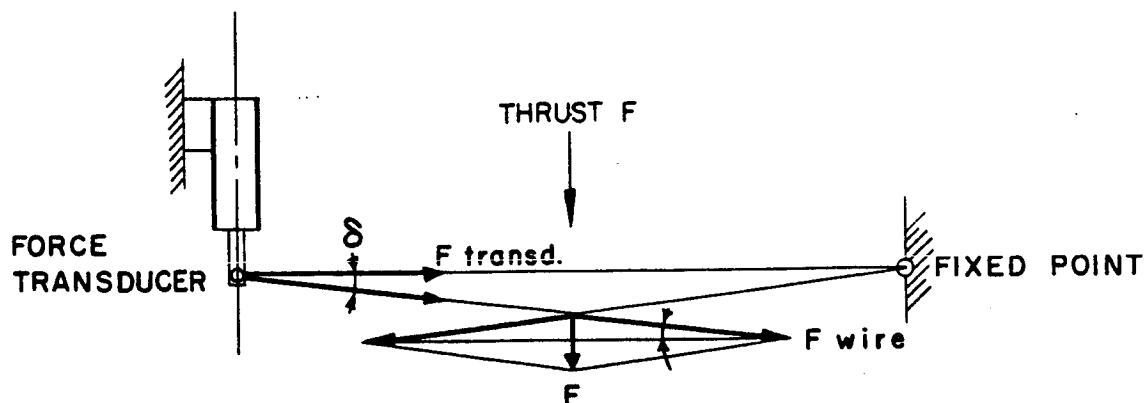


Figure 4.1 Schematic Diagram of Mechanical Force Amplification System for Thrust Measurement

$$\begin{aligned}
 & \left. \begin{aligned} F_{\text{Wire}} &= \frac{F}{2 \sin \delta} \\ F_{\text{Transd.}} &= F_{\text{Wire}} \cos \delta \end{aligned} \right\} F_{\text{Transd.}} = \frac{F}{2} \operatorname{ctg} \delta \\
 & \left. \begin{aligned} F_{\text{Transd.}} &= 225 \text{ gm(max)} \\ F &= 10 \text{ gm(max)} \end{aligned} \right\} \frac{F_{\text{Transd.}}}{F} = \frac{225}{10} = 22.5 \\
 & \delta = \operatorname{arc} \operatorname{ctg} \left(2 \frac{F_{\text{Transd.}}}{F} \right) \approx 1^\circ
 \end{aligned}$$

The wire was sized so that the maximum stress remained within the elastic range, and it caused no noticable hysteresis. The total restoring force acting on the thrust beam consisted of the gravitational force, the spring forces of the flexure joints, and the displacement force of the transducer.

The power and propellant lines caused some minor hysteresis problems. Thermal equilibrium was approached after one hour of operation.

For accurate steady-state thrust measurement it is considered necessary to provide means for calibrating the thrust balance under operating conditions by remote control, since both the vacuum and the heat can distort the tank-beam structure and can affect the transducer. A remotely controlled calibration device was assembled, containing six precision weights of equal mass, suspended on a thin vertical wire which was passed through the center of the weights and over a jewelled-bearing wheel and was attached horizontally to the beam on the thruster axis. A motor-driven rack supporting the weights individually could be lowered and raised in the closed tank by remote control, and each of the six weights could be loaded onto the wire in succession, with the thrust signal being recorded on a Sanborn recorder. The calibration curve was almost linear. Photographs of the thrust calibration device and Sanborn recorder are shown in Figure 4.2 and 4.3. A typical thrust calibration trace is shown in Figure 4.4, and Figure 4.5 shows the corresponding calibration curve.

4.2 Mass Flow Measurement

The mass flow was measured with a sonic orifice flow meter, using an orifice diameter of 0.0039 inch. Upstream pressure and temperature (P_1 and T_1) and downstream pressure (P_2) were measured. The gas was passed through a constant temperature bath ahead of the orifice. The orifice calibration was routinely checked in place by means of a volumetric calibration system built into the test stand. The calibration system contained

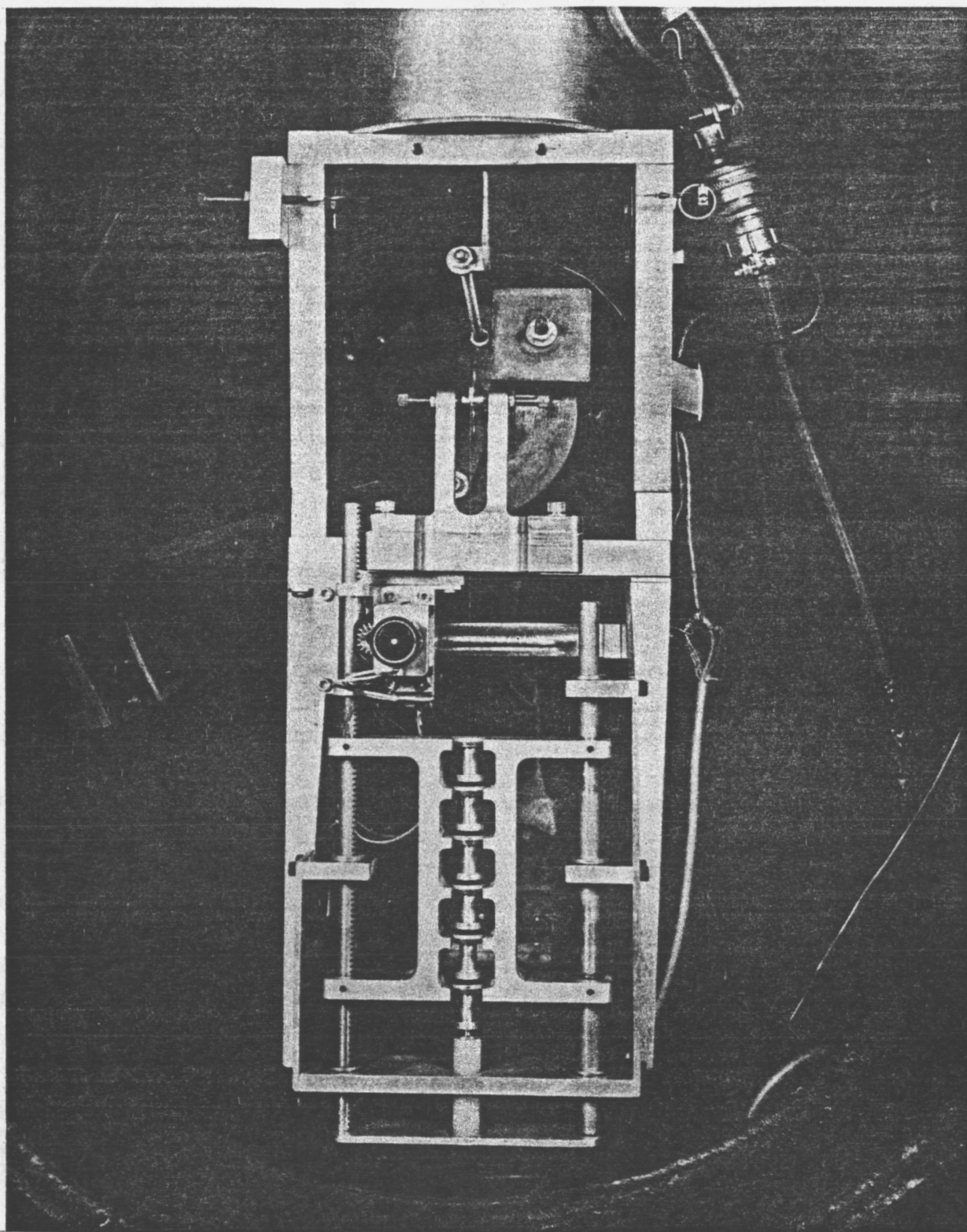


Figure 4.2. Thrust Balance Calibration System -- Remotely Controlled Multi-Weight Mechanism Installed on Thrust Balance in Vacuum Test Chamber

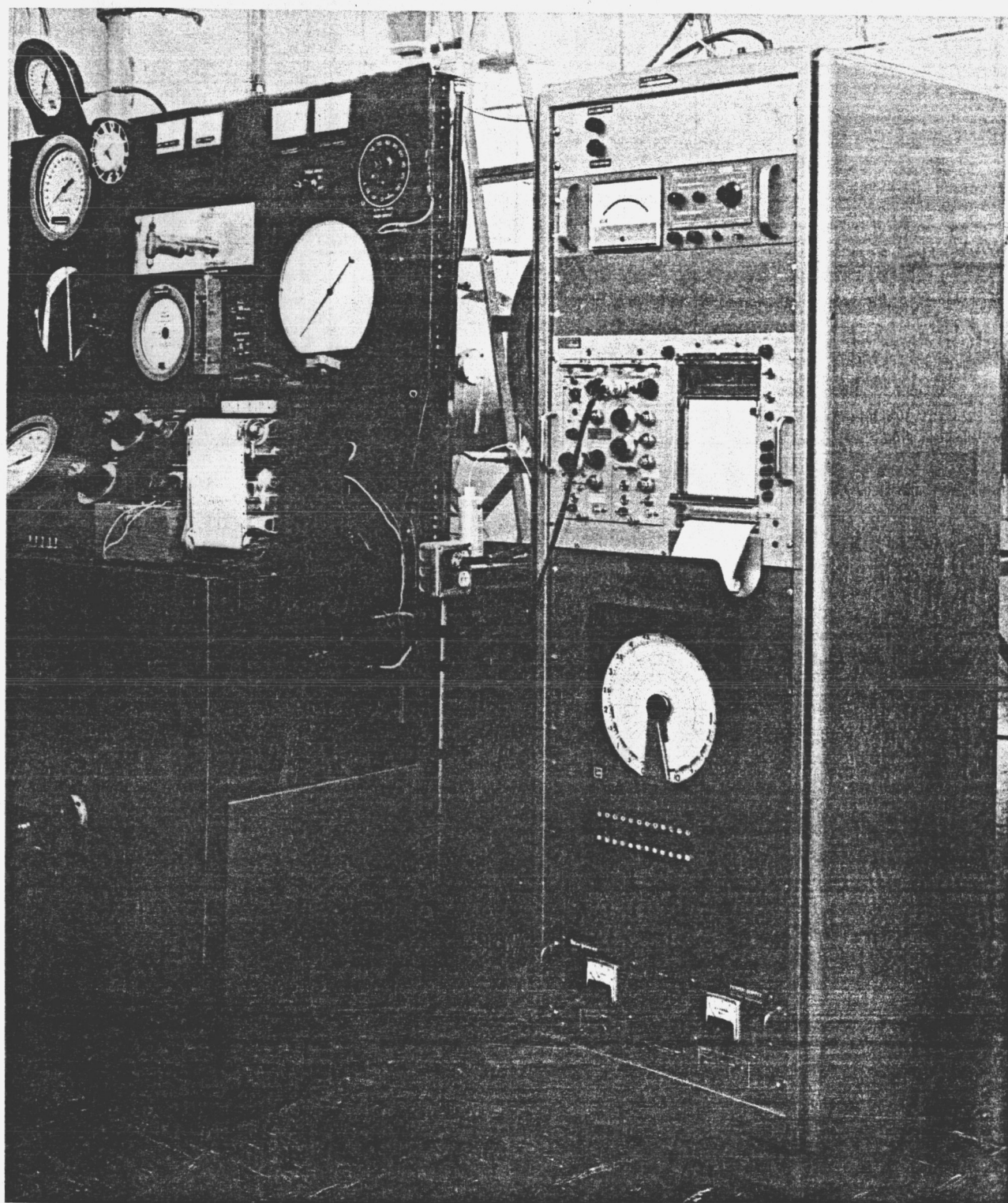
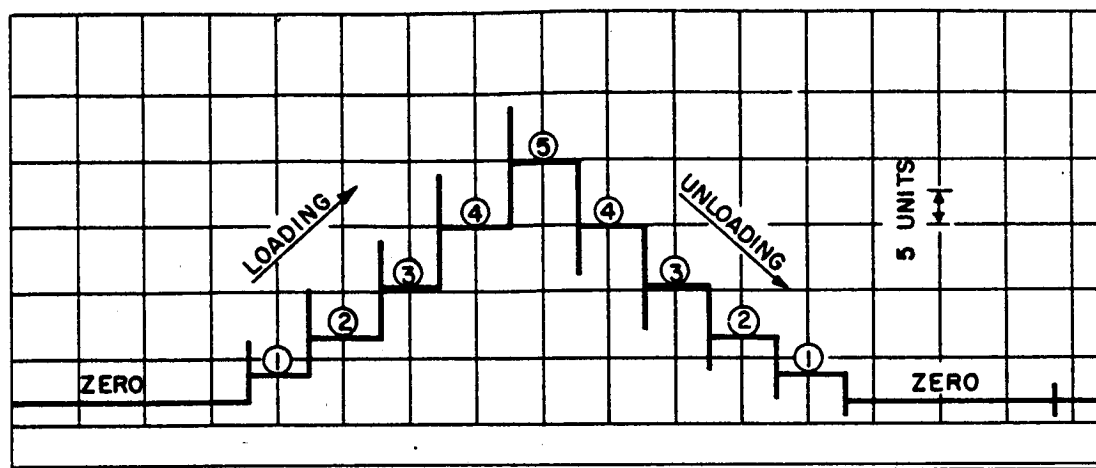


Figure 4.3. Photograph of Thrust Indicating and Recording Instrumentation

TYPICAL WEIGHT CALIBRATION



EVALUATION OF THE CALIBRATION CURVE

Step	Number of Weights	Total Weight (grams)	Read Out (units)	
1	1	3	3.7	Loading
2	2	6	9.5	
3	3	9	17.1	
4	4	12	25.9	
5	5	15	35.5	
4	4	12	28.1	Unloading
3	3	9	17.4	
2	2	6	9.8	
1	1	3	3.8	

(THE CALIBRATION CURVE IS SHOWN IN FIGURE 4.5)

Figure 4.4

Figure 4.4 Typical Recording Trace and Read-out Data for Thrust Balance Calibration Using Remotely-Controlled Calibration System

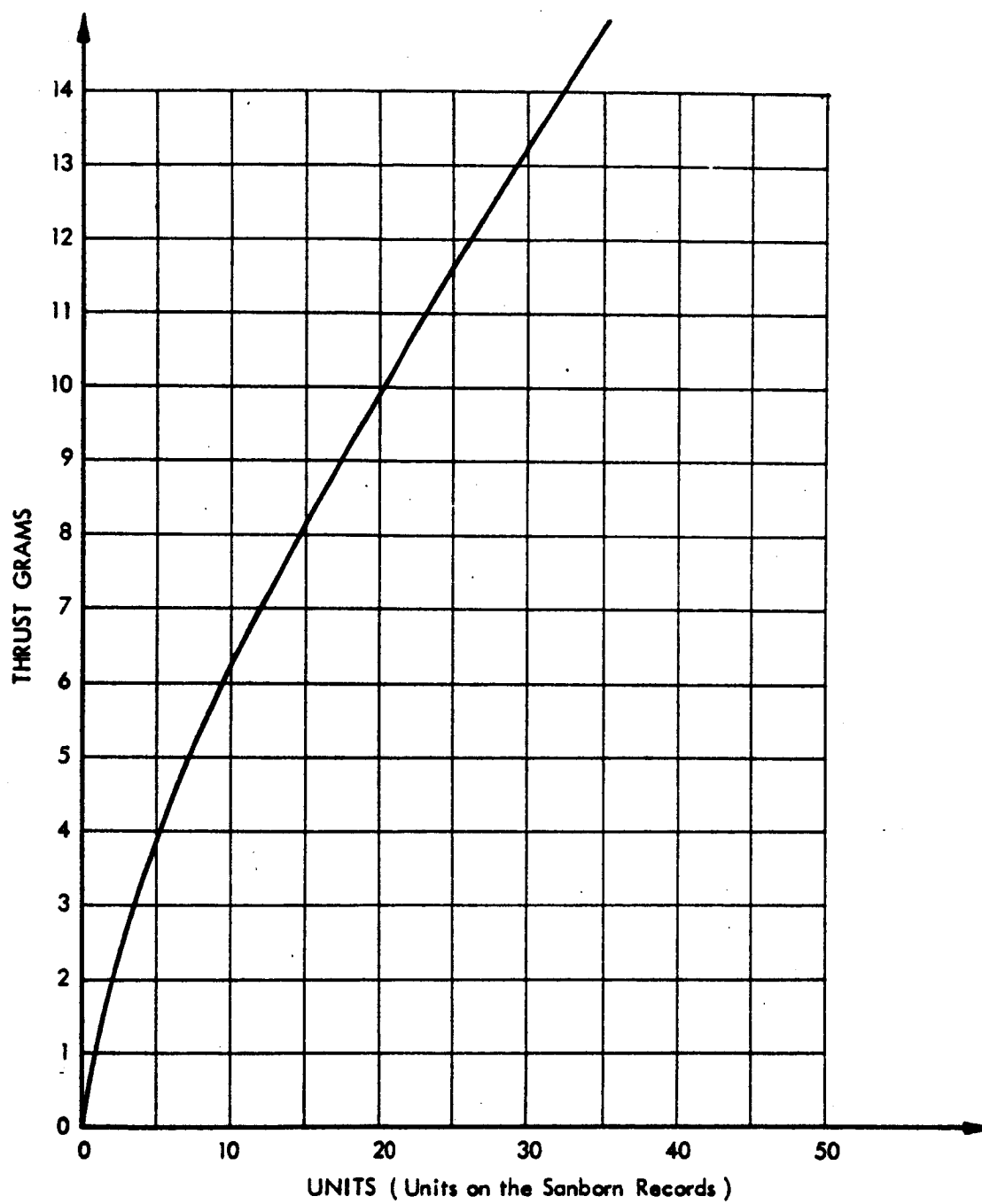


Figure 4.5 Typical Thrust Calibration Curve (see Figure 4.4)

a spherical tank of known volume, and mass flow rate during calibration was determined from measurements of gas temperature and pressure in the container before and after the calibration run, and from run duration. The container was purged several times prior to each test with the propellant in order to avoid contamination of the gas.

The orifice flow meter was also calibrated by an independent testing laboratory, Wyle Laboratories.

For the orifice calibration as well as for the test runs, industrial gaseous hydrogen was used. An analysis of industrial hydrogen is shown in Appendix A. Excessive water content will affect the gas constant and, consequently, the flow measurement by 1%.

Figure 4.6 shows a schematic of the calibration arrangement.

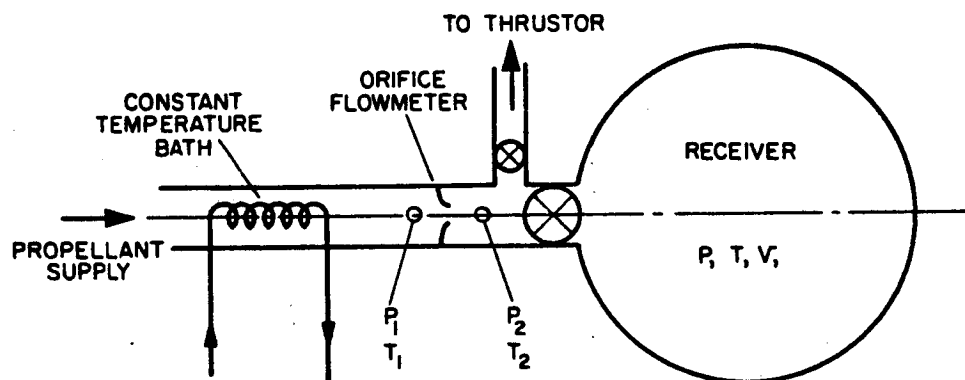


Figure 4.6 Schematic Diagram of Built-in Calibration System for Propellant Flowmeter (dimensions and distances not to scale)

Measured data:

t	=	calibration run time
P'	=	tank pressure before run
T'	=	tank temperature before run
P''	=	tank pressure after run
T''	=	tank temperature after run
V	=	volume of the tank
P_1 & P_2	=	orifice flowmeter upstream and downstream pressures
T_1	=	orifice flowmeter upstream temperature

The total weight of propellant flow W is given by the gas law equation:

$$W = \frac{V}{R} \left[\frac{P''}{T''} - \frac{P'}{T'} \right] \quad \text{where } R = \text{gas constant}$$

and the average flow rate during the calibration run is given by:

$$\dot{W} = \frac{W}{t}$$

The following is a typical set of data for a flow calibration:

P'	=	20 psi abs
P''	=	36 psi abs
T'	=	525°R
T''	=	527°R
P_1	=	505 psig
T_1	=	525°R
t	=	792 seconds
V	=	3.04 ft ³
R	=	766 ft/°R

Figure 4.7 shows the calibration curve for the orifice flowmeter.

4.2.1 Calibration Error Analysis

In the calibration procedure the mass flow rate is a value computed from measured quantities. Associated with each measured quantity is an uncertainty interval arising from various experimental errors, including instrument errors, reading errors, and errors due to unsteady conditions. In general, these errors are independent of each other. The standard procedure for estimating the total uncertainty interval in a measurement is to calculate the square root of the sum of the squares of the individual independent errors. For example:

$$\dot{W} = f(V, R, t, P'', T'', P', T') \quad \text{The error } \Delta \dot{W} \text{ becomes}$$

$$\Delta \dot{W} = \sqrt{\left(\frac{\partial f}{\partial V} \Delta V\right)^2 + \left(\frac{\partial f}{\partial t} \Delta t\right)^2 + \left(\frac{\partial f}{\partial R} \Delta R\right)^2 + \left(\frac{\partial f}{\partial P''} \Delta P''\right)^2 + \left(\frac{\partial f}{\partial T''} \Delta T''\right)^2 + \left(\frac{\partial f}{\partial P'} \Delta P'\right)^2 + \left(\frac{\partial f}{\partial T'} \Delta T'\right)^2}$$

The individual errors in the flow calibration were estimated to be as follows:

ΔV	=	$\pm 0.001 \text{ ft}^3$
Δt	=	$\pm 1 \text{ second}$ (starting and stopping 1/2 second each)
ΔR	=	$\pm 7.6 \text{ ft/}^\circ\text{R}$
$\Delta P''$	=	$\pm 0.25 \text{ psi}$

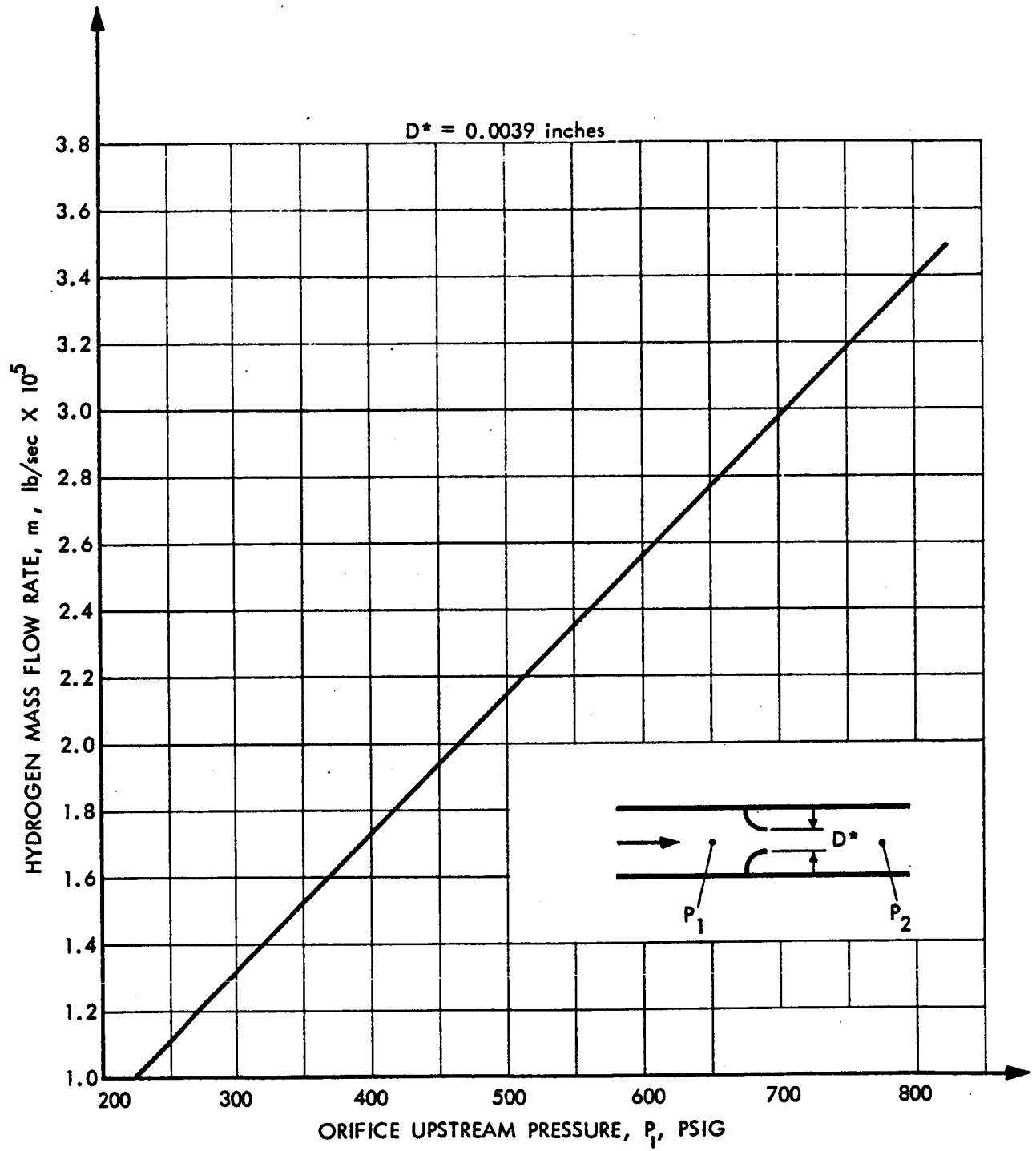


Figure 4.7 Calibration Curve for Orifice Flowmeter

$$\Delta P' = \pm 0.25 \text{ psi}$$

$$\Delta T' = \pm 5^\circ \text{F}$$

$$\Delta T'' = \pm 5^\circ \text{F}$$

Therefore:

$$\frac{\partial f}{\partial V} \Delta V = 0.720 \times 10^{-8} \text{ lbs/sec}$$

$$\frac{\partial f}{\partial t} \Delta t = 2.770 \times 10^{-8} \text{ lb/sec}$$

$$\frac{\partial f}{\partial R} \Delta R = 21.800 \times 10^{-8} \text{ lb/sec}$$

$$\frac{\partial f}{\partial P''} \Delta P'' = 34.200 \times 10^{-8} \text{ lb/sec}$$

$$\frac{\partial f}{\partial T''} \Delta T'' = 46.800 \times 10^{-8} \text{ lb/sec}$$

$$\frac{\partial f}{\partial P'} \Delta P' = 34.200 \times 10^{-8} \text{ lb/sec}$$

$$\frac{\partial f}{\partial T'} \Delta T' = 26.200 \times 10^{-8} \text{ lb/sec}$$

The total mass flow error becomes

$$\Delta \dot{W} = 75.5 \times 10^{-8} \text{ lb/sec}$$

The absolute mass flow is

$$\dot{W} = 21.1 \times 10^{-6} \text{ lb/sec}$$

The relative mass flow error is calculated as

$$\frac{\Delta \dot{W}}{\dot{W}} = \frac{0.755}{21.1} = 0.036$$

or

$$\frac{\Delta \dot{W}}{\dot{W}} = 3.6\%$$

This relative mass flow error of 3.6% can be considered to be the most probable error in the results of the calibration procedure.

This error analysis was checked by a statistical method. The same orifice was calibrated 17 times at different pressures P_1 . The deviation in mass flow may also be expressed by the deviation in flow coefficient. The flow coefficient is defined as

$$\psi = \frac{\dot{W}_{\text{Measured}}}{\dot{W}_{\text{Calculated}}}$$

$$\dot{W}_{\text{calculated}} = A \rho_1 \sqrt{\gamma R T_1} \left(\frac{2}{\gamma + 1} \right)^{\frac{1}{2}} \cdot \frac{\gamma + 1}{\gamma - 1}$$

(A is the flow section of the nozzle)

The standard deviation is defined as

$$\Delta \psi = \sqrt{\frac{\sum_{n=1}^k (\delta \psi_n)^2}{k-1}} \quad \text{where } \delta \psi_n = \psi_n - \bar{\psi} \quad \text{and}$$

$$\bar{\psi} = \frac{1}{k} \left[\sum_{n=1}^k \psi_n \right]$$

The standard deviation applied to the mass flow measurements gives

$$\Delta \psi = 7.5 \times 10^{-3}$$

and the standard relative deviation becomes

$$\frac{\Delta \psi}{\bar{\psi}} = \frac{7.5 \times 10^{-3}}{574 \times 10^{-3}} = 0.013 \text{ or } 1.3\%$$

4.3 Summary of Test Instrumentation and Instrument Calibration

Data on instrumentation used in this program are summarized in Table 13. The calibration curves of the voltmeter and ammeter are shown in Figure 4.8 and 4.9. The test facility components are described in Table 14. Figure 4.10 shows schematically the test arrangement and the location of the instruments.

Figures 4.11 and 4.12 are photographs of the Low Power Electrothermal Engine Test Facility used in this program, showing views of the control consoles, instrumentation, data recorders, and vacuum test chambers.

TABLE 13
DESCRIPTION OF INSTRUMENTATION -- 2 KW ARC-JET ENGINE PROGRAM

Item	Description	Serial No.	Range	Vendor Accuracy	Calibration Date	Remarks
1	Pressure Gauge, Ashcroft 6" Mirror Scale		0 to 1000 psi	0.25% full scale	4-11-63	Orifice upstream
2	Pressure Gauge, Ashcroft 7" Mirror Scale		-30 to 400 psi	0.25% full scale	5-23-63	Orifice downstream
3	Pressure Gauge, Wallace & Tiernan, Model FA 160	DDO3725 NAS 5-651-3	0.1 to 20 mm Hg	0.33% full scale		Tank Pressure
4	Pressure Gauge, Ashcroft	NAS 5-651	0-3000 psi			Pressure in gas bottles
5	Voltmeter, Esterline-Angus Model AW, DC	134850R	0-100V 0-250V 0-500V	1% of full scale	4-10-63	2000 Ω /volt
6	Ammeter, Esterline-Angus Model AW, DC	134850L	0-25A 0-50A	1.5% of full scale	4-10-63	0-50 mv shunt
7	Wattmeter, Esterline-Angus	147207	0-4 KW			
8	Bytrex Load Cell Model BC-05	A-2831	0-0.5 lb	0.5% of full scale		Force transducer

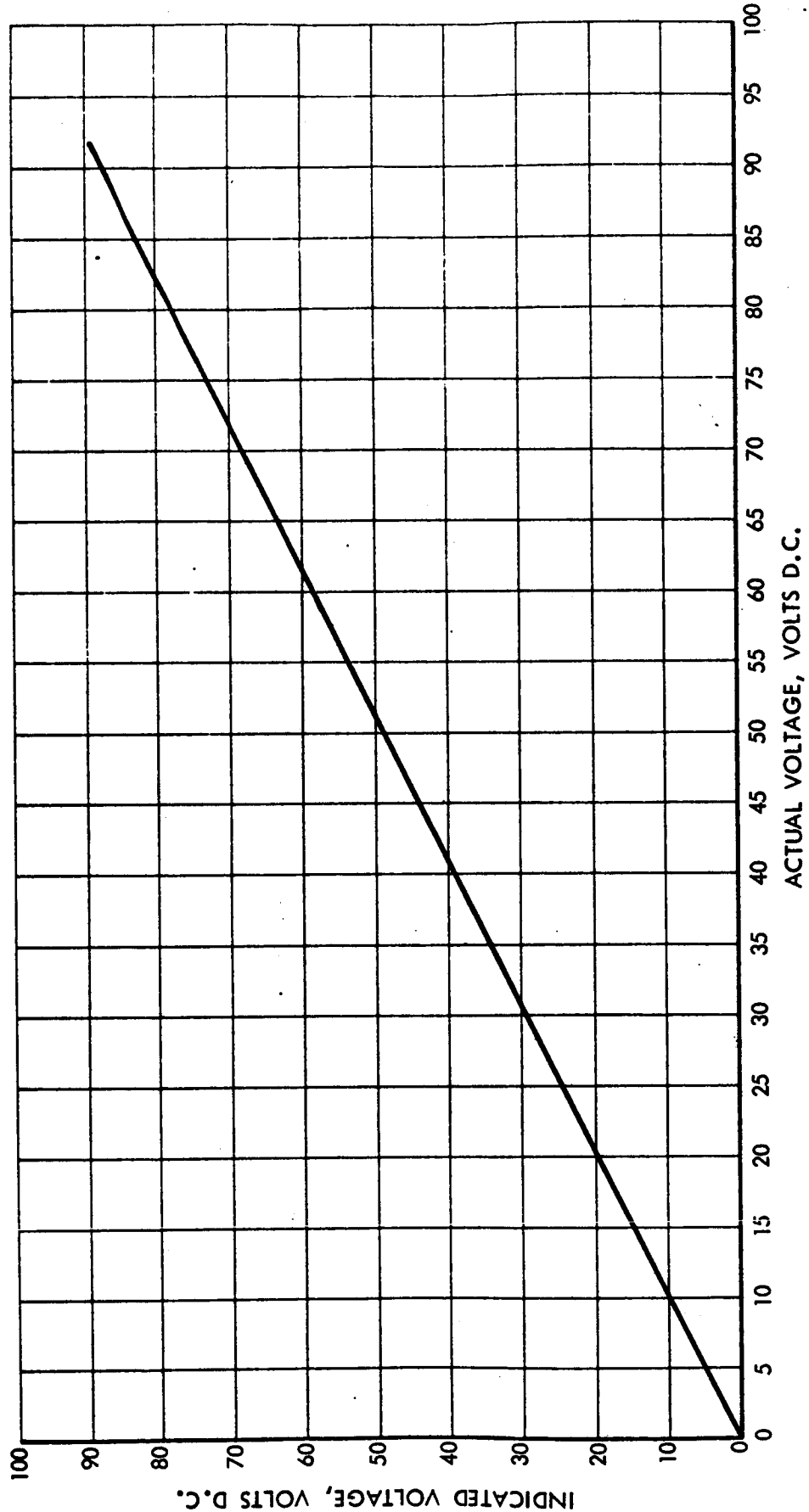


Figure 4.8 Voltage Correction Curve for Esterline-Angus No. 13450R Voltmeter

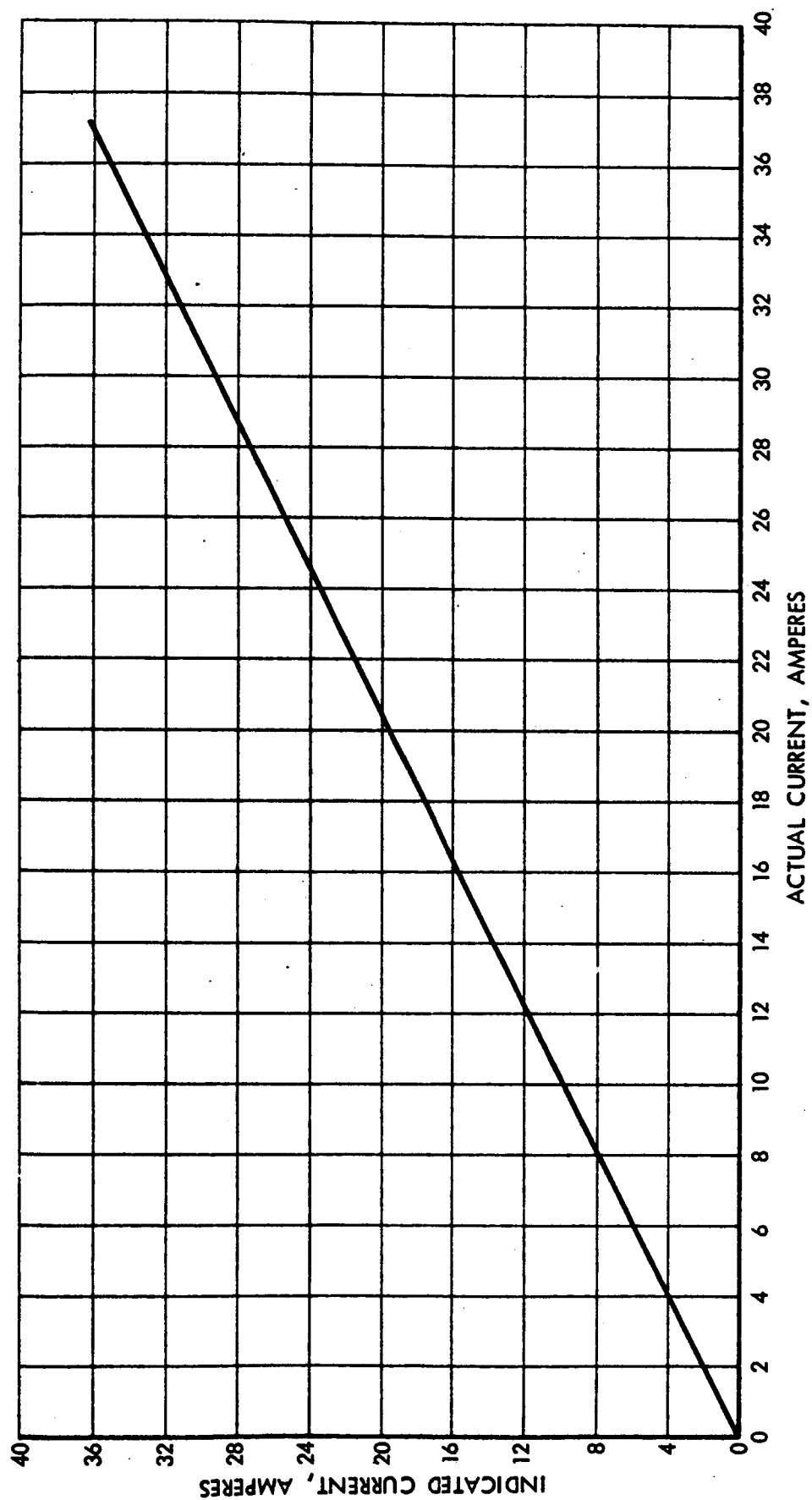


Figure 4.9 Current Correction Curve for Esterline-Angus No. 13450L Ammeter

TABLE 14
DESCRIPTION OF TEST FACILITY -- 2 KW ARC-JET ENGINE PROGRAM

Item	Description	Remarks
1	Vacuum Tank, 30" dia. x 84", water cooled Contains: Thrust beam Automatic thrust calibration device Calorimeter	
2	Stokes Vacuum Pump, Type RGS-SP-AVM, Serial No. 62136-86, Size 615, NAS 5-651-74	Both pumps in series create a vacuum of 0.4 mm Hg at 3×10^{-5} lb/sec H_2 mass flow
3	Stokes Microvac Pump, Model 412 H-10 Serial No. 83100, Lot No. C-86714-40, NAS 5-651-74, 490 RPM, 10 HP, 300 cfm	
4	Miller Rectifier NAS 5-651-25, 12 KW	
5	Sanborn, Model 297, Recording Unit	Thrust Recorder
6	Gas supply, industrial gaseous hydrogen in bottles	

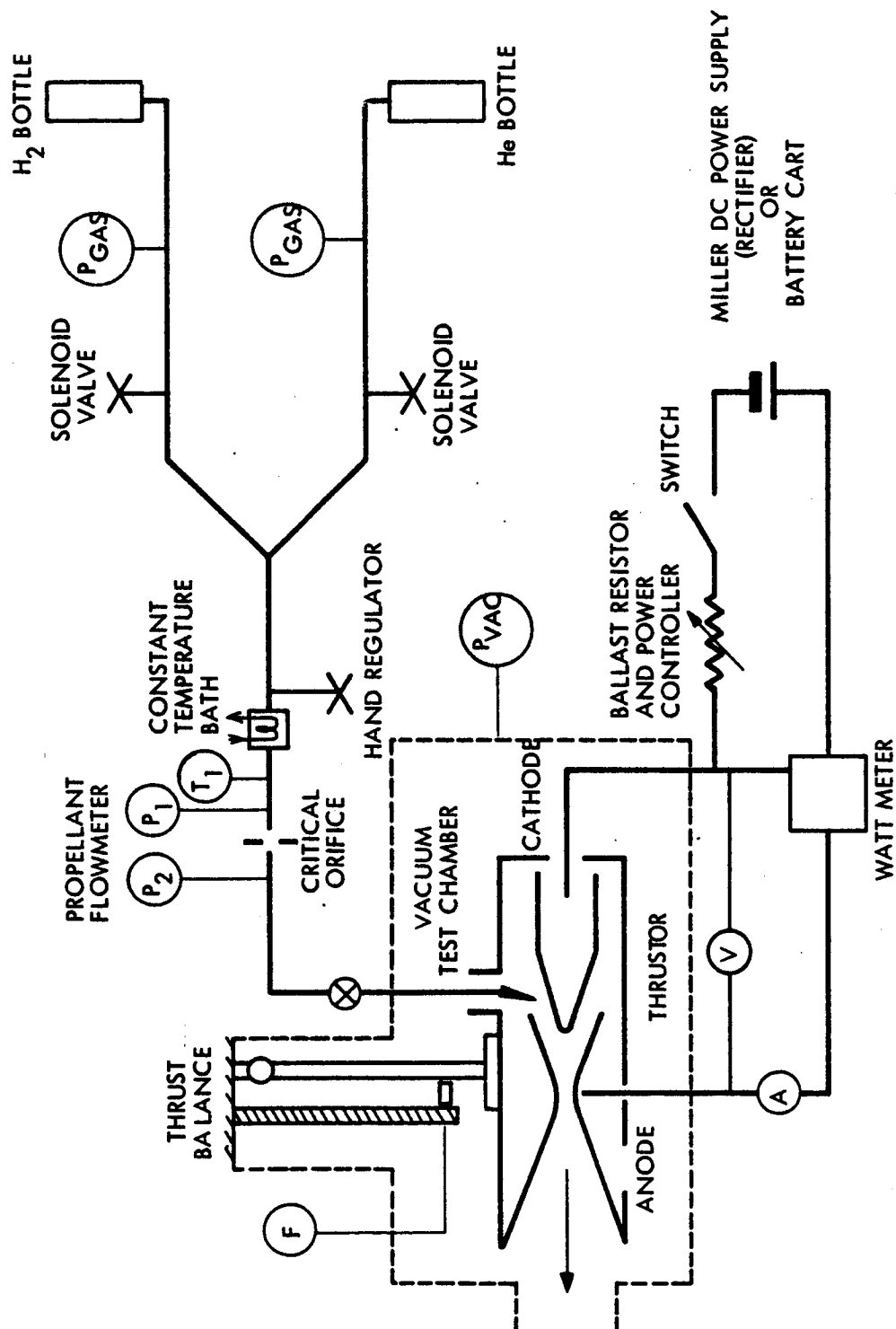


Figure 4.10 Schematic Diagram of 2 KW Arc-Jet Test Facility and Instrumentation Connections

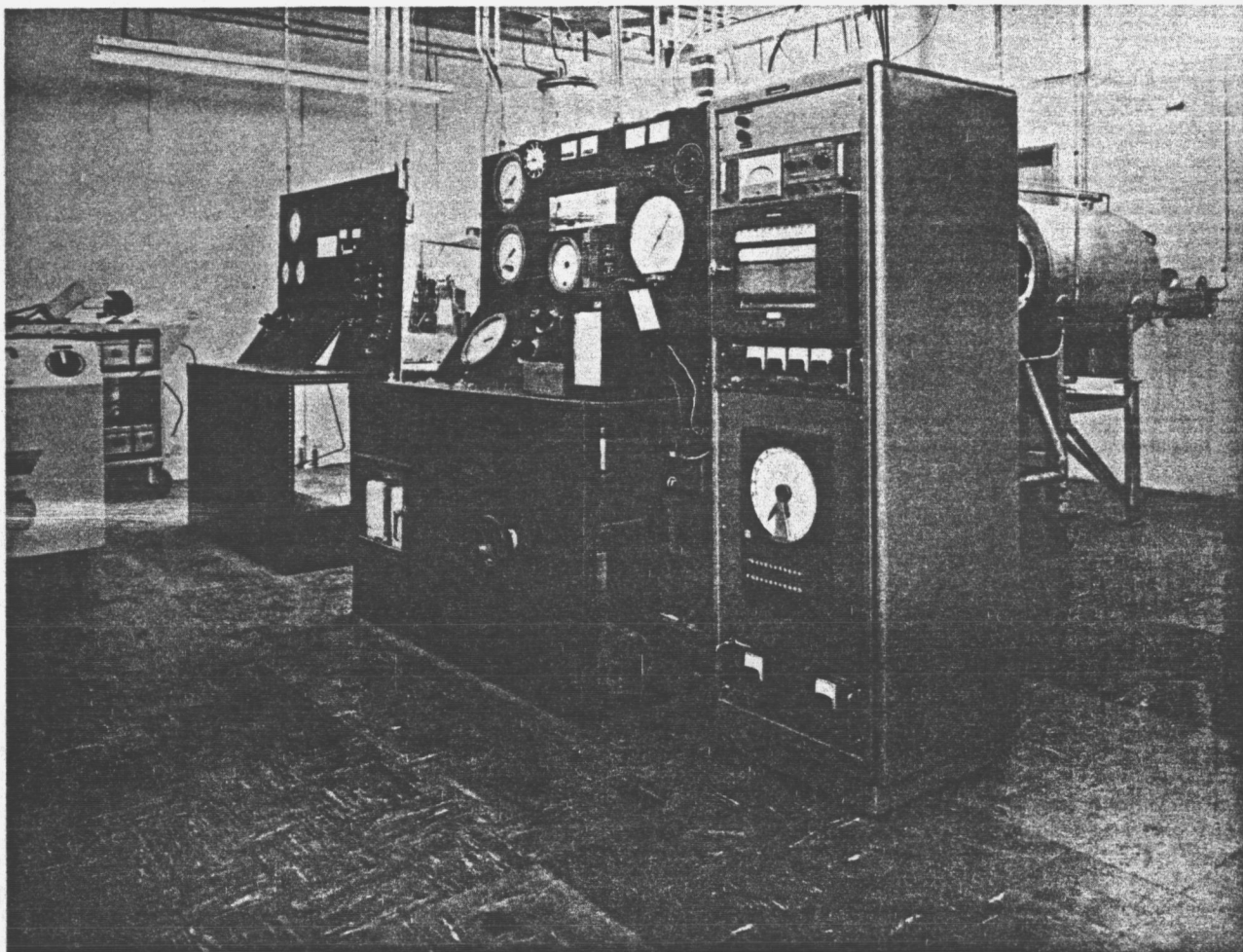


Figure 4.11. View of Control Consoles -- Low Power Electrothermal Engine Test Facility

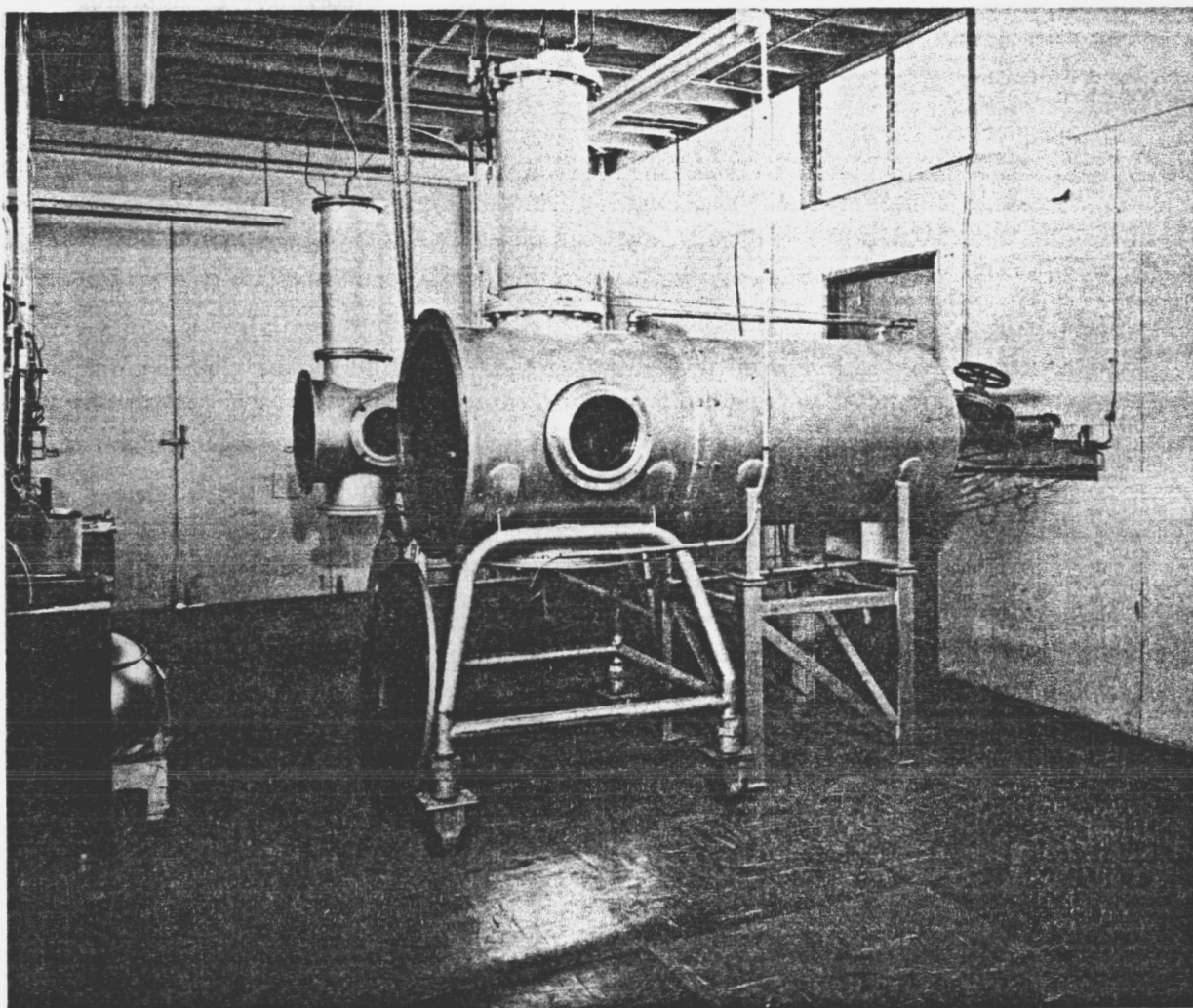


Figure 4.12. View of Vacuum Test Chambers -- Low Power
Electrothermal Engine Test Facility

5.0 THRUSTOR ASSEMBLY, INSPECTION, TESTS, AND DISASSEMBLY PROCEDURES

This section of the report covers the procedures used in assembling the thrustor units and the quality control which is maintained in the manufacture of these parts. In addition, the procedures used before and after the tests to check the calibration of instruments and the performance of the thrustor are also outlined.

5.1 Thrustor Assembly and Inspection

Each component part of the thrusters was carefully checked to insure that the dimensions were within the design tolerances as shown on the drawings in Section 2 of this report. Figure 5.1 shows the assembler dimensionally checking the boron nitride rear insulator part. Precision measuring instruments were used and all parts were handled with proper precautions for cleanliness, as exemplified by the gloves being worn by the assembler in Figure 5.1. A special assembly room was set up for the express purpose of assembling these thrusters, and all efforts were made to insure cleanliness in the room and also to provide the assembler with necessary instruments.

After all thruster parts had been checked and passed in the quality control inspection procedure, the thruster was assembled and the cathode-anode axial gap spacing was set. Figure 5.2 shows the apparatus used in setting the gap spacing. The cathode was run in until it touched the anode and the length was measured. The cathode was then backed out the required distance to set the axial gap. In several cases this gap was checked after the thruster had been run to insure that no change in gap spacing had occurred in handling. The cathode was also weighed prior to thruster assembly for a test run, and this weight was recorded.

The thruster was leak-checked in the cold condition by placing a cap over the nozzle, filling with helium at a pressure of 200 psig, closing the gas supply valve, and allowing the thruster to remain undisturbed for one hour. The decrease in pressure after one hour was noted. If undue pressure loss occurred, the thruster was disassembled and the leak corrected. In addition, cold flow tests were made in which helium was supplied to the thruster through a critical orifice at upstream orifice pressures P_1 of 200, 300, and 400 psig, and the orifice downstream pressure P_2 (used as a measure of the chamber pressure) was recorded. The resistance from the cathode to the anode was also checked using an ohmmeter. A high voltage hypot device was employed to determine the voltage at which the gap between cathode and anode broke down in air. The use of this device is illustrated in Figure 5.3. This latter test proved inconsequential since the voltage at which the different thrusters broke down was too close to be measured accurately with the hypot. All of these preliminary tests were performed prior to a hot firing test in the vacuum test chamber.

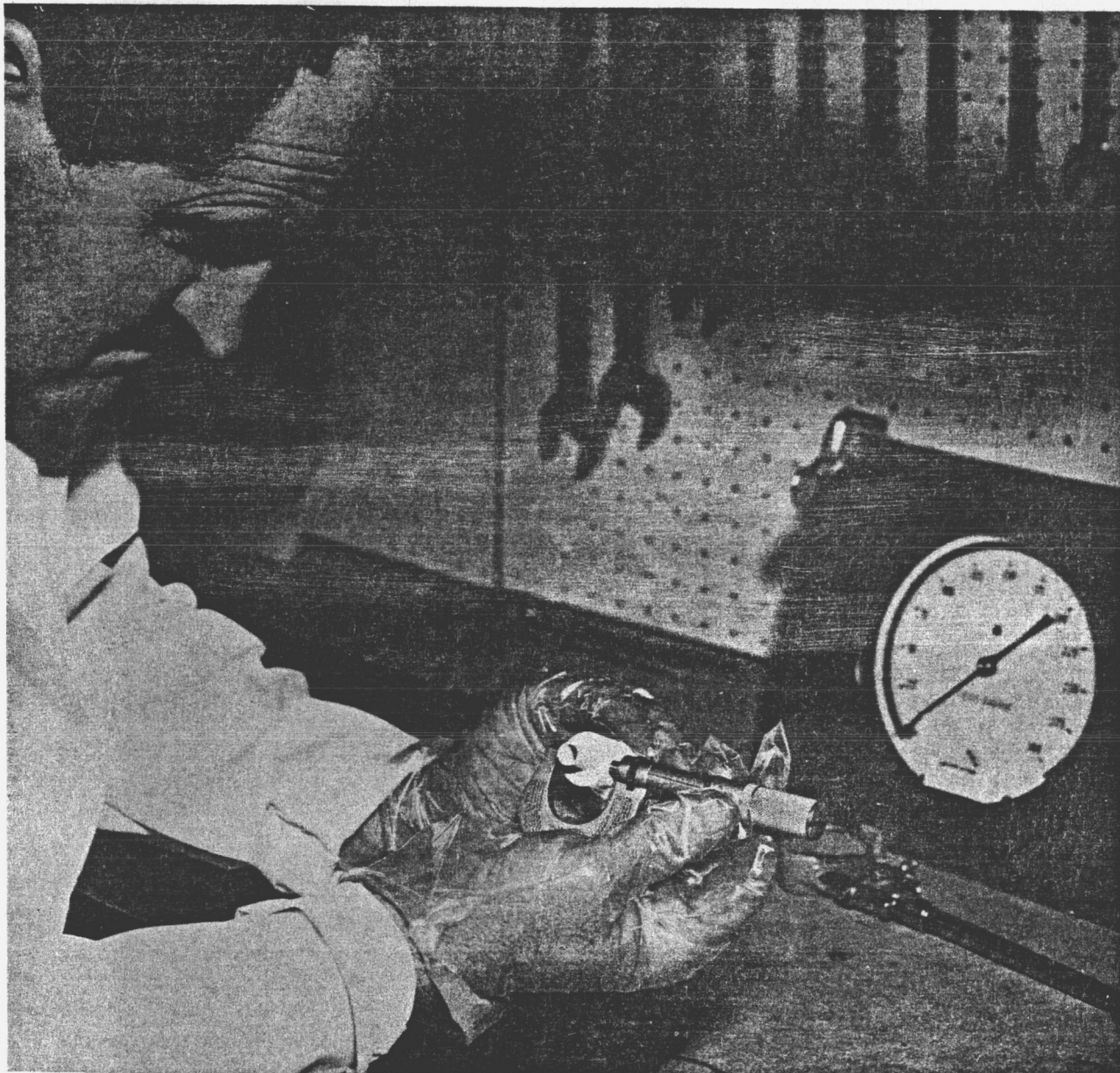


**Figure 5.1. Assembler Shown Inspecting Boron Nitride Rear Insulator
for Dimensional Accuracy**

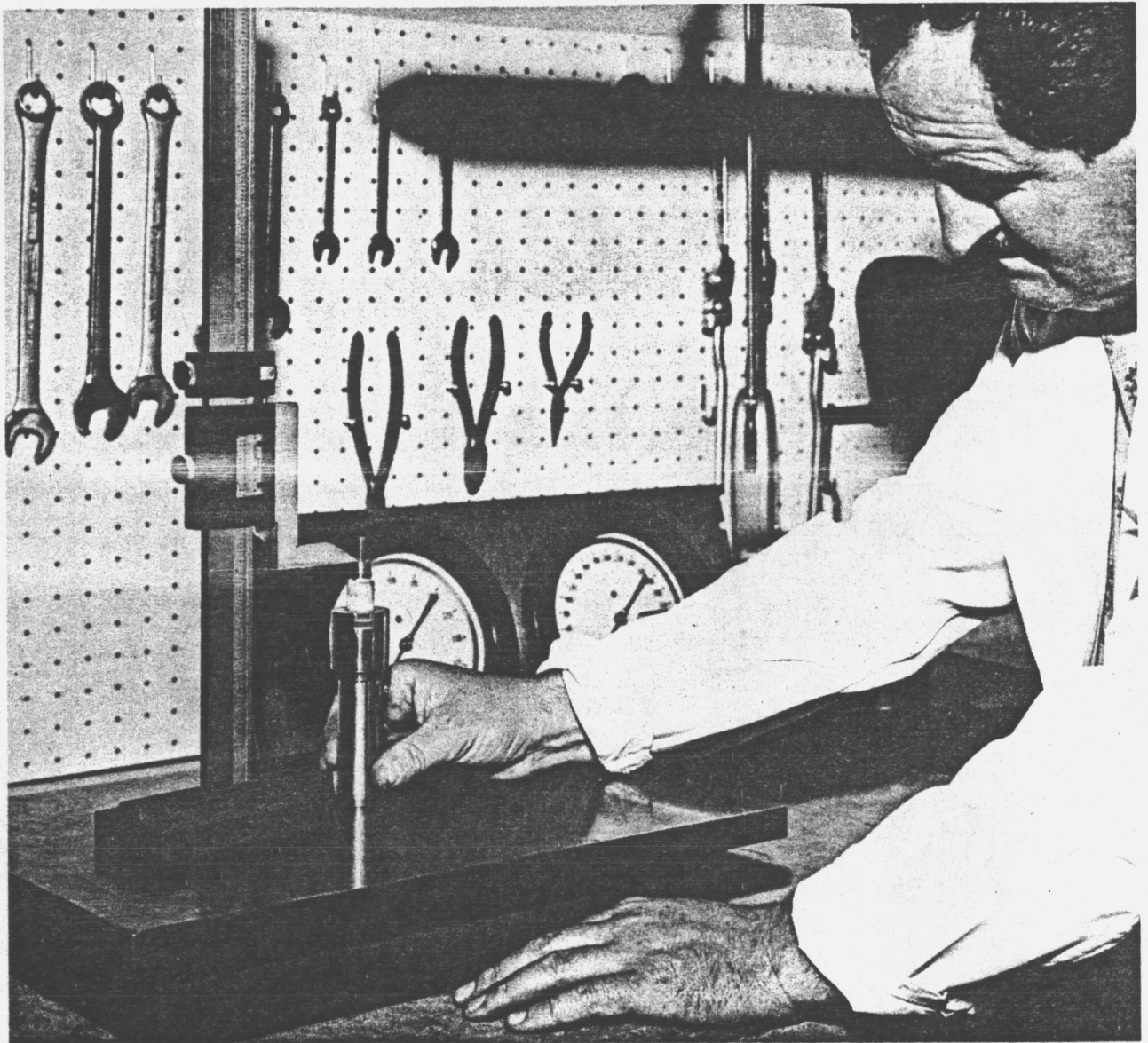


Figure 5.2. Assembler Shown Using Precision Gauge to Set Cathode-Anode Gap Spacing

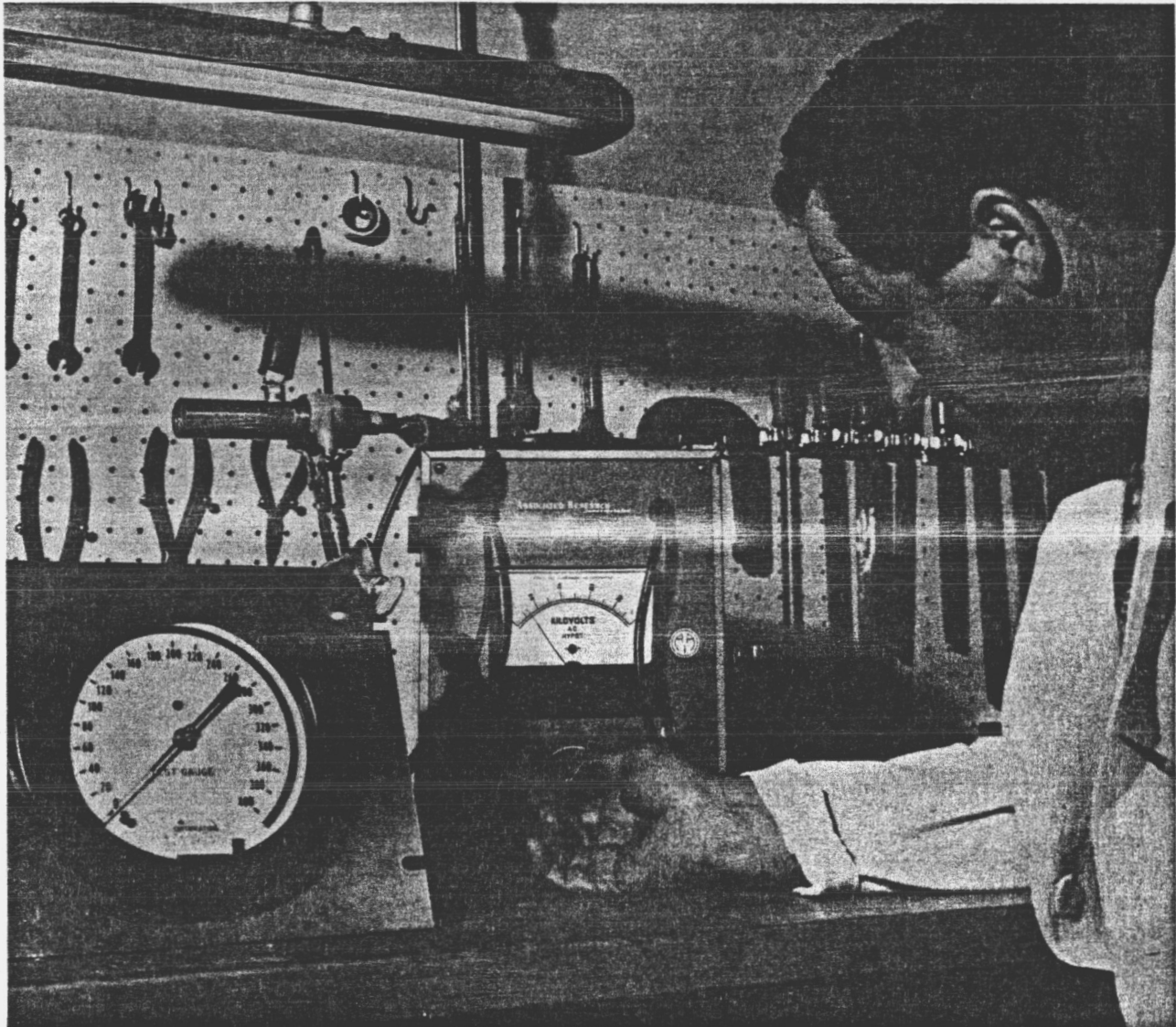


Figure 5.3. Assembler Shown Using High Voltage Hypot Instrument to Check Break-Down Voltage of Cathode-Anode Gap in Thrustor

5.2 Testing Procedure

After the thruster had been assembled, it was installed in the test chamber. The thrust measurement device was then connected and a calibration of the thrust balance was performed using the remote calibration system described in Section 4, and shown in Figure 4.2. The test chamber was then pumped down an additional calibration of the thrust balance was made. Cold flow checks were then made on the thruster by setting a mass flow, measuring the downstream pressure of the orifice (p_2) and the thrust reading. From these readings the cold flow specific impulse was calculated. The test was then begun by setting the propellant flow rate applying the open circuit voltage. After the start was obtained the power was set at the desired value and the remaining parameters were measured and checked.

After the test had been completed additional thrust balance calibrations were performed to determine whether any drift in the thrust calibration and read-out had occurred. The thruster was allowed to cool for a sufficient length of time before the test chamber was opened. After the thruster had cooled the cold flow checks on inlet pressure and thrust were repeated. These gave some indication of the conditions inside the thruster and gave a comparison of results with those obtained prior to the run.

5.3 Thruster Disassembly and Re-inspection

After the hot test was completed, the thruster was disassembled by the same person who had assembled it. On disassembly several general observations were made and recorded, including the condition of the various component parts. A leak-check was again performed to determine if any leaks had developed during the test. After all the parts had been disassembled, the cathode was weighed and the cathode tip was checked by using a 50 power comparator. Visual observations on the condition of the anode, and the erosion pattern, if any, were also made on disassembly. Where possible, the average throat diameter after the test was measured.

6.0 CONCLUSIONS AND RECOMMENDATIONS

6.1 Conclusions

1. A 2 KW D.C. arc-jet thruster has been successfully developed and endurance tested for 150 hours in continuous operation using hydrogen as a propellant. During the test the average specific impulse level was 935 seconds, the average efficiency was 30.7%, and the average thrust level was 30.1 millipounds. The test was terminated voluntarily without failure, and post-test examination of the disassembled thruster indicated that the thruster undoubtedly could have completed a longer duration test.
2. A duplicate thruster has been tested for short periods of time at specific impulse levels up to 1275 seconds, and at power levels from 1.5 to 3.5 KW.
3. The final thruster developed and endurance-tested under this program (series 142-600) incorporated a number of major simultaneous changes in design from the previous designs, based on the results of the analytical and experimental work. There was no time remaining in the program for a detailed investigation and optimization of the final design, and the test results are not necessarily representative of the best that can be achieved with this design.
4. The noteworthy success of the final design compared to all previous design approaches led to the following tentative conclusions regarding low power arc-jet configurations:
 - a. Arc chamber pressures: The previous belief that a relatively high arc chamber pressure (over 5 atmospheres), with a correspondingly small constrictor-throat diameter, was advantageous for performance and life has been fairly well disproved. Since it was not possible to vary chamber pressure without varying other important parameters simultaneously, the exact effects of, and optimum value of, chamber pressure alone remain uncertain, but the final design successfully employed a chamber pressure of about 1.2 and 1.5 atmospheres with no apparent performance penalty, and even lower values might be advantageous.
 - b. Constrictor-throat diameter: This is related to chamber pressure, and again no true optimum could be determined for

~~CONFIDENTIAL~~

this parameter alone. The largest throat size tested - 0.035 inch diameter - produced performance and life at least equal to, or better than, any of the smaller sizes tested, and was less sensitive to the effects of any erosion. It is possible that a still larger diameter would be even more advantageous.

- c. Constrictor length and length/diameter ratio: The earlier tests under this program were run at length/diameter ratios between 1.5 and 1.8, but the tests indicated that the anode foot point of the arc had a tendency to periodically move from the nozzle back up into the throat, resulting in severe erosion. In the final design an L/D value of 1.0 (length = 0.035 inch) was selected somewhat arbitrarily in an attempt to avoid that problem, and it was found that erosion was greatly reduced without noticeable effect on performance. Again, this value is not necessarily the optimum, and a still smaller value may be better. This change was made simultaneously with the change in injector design, and it is difficult to isolate the individual effects.
- d. Cathode - anode axial gap setting: A series of tests to optimize gap setting was run on the early design and it was found that a gap setting of 0.026 inch produced the best results, apparently because it caused most of the arc column to be stretched through the constrictor with the foot point located just downstream of the throat in the divergent section of the nozzle. Apparently, larger gap settings tended to cause the foot point to locate in the constrictor or inlet with high erosion and heat losses, while smaller settings caused the arc to stretch out too far into the nozzle, with reduced performance. (Note that a rather short nozzle was used in these tests). The 0.026 inch axial gap corresponded to a flow area ratio of 1.0 between the minimum annulus area and the throat area for a 0.035 inch diameter constrictor. The same gap setting was arbitrarily used with satisfactory results in the final design, even though the constrictor length was reduced and the nozzle length was increased. It may not be optimum for this design.
- e. Propellant injectors and vortex chamber: It was found that particular attention must be paid to the design of the injectors and vortex chamber in the very small size thrustors because of

~~CONFIDENTIAL~~

the importance to thruster life of generating a controlled vortex and maintaining it through the constrictor, coupled with the difficulty of doing so under the very low Reynolds number conditions prevailing. In the earlier designs threaded spiral passages were employed to introduce the gas into the vortex chamber and produce a swirl, but test results and further analysis indicated that this approach did not provide adequate control over the gas flow patterns in the vortex chamber. In the final design six precision injector orifices were employed to inject the gas tangentially into a redesigned vortex chamber. change is believed to have contributed greatly to radical improvement in life and performance.

- f. Anode-nozzle cooling: In the parametric experimental investigation of geometry during the earlier part of this program an anode-nozzle insert design was used which had been developed in basic form in the 1 KW program during the previous year. This insert was cooled by a combination of some regenerative cooling at the upstream face, radiation cooling at the downstream face, and cooling at the outer surface by heat conduction across the contact surface to the molybdenum housing. A brief test in the previous program had indicated that an extended radiating surface provided no noticeable improvement, and internal heat transfer was felt to be satisfactory. In the present parametric investigation the same basic insert design was used, but with a greatly enlarged constrictor and no upstream regenerative cooling. Hand calculation of internal heat transfer patterns and temperature distributions was attempted but was found not to be feasible because of the complex boundary conditions and irregular three-dimensional nature of the problem. However, as the parametric investigation progressed evidence accumulated that both internal and external heat transfer paths for the insert were inadequate, resulting in "heat dams" and excessive internal temperatures. In the final insert design larger internal heat flow paths and a substantially larger external radiating surface were provided, and the results were very satisfactory. Again, the design has not yet been optimized.
- g. Nozzle divergence angle and area ratio: In the previous 1 KW program it had been concluded from an analysis that the best

~~CONFIDENTIAL~~

nozzle design for very low power arc-jets, which operate at very low Reynolds numbers, is one with a relatively large divergence angle and a relatively short length, in order to minimize wall friction effects. However, a simplified re-analysis during the present program indicated that the optimum divergence half angle is about 20° and the optimum area ratio for an ambient pressure of 0.1 mm Hg abs. is about 50/1, resulting in a much longer and narrower nozzle than previously used. During the course of this experimental program two different nozzle divergence half-angles -- 20° and 30° -- and a wide range of area ratios were tested, but in all cases except one other geometric parameters were varied simultaneously. The best interpretation of these results is that the final 20° half-angle, 50/1 area ratio nozzle was distinctly superior in performance to all of the nozzles of smaller area ratio and/or larger divergence angle which were tested, tending to confirm the validity of the latest analysis. It was also found that better results are obtained if all sharp-edged corners in the arc chamber and nozzle flow passages are carefully rounded.

- h. Electrode erosion: It was found that cathode erosion and anode erosion are both very sensitive to the operating mode and configuration of the arc, which in turn depend on certain critical details of cathode, anode and flow passage geometry, flow patterns, and heat transfer paths. If the design is such that the arc can be stabilized in the desired position, with the electrodes suitably cooled (but not over-cooled) in the arc attachment regions, then erosion can apparently be held to an acceptably low value over a long period of time, as demonstrated by the thruster which completed the 150 hour test. If the design is grossly incorrect in any of the important details, it is likely that the arc will cause severe erosion of one or both of the electrodes, leading to rapid failure of the thruster. In this respect, low power arc-jet thrusters appear to be much more sensitive to lack of design optimization than do higher powered arc-jet thrusters which seem to operate reasonably well over a rather broad range of configurations.

5. It is concluded that the major objective of the present program -- the demonstration of the feasibility of achieving continuous long life

~~CONFIDENTIAL~~

operation with low power arc-jets -- has been essentially fulfilled, and the way is now open to proceed immediately with the development of thrusters with still better life and performance capability.

6. The design of the present continuous-running low power arc-jet thruster is not basically suitable for use in applications requiring short-pulse operation, as in some attitude control applications. However, the knowledge and experience gained in developing this thruster should permit the design and development of a similar thruster for pulse-mode operation with a minimum of difficulty.

6.2

Recommendations

1. Research and development of the present 2 KW continuous-running arc-jet thruster should be continued. The design approach which proved successful in this program should be further optimized and extended. Full regenerative cooling should be employed to increase both performance and life. Full regenerative cooling would be expected to provide better life both directly through better anode cooling and indirectly through increases in efficiency which permit higher flow rates and larger dimensions for fixed levels of power input and specific impulse. The parametric investigations of geometry should be continued for the new design. The best design should be selected and endurance tested for 500 - 1000 hours. Efficiency levels in the 35-40% range could be expected from a thruster operating at a specific impulse of about 1000 seconds.
2. The regeneratively-cooled thruster should also be tested at specific impulse levels above 1000 seconds (to perhaps 1500 seconds) to determine its potential for operating satisfactorily in that regime.
3. If the use of arc-jet thrusters in attitude control system is contemplated, a separate program should be initiated for the development of thrusters designed specifically for pulse-mode operation.

7.0 REFERENCES

1. Greco, Robert V., and Stoner, Willis A., "Development of a Plasmajet Rocket Engine for Attitude Control." (U), Plasmadyne Summary Report No. FR-111-651, Vol. 1, for Phase I of Contract NAS 5-651, December 1961. [REDACTED].
2. McCaughey, Owen J., Stoner, Willis A., Humpal, Harold H., and DeViney, William D., "Development of a Plasmajet Rocket Engine for Attitude and Orbit Control, " (U), Plasmadyne Final Summary Report No. FR-112-651, Contract NAS 5-651, (Confidential).
3. Marchand, Frederic E., et.al., "Application Studies of Low Power Arc-Jet Engines for Attitude Control, Station-Keeping, Orbit Transfer and Related Uses, " (U), Plasmadyne Final Summary Report No. FR-112-2544, Contract NAS 8-2544, (in publication) (Unclassified).
4. Marchand, F. E., Arthur, P. D., and McCaughey, O., "Results of Satellite Raising and Orbit Transfer Studies for Low Power Electrothermal Arc-Jet Propulsion Systems, "AIAA Electric Propulsion Conference, AIAA Preprint No. 63010, March 1963.
5. Marchand, F. E., and McCaughey O. J., "Applicability of Electrothermal Arc-Jet Engines for Attitude Control and Station-Keeping of a 550 Pound Synchronous Equatorial Satellite, " (U), Plasmadyne Engineering Report No. PRE-109, Revision A, 6 February 1963.
6. Beech Engineering Report No. 13558, "Electrothermal Engine Propellant Storage and Feed System Study Phase II Report, " September 1962.

APPENDIX A*

GAS CONSTANT OF INDUSTRIAL HYDROGEN

The water content of commercial hydrogen was measured with a CEC moisture monitor type 26-304 ME and was found to be as high as a thousand volume parts of water vapor in a million parts of the sample. There are

10^6 molecules of mixture

10^3 molecules of H_2O

thus, the number of H_2 molecules is 999×10^3 and the molecule ratio ϵ becomes

$$\epsilon = \frac{m_{H_2} + m_{H_2O}}{m_{H_2O}} = \frac{999 \times 10^3 \left[\frac{2}{6.03 \times 10^{26}} \right] + 10^3 \left[\frac{18}{6.03 \times 10^{26}} \right]}{10^3 \left[\frac{18}{6.03 \times 10^{26}} \right]} = 112$$

1 kmol H_2 = 2 kg

1 kmol H_2O = 19 kg

1 kmol contains 6.03×10^{26} molecules

$m_{H_2} + m_{H_2O} = W$ (W denotes a quantity, e.g. 1000gm)

$$m_{H_2O} = \frac{W}{\epsilon}$$

$$m_{H_2} = W \left(1 - \frac{1}{\epsilon} \right)$$

$$m_{H_2O} = \frac{1000}{112} = 9 \text{ gm Water}$$

1000 gas mixture

$$m_{H_2} = 1000 \left(1 - \frac{1}{112} \right) = 991 \text{ gm Hydrogen}$$

gas constant of Hydrogen = 766 ft/ $^{\circ}$ R

gas constant of Water vapor = 86 ft/ $^{\circ}$ R

$$R_{res} = \frac{\sum m_i R_i}{\sum m_i} = \underline{\underline{759.88 \text{ ft}/^{\circ}\text{R}}}$$

$$\frac{R_{H_2}}{R_{mixture}} = \frac{766}{759.88} = 1.008 \text{ (deviation is appr. 1\%).}$$

(NOT USED)